Particles settling dynamics

David de Souza

INSTITUT POLYTECHNIQUE DE PARIS

NNT : 2021IPPAE003

Thèse de doctorat

ENSTA

IP PARIS

Dynamique de sédimentation de particules

Thèse de doctorat de l'Institut Polytechnique de Paris
préparée à École nationale supérieure de techniques avancées

École doctorale n°626 École doctorale de l'Institut Polytechnique de Paris (EDIPP)
Spécialité de doctorat : Ingénierie Mécanique et Energétique

Thèse présentée et soutenue à Palaiseau, le 19 mars 2021, par

DAVID DE SOUZA

Composition du Jury :

Véronique Roig Professeure, Institut de Mécanique des Fluides de Toulouse	Présidente
Sebastien Aumaître Ingénieur de recherche, Commissariat à l'Énergie Atomique CEA–Saclay (Service de Physique de l'État Condensé)	Rapporteur
Romain Volk Maître de conférences, École Nationale Supérieure de Lyon (Laboratoire de Physique)	Rapporteur
Martin Obligado Maître de conférences, Université Grenoble Alpes (Laboratoire des Écoulements Géophysiques et Industriels)	Examinateur
Aymeric Vié Maître de conférences, École CentraleSupélec (Laboratoire Énergétique Moléculaire et Macroscopique, Combustion)	Examinateur
Romain Monchaux Professeur, École Nationale Supérieure de Techniques Avancées Paris (Unité de Mécanique)	Directeur de thèse

Synthèse

La dynamique de particules inertielles lourdes évoluant dans un fluide présente un intérêt dans de nombreux domaines. On les retrouve dans des phénomènes naturels, comme par exemple les gouttes d'eau dans les nuages, les sédiments dans les rivières et les océans ou les disques d'accrétion planétaire. Mais ils sont également intéressants dans des domaines liés aux activités et technologies humaines, comme par exemple des gouttes de carburant en chambre de combustion, la dispersion de catalyseurs solides dans des réacteurs chimiques ou encore de particules de salives quand des personnes parlent ou éternuent. Ces systèmes sont complexes. Les modèles utilisés pour les étudier utilisent des hypothèses simplificatrices souvent fortes. Pour tester la robustesse de ces modèles, il est donc encore nécessaire de récolter des données expérimentales. Si nécessaire, ces données peuvent également servir à construire de nouveaux modèles, théoriques ou empiriques.

De nombreux comportements ont été observés dans ces écoulements diphasiques dispersés, à la fois dans des simulations et dans des expériences. Cette thèse s'intéresse en particulier à deux de ces phénomènes. En premier le clustering, qui se traduit par le fait que des particules s'accumulent dans des régions spécifiques de l'écoulement et en laissent d'autres vides. Ces inhomogénéités de concentration peuvent être très fortes, la concentration en particules pouvant localement être plus de dix fois supérieure à la concentration moyenne, ce qui a un impact certain sur les probabilités de collision des particules (dans le cadre de la formation de la pluie par exemple). Le second phénomène étudié est l'altération de la vitesse de sédimentation, qui correspond à une augmentation ou une diminution de la vitesse de sédimentation des particules par rapport à une particules isolée tombant dans un fluide au repos. Cette modification de la vitesse de sédimentation a un lien fort avec la capacité des particules à se disperser. Par exemple, dans le cadre de la dispertion d'aérosols, des particules tombant plus vite à terre voyageront sur de plus petites distances. Ces phénomènes sont liés, et dépendent de paramètres comme la taille et la densité des particules, de la phase porteuse (eau ou air généralement) et de si celle-ci est au repos ou dans un état turbulent. Cette dépendance à de multiples paramètres complexifie d'autant plus l'étude des écoulements chargés en particules, et isoler l'impact de chacun de ces paramètres sur les phénomènes étudiés ici est également un enjeu de cette thèse.

Un dispositif expérimental a été construit pour cette étude, dans lequel de petites particules solides (diamètre maximal de $200\mu m$) sédimentent dans de l'eau. Des particules de différentes densités ont été séparées par taille par tamisage. Cette préparation de différentes populations de particules donne accès à une large gamme de paramètres qui serviront à mieux discerner l'influence de chacun d'entre eux. Une technique de double mesure simple à mettre en œuvre permettant de mesurer simultanément la vitesse des

particules et du fluide a été développée. En utilisant un système d'acquisition stereo-PIV et des traceurs fluorescents, une séparation entre traceurs et particules inertielles est effectuée, ce qui permet d'effectuer un suivi des particules inertielles (PTV) et une mesure des champs de vitesse du fluide (PIV). Cette technique donne accès aux interactions particules-fluides, ce qui a rarement été réussi jusqu'à présent. Des augmentations de la vitesse de sédimentation des particules tombant dans un fluide au repos ont été observées et ont été attribuées au développement d'un écoulement descendant qui pousse les particules à tomber plus vite. De manière intéressante, si l'on regarde la vitesse de glissement entre les particules et le fluide, on observe que les particules sédimentent avec une vitesse plus faible qu'attendue dans un référentiel se déplaçant avec le fluide. Une interprétation en terme d'écoulement 'tapis roulant' a été proposée, les particules échangeant de l'énergie avec le fluide pour développer un écoulement à grande échelle. Des analyses de Voronoï ont également été effectuées, mais n'ont pas pu déterminer avec certitude si les particules formaient des clusters ou non. Aucune influence de la concentration locale des particules sur la vitesse de sédimentation n'a été observée pour nos populations de particules.

Ce travail fournit des données intéressantes, pertinentes pour l'étude des particules qui sédimentent dans des fluides au repos en espace clos, étude qui se poursuivra sur les nombreuses populations de particules préparées au cours de cette thèse. Il fournit également un point de référence pour de futurs travaux où la turbulence sera ajoutée au système. Un système de grilles oscillantes a d'ores et déjà été installé et est actuellement en cours de caractérisation dans ce but.

Remerciements

Je tiens d'abord à remercier les membres de mon jury de thèse pour avoir accepté d'évaluer les résultats de mon travail et pour leurs suggestions lors des discussions qui ont suivi ma soutenance. Je remercie en particulier Sebastien Aumaître et Romain Volk pour avoir accepté le rôle de rapporteurs, et Véronique Roig pour avoir présidé le jury lors de ma soutenance.

Je remercie également mon directeur de thèse, Romain Monchaux, d'avoir accepter de m'encadrer pendant ce travail. Je suis heureux d'avoir pu travailler avec lui pendant toutes ces années où il m'a soutenu, conseillé et aidé à avancer.

Un grand merci aussi à Till Zürner pour m'avoir accompagné sur la fin de ma thèse. Le projet n'en serait pas là sans sa rigueur et je garde un excellent souvenir des échanges que nous avons pu avoir.

Merci aussi à Jean-Marc Chomaz pour avoir apporté un regard extérieur sur mon travail et m'avoir remis sur le bon chemin quand j'en avais besoin.

Mon projet de thèse n'aurait pas pu aboutir sans le soutient et l'expertise de nombreuses personnes. Je remercie en particulier Thierry Pichon, Lahcène Cherfa, Nicolas Baudet et Nicolas Thurieau pour leur aide sur de nombreux aspects plus techniques de cette thèse.

Je mentionne également l'AID, qui a ma gratitude pour avoir accepté de financer ce projet, en particulier Emmanuelle Guillot-Combe, Mathilde Bellot-Ayreault et Stephane Burkhart.

Je remercie aussi les personels de l'UME et de l'IMSIA pour tous les moments d'échange et de convivialité que nous avons pu passer ensemble.

Enfin, je remercie mes amis et ma famille qui m'ont soutenus pendant ces années sur les autres aspects de ma vie.

Contents

Chapter 1

Introduction

Particle laden flows are a vast topic covering a wide range of systems. They are a two-phase system in which a dispersed phase, i.e. the particles, evolves in a carrier phase, i.e. a fluid. The properties of both the particles and the carrier phase can vary substantially from one application to the next. These dispersed two-phase flows can for example be found in nature in cloud dynamics where water droplets evolve in air, or in the dynamics of sediments in rivers and ocean. In space, they are also involved in planetary accretion disks where dusts collide and aggregate to form planets in a gas. The study of these systems is also of importance in human activities and technologies. In the chemical industry, heterogeneous catalysis often involve solid catalysts to be dispersed in a fluid reaction medium for example. Spray dynamics generally relate to liquid particles dispersing in air, and are relevant for fuel dispersion in combustion chambers, or the dispersion of saliva droplets when people talk or sneeze. The dispersed phase can also be lighter than the carrying fluid, as is the case for bubbly flows (i.e. gas bubbles in water), relevant to industrial processes and to gas exchanges between the oceans and the atmosphere.

These multiphase flows are complex as many parameters are involved in their description, e.g. particle size, shape, density and concentration, fluid density and viscosity. Different phenomena can be studied depending on the specificities of considered system. For example, if the dispersed phase is a fluid, particles can coalesce or break up, but in the case of solid particles collision can occur. The dynamics of the system will also depend on whether the carrier phase is in a quiescent or turbulent state. Gravity is also an important aspect that often cannot be neglected in these systems, as it causes heavy particles to settle and gas bubbles to rise. Even when restricting ourselves to the case of heavy settling particles, many behaviours have been observed. This thesis and the project in which it is inscribed aim at studying a few of those. The first is

clustering, or the tendency for particles to accumulate in some regions of the fluid while leaving other regions completely void. Understanding how and why clustering occurs is of importance to predict when particles can collide and coalesce, which is crucial to predict rain formation for example. The second is the modification of the settling velocity of the particles. Depending on the system studied (more or less heavy particles, smaller or larger, quiescent or turbulent fluid), particles have been observed to settle at either increased or hindered velocities. Understanding this behaviour is a key in producing more accurate models of particle dispersions in the atmosphere or in the oceans for example, as the particles travel time will depend on how fast they settle. It is important to note that clustering and settling velocity alteration are connected, one often being observed in conjunction with the other.

This thesis was then focused on building an experimental apparatus to study the settling dynamics of small (less than 200 μm diameter length) heavy particles. Only experiments in a quiescent fluid have been performed up to now, characterising how the experimental device behaves and giving insight into how particles settle in an enclosed space. By taking particles of different types and sizes, a large array of parameter values could be accessed to test what is the influence of each parameter and their relative importance. Details on the experiments and how the particle populations were prepared are given in chapter 2. To study the local interactions between particles and fluid, a double-measurement technique has been developed, that allows simultaneous measurement of particle and fluid velocities. This method and its validation process are the topic of an article currently under review for the journal *Experiments in Fluids*, article reproduced in chapter 3. The results obtained from the experiments and their analysis are detailed in chapter 4, and future perspectives of the project will be discussed in chapter 5.

This first chapter will provide an overview of the state of the art to put the present work in its context. A first section will be dedicated to the dynamics of a single particle settling in a quiescent flow. Then the collective effects on the settling velocity of multiple particles will be tackled. Even if there is no turbulence in the experiments presented in this thesis, because the overall goal of the project is to study particles settling in a turbulent flow, the third section of this chapter will discuss the additional effects that arise when turbulence is added. The fourth and final section of this chapter will present the necessary background on the measurement and analysis techniques used in this thesis.

1.1 Single particle settling in a quiescent fluid

Let us consider a spherical particle of diameter d and density ρ_p, settling in a fluid of density ρ_f and kinematic viscosity ν. An important parameter for the system is the density ratio, defined as

$$\Gamma = \frac{\rho_p}{\rho_f}. \tag{1.1}$$

This ratio varies a lot depending on the system considered, and the study of heavy particles in a fluid (i.e. $\Gamma > 1$) is quite different from the study of particles that are lighter than their surrounding fluid (i.e. $\Gamma < 1$). Though some mechanisms definitely overlap, the dynamics of say air bubbles in water at $\Gamma \approx 10^{-3}$ or of oil in water $\Gamma \approx 0.9$ are already different from each other, but differ even more from the dynamics of sand in water $\Gamma \approx 2-5$ or water droplets in clouds $\Gamma \approx 1000$. Because this work is focused on settling particles, $\Gamma > 1$ for all considered cases if not mentioned from now on. The settling particle is subject to three forces : its own weight $\mathbf{F_W}$, buoyancy $\mathbf{F_A}$ and drag $\mathbf{F_D}$. The particle weight and buoyancy can respectively be expressed as $\mathbf{F_W} = -\frac{4}{3}\pi\left(\frac{d}{2}\right)^3 \rho_p g\ \mathbf{e_z}$ and $\mathbf{F_A} = \frac{4}{3}\pi\left(\frac{d}{2}\right)^3 \rho_f g\ \mathbf{e_z}$, where g is the acceleration of gravity, and $\mathbf{e_z}$ is the unit vector of the vertical axis, oriented upward (i.e. opposite of gravity). The expression for the drag force in a quiescent fluid for a sphere is $\mathbf{F_D} = -\frac{C_\mathrm{D}}{8}\rho_f \pi d^2 v \mathbf{v}$ where $\mathbf{v}$ is the particle velocity vector, $v = |\mathbf{v}|$, and C_D is the drag coefficient. C_D is a complicated function that depends on the flow conditions and the particle velocity. In creeping flow conditions, C_D can be theoretically expressed as $C_\mathrm{D} = \frac{24}{Re_p}$ where $Re_p = \frac{vd}{\nu}$ is the particle based Reynolds number. Such theoretical expression are not derivable in non creeping flow conditions and a large number of empirical expressions have been coined for various velocity ranges over the last century. See Brown and Lawler [2003] for an overview. In a lot of instances, these drag models are corrections to the creeping flow theoretical result using experimental data. The drag coefficient can then usually be put in the following form $C_\mathrm{D} = \frac{24}{Re_p} f_\mathrm{D}(Re_p)$, with $f_\mathrm{D}(Re_p)$ being the drag model correction used.

At its terminal velocity, the particle then satisfies the equation:

$$\begin{aligned} 0 &= \mathbf{F_W} + \mathbf{F_A} + \mathbf{F_D}, \\ 0 &= \frac{4}{3}\pi\left(\frac{d}{2}\right)^3 g(-\rho_p + \rho_f) + \frac{1}{8}\frac{24}{Re_p} f_\mathrm{D}(Re_p)\rho_f \pi d^2 v^2, \\ Re_p f_\mathrm{D}(Re_p) &= \frac{1}{18}\frac{(\Gamma-1)gd^3}{\nu^2}. \end{aligned} \tag{1.2}$$

According to the drag model used, the terminal settling velocity of the particle can then be computed using 1.2. For the purposes of this work, two drag models will be

considered. The first is the Stokes drag model, that is theoretically derived from creeping flow conditions, for which we then have $f_D = 1$. A second model that is often used leaving the Stokes regime is the Schiller-Naumann drag: $f_D = 1 + 0.150\ Re_p^{0.687}$ [Schiller and Naumann, 1933]. This empirical correction is valid for $Re_p < 800$.

Studies have shown that the behaviour of a single particle settling in a quiescent fluid varies according to the wake this particle will develop. See Johnson and Patel [1999] for the study of the wake of a fixed sphere, Jenny et al. [2004] for a numerical study of a free falling sphere and Horowitz and Williamson [2010], Veldhuis and Biesheuvel [2007] for equivalent experimental studies, although more focused on rising particles (i.e. $\Gamma < 1$). The behaviour of the particle and the form that its wake will take is entirely dependent on two parameters Jenny et al. [2003]: the density ratio Γ and the Galileo number Ga, defined as:

$$Ga = \sqrt{\frac{gd^3(\Gamma - 1)}{\nu^2}}. \tag{1.3}$$

The Galileo number results from the comparison between the gravity forces and the viscous forces exerted on the particle. It is also analogous to a Reynolds number based on a gravitational velocity

$$v_g = \sqrt{gd(\Gamma - 1)}. \tag{1.4}$$

For further discussion on how it is defined, see Jenny et al. [2004]. As an alternative to the Galileo number, the Archimedes number can also be used :

$$Ar = Ga^2 = \frac{gd^3(\Gamma - 1)}{\nu^2}. \tag{1.5}$$

As the Galileo number increases, four forms of the drag have been identified. For low Ga, the particle will settle with a vertical motion and an axisymetric wake. Then, at $Ga \approx 155$ ($Ar \approx 24000$), a first transition occurs and the particle then settles with a steady oblique motion. This transition presents a first symmetry breaking, where the particle now instead evolves in a symmetry plane formed by the direction of its trajectory and the direction of gravity. At $Ga \approx 185$ ($Ar \approx 34200$), a secondary transition corresponding to a Hopf bifurcation adds an oscillation to the particle movement, without breaking out of the previously mentioned plane. This corresponds to a vortex sheding phase. Finally, above $Ga \approx 215$ ($Ar \approx 46200$), the particle breaks out of the symetry plane, its wake and trajectory becoming chaotic.

Interestingly, equation 1.2 then gives a relation between Re_p (i.e. the terminal settling velocity) and Ar or Ga that then only depends on the choice of the drag model:

$$Re_p f_D(Re_p) = \frac{Ar}{18} = \frac{Ga^2}{18}. \tag{1.6}$$

Given the relatively simpler form of equation 1.6 when Ar is used, the Archimedes number will be used over the Galileo number in the present work.

1.2 Collective effects on settling

The already rich picture becomes even more complex when multiple particles have to be considered. As many particles settle together, they interact with each other's wakes and with the flow they collectively create. In a similar fashion to what has been done in the study of a single particle, many investigations were conducted on the flow structures that develop around fixed particles in various configurations. Tsuji et al. [2003] have performed a numerical study of 2 particles aligned streamwise or side by side against the flow and found that the streamwise configuration reduces drag intensity on both particles while the other configuration increases it. This side-by-side configuration was also studied both experimentally and numerically by Schouveiler et al. [2004] and reached the same conclusions. In these cases, the important parameters affecting how the wake deviate from the single particle case are the velocity of the fluid around the particles and the relative distance between them. These phenomena are the building blocks of larger scale behaviours observed when large numbers of particles settle. With a focus on the study of turbulence induced by bubble swarms, numerical simulations of the flow through arrays of sphere fixed at random positions were performed by Riboux et al. [2013]. Although these simulations did not resolve well the flow near the spheres, they could nonetheless reproduce observed features of bubble swarms, especially on the vertical fluid velocity statistics, but not on the horizontal one. Their conclusion is that the bubble induced turbulence mainly arises from large scale wake interactions. Taking advantage of the fixed positions of the spheres, the fluid agitation could be decomposed in time-averaged spatial fluctuations (mean bubble wakes) and genuine temporal fluctuations (instability of the randomly placed wakes). A following experimental study of such configuration Amoura et al. [2017] reaches similar conclusions, and insists on the importance of distinguishing between the spatial fluctuations, predominant at low flow speeds, and the temporal fluctuations, whose importance rises with the flow velocity.

When the number of particles increases, an additional non-dimensional number expressing the particle concentration, or particle loading, is added to describe the system. Two parameters can be used for that. To simplify the following equations, all particles are considered to be identical in size and mass. The first parameter is the volumic fraction occupied by the particles

$$\Phi_V = \frac{N_p \mathrm{V}_p}{\mathrm{V}_{\mathrm{tot}}}, \tag{1.7}$$

where N_p is the number of particles, V_p is the volume of one particle and $\mathrm{V}_{\mathrm{tot}}$ the total volume considered, i.e. particles and fluid included. The second is the mass fraction of the particles

$$\Phi_m = \frac{\rho_p N_p \mathrm{V}_p}{\rho_f(\mathrm{V}_{\mathrm{tot}} - N_p \mathrm{V}_p) + \rho_p N_p \mathrm{V}_p}. \tag{1.8}$$

Given their expressions, Φ_V and Φ_m are linked with the relation:

$$\Phi_m = \frac{\Gamma \Phi_V}{1 + (\Gamma - 1)\Phi_V}, \tag{1.9}$$

so either one can be used to characterise the system.

Whatever the chosen parameter, this estimation of the particle concentration remains a global, average parameter. However, the local concentration around each particle can still deviate a lot from this average. In contrast with the previously cited studies where the particles' positions are fixed, freely moving settling particles can form regions of higher concentration while leaving other areas of the fluid completely void. This effect of an inhomogeneous concentration field appearing from an initially homogeneous particle distribution is called clustering. How these structures of low and high particle concentration form, and in what measure are they linked to potential modifications of the settling velocity of the particle are active research topics and are the main study goal of this thesis.

Under very dilute conditions (i.e. $\Phi_V < 10^{-4}$), particle behaviour stays unchanged and flow statistics can quite accurately be predicted by considering a linear superposition of the particles' individual wakes for the contribution of the settling phase. This was observed both experimentally and numerically [Parthasarathy and Faeth, 1990a,b]. These observations can be linked with fixed positions studies where particles far apart from one another no longer influence each other, which is similar to the dilute conditions mentioned here.

For higher particle loadings, many numerical studies were performed with particles settling in a turbulent flow, and those will be discussed in section 1.3. However, fewer studies focused on particles settling in a quiescent fluid. Uhlmann and Doychev [2014] performed such numerical simulations for two Archimedes numbers, $Ar \approx 14600$ and $Ar = 31700$, at a particle loading of $\Phi_v = 5 \times 10^{-3}$ and $\Gamma = 1.5$. These two Archimedes numbers were chosen to fall in the steady vertical and steady oblique settling regimes identified for a single particle, as defined in section 1.1. In the higher Ar case, they observed that particles would form columnar structures, as particles then tend to follow each other when settling. This was not observed in the lower Ar case. Additionally, they found that particles settling in the columns had a higher settling velocity than that of an isolated particle with the same parameters. Going from the results obtained for single

particle settling, they interpreted it as a result of the oblique trajectories increasing the likelihood of particles crossing paths and becoming 'trapped' in one another's wakes. As this configuration has been shown to reduce the drag force experienced by the particles, particles then settle at enhanced velocities. Fornari et al. [2016] have also performed numerical simulations without turbulence to compare them with results obtained with turbulence. In their case, volume fractions of $\Phi_V = 5 \times 10^{-3}$ and $\Phi_V = 10^{-2}$ were used with particles of parameters $\Gamma = 1.02$ and $Ar = 21000$. They report a slight decrease in the settling velocity of the particles in quiescent case due to a strong intermittency arising from particle-particle interactions. They observe no clustering either, which is in line with the observations and interpretations of the previous numerical work.

Unfortunately, experimental studies of particles settling in an initially quiescent fluid are also rare. With the goal of expanding the parameter space already studied by Uhlmann and Doychev [2014], Huisman et al. [2016] performed an experimental study of glass particles settling in a fluid column of 2 m height and square-cross section of sides 0.3 m. Using 3D particle tracking, they had access to particle positions and velocities. In their case, $\Gamma = 2.5$, but by varying the size of the particles and the viscosity of the fluid, they were able to cover four Archimedes numbers ranging from $Ar \approx 12100$ to $Ar \approx 96100$, one for each type of trajectory for a single particle settling. Their experiments were manually seeded by pouring particles on top of a stack of meshes, resulting in particle loadings between $\Phi_V = 10^{-4}$ and $\Phi_V = 10^{-3}$. Their results add a bit of nuance to what was established by Uhlmann and Doychev [2014]. First, even particles that should settle vertically (i.e. lower Archimedes numbers) present mild clustering, which they suspect might come from large scale flow that develop due to the geometry of their experiment, as particles fall in a constrained environment that is different from the boxes with periodic boundary conditions of numerical simulations. Secondly, as they performed experiments with higher Ar, they observed that although clustering intensifies as Ar increases, the settling enhancement do not follow that trend. Instead, it peaks for their $Ar \approx 40000$ cases and decreases for $Ar \approx 96100$. By comparing with the results of Uhlmann and Doychev [2014] they conclude that, although it certainly plays a role, the regime of a single settling particle in itself is not enough to predict the behaviour of multiple particles settling together. This is because changing boundary conditions provoked the apparition of clustering in experiments, while this was not observed for numerical simulations with similar Ar and Φ_V.

This influence of the interaction with the flow and how it develops due to physical constraints prompts Huisman et al. [2016] to emphasize the importance of having access to the velocity field of the fluid in addition to data from the particles, to get a better picture of the phenomena observed. Numerical simulations give access to data from both phases, but extensive parameter studies remain difficult to perform due to computational time.

In physical experiments, it is arguably easier to achieve a broader range of parameters, but the data is incomplete, often missing one of the two phases or being limited to measurements at a point (e.g. Laser Doppler Velocimetry) or a plane (laser sheet). For example, Uhlmann and Doychev [2014] report an interesting finding linking fluid and particle velocity. In their case, when particles fall at higher velocities than expected, those particles not only are in regions of downward fluid flow, but subtracting the velocity of the fluid from the velocity of the particle gives back the expected settling velocity for a single particle. In essence the particles develop a flow where columns of fluid have higher downward velocities and this velocity is what pushes them and enhances their settling speed. This study however requires the definition of a slip velocity between the particles and the fluid. How this can be achieved will be discussed in section 1.4, along with an overview of experimental techniques that can be used to access data from both phases.

1.3 Toward turbulence

When the particles settle in a turbulent flow, the complexity increases yet again. The fundamental equations for a single particle evolving in a turbulent flow were established a long time ago [Gatignol, 1983, Maxey and Riley, 1983]. However, these already complex equations were derived in the limit of very small particles submitted only to a Stokes drag, i.e. for vanishing Re_p. In most cases, systems of particles evolving in a turbulent flow do not fit these hypotheses and model equations, often simpler than the ones proposed by Gatignol [1983], Maxey and Riley [1983], have been used, both to describe experimental observations and as an input for numerical simulations.

To describe the system with turbulence, several parameters are then also added. First of all, the Reynolds number is used for quantifying the intensity of the turbulence in the fluid. Various length scales can been used for its definition. A popular choice is the Reynolds number based on the Taylor micro-scale λ, an intermediate scale of turbulent structures (see Pope [2000] for definition). This Reynolds number is then expressed as:

$$Re_\lambda = \frac{u'_{\text{rms}}\lambda}{\nu}, \tag{1.10}$$

where u'_{rms} is the root mean square of the fluid velocity fluctuations.

The Stokes number is also of importance here

$$St = \tau_p/\tau_f, \tag{1.11}$$

and compares a particle response time τ_p to a given time scale of the flow τ_f. It gives a measure of particle inertia, as for $St \gg 1$ particles present a ballistic motion and ignore the flow, and for $St \ll 1$ particles are completely carried by the flow. Interesting effects can then occur at intermediate values, and it has been observed that, for sub-Kolmogorov particles, clustering and settling velocity enhancement often peak for $St \approx 1$, because fluid and particle motions are then more in phase. For more details, see the experiments of Yang and Shy [2003]. The particle response time is often derived from the drag model used, and sometimes also accounts for added mass effects. For the fluid time scale, the choice depend on the particle size. Because particles of different sizes do not sample the same flow structures, the related flow time scales are also different. For particles smaller than the Kolmogorov scale, the Kolmogorov time scale is used.

To account for the effects of gravity, the Froude number F is sometimes used, as it compares the strength of turbulence to the effects of gravity on the flow. Alternatively, the Rouse number Ro can also be used. It compares the terminal settling velocity of a particle with a characteristic flow velocity. The root mean square of the fluid velocity fluctuations can be used:

$$Ro = \frac{v_t}{u'_{\text{rms}}}, \tag{1.12}$$

but the Kolmogorov velocity u_η is also used in some instances, and the Rouse number is often called settling parameter Sv in these cases.

The previously defined density ratio Γ is of course still of importance, and if a large number of particles are in the considered system, Φ_V and/or Φ_m also have to be used in its description.

Throughout the experimental works and numerical simulations performed on settling particles, a variety of effects have been observed, such as clustering and settling velocity increases or decreases. To explain these effects many mechanisms have been proposed. These mechanisms will be briefly evoked here, and a more detailed overview of these mechanisms can be found in Sumbekova [2016].

To begin, mechanisms involving the interaction of a particle with the flow in itself will be listed. A first mechanism is the fast-tracking, or preferential sweeping effect [Maxey, 1987, Wang and Maxey, 1993], where particles swept around vortices preferentially sample regions of downward fluid motion and thus present enhanced settling velocity. An opposite effect would be the loitering mechanism, where, if a particle settle with a relatively vertical motion, it will traverse turbulent eddies, with both regions of upward and downward fluid velocity [Nielsen, 1993]. But because upward fluid velocity regions will slow it down, the particle will spend more time in those regions. Overall, the expected result is a lower settling velocity, when compared with a non turbulent case.

These two mechanisms compete in their effects but recent numerical simulations suggest that loitering do not supersede preferential sweeping, at least for sub-Kolmogorov heavy ($\Gamma \approx 1000$) particles [Rosa et al., 2016]. The fluid acceleration field can also have an impact, as, along its path, the particle will not only experience changes in the fluid velocity, but also in the acceleration of the carrier phase. Numerical simulations have found a correlation between not only particle and fluid velocities, but also between particle velocity and fluid acceleration [Dejoan and Monchaux, 2013]. A final mechanism that can be cited is the sweep-stick mechanism. It was theorised in the context of clustering of particles in a turbulent flow without gravity, and stipulate that particles cluster as they stick to points of the fluid without any acceleration. In a gravity field, particles would be expected to stick to points of the fluid with an acceleration equal to gravity g, which has been confirmed by numerical simulations [Hascoët and Vassilicos, 2007], with an additional observation that the clusters formed by the particles can then present a different shape due to gravity (elongated in the direction of gravity). Because of that, it can be expected that the altered cluster dynamics also change the settling velocity of the particles.

All the mechanisms discussed in the previous paragraph only consider how the particles react to the flow. Although they certainly play a role in the dynamics of a dispersed two-phase flow, the way particles interact and modify the flow in return are also an important part in understanding these complex systems. The distinction between those two cases is clear in the numerical experiments. The numerical studies cited for these mechanisms here all used so-called one-way simulations, where the particles only respond to the flow structure. Other simulations, called two-way, more difficult to implement, have also taken a back reaction of the particles into account. It is important to note that an additional step in complexity can be taken if particle collisions are taken into account, then named four-way, but this case will not be discussed further here. Because particles can now affect the flow, it is also expected that the particle loading Φ_V or Φ_m can now influence the results. As the particles have an action on the flow, they modify its structures and if multiple particles are present, they will then impact how other particles behave.

Two-way simulations where the particles have a finite size were performed by Kajishima and Takiguchi [2002], for $\Phi_V = 2 \times 10^{-3}$, $\Gamma = 10$. They found that particles would form clusters in the turbulent flow through their wake interactions, and described a life cycle for the clusters. For velocities high enough for the particles to provoke vortex shedding ($Re_p = 300$, here based on a slip velocity), the particles' wakes enables them to interact with other particles. This leads particles to group up, thus forming clusters. Because particles in a cluster are in the wakes of others, the drag they experience is lower and the particles in the cluster fall faster. As they accelerate downward, they also

accelerate the fluid around them, and generate additional turbulent eddies. This ends up destabilising the cluster and particles then separate. A follow up study including the effect of particle rotation was also performed [Kajishima, 2004] and found that rotational particles tend to break from cluster structures more easily. The work from Fornari et al. [2016] included simulations both with and without turbulence in the fluid for finite-size spheres. When comparing these two cases they found that the added turbulence actually reduced the settling velocity of their particles. Monchaux and Dejoan [2017a] also performed two-way numerical simulations, of heavy ($\Gamma = 5000$) point particles in this case, and found an increase of the settling velocity in turbulence. Here, although the system was dilute enough that particles did not influence the overall statistics of the turbulent flow ($\Phi_V = 1.5 \times 10^{-5}$ to $\Phi_V = 7 \times 10^{-5}$), the back-reaction of the particles on the fluid changed the local flow structures around them. The falling particles locally accelerate the fluid downward, and fluid and particles end up settling together.

Experiments on particles settling in turbulence have also been performed. In their study of water droplets evolving in a wind-tunnel grid turbulence, Aliseda et al. [2002] observed that not only particles settled faster than expected, but particles with a higher local concentration of particles around them settled faster than more isolated particles. This lead them to formulate the hypothesis that particle clusters would act as meta-particles which would be responsible for the enhanced settling velocities of the particles they observed. The observations made in the numerical works of Monchaux and Dejoan [2017b] agree with this hypothesis, since the authors found that both the fluid and the particles settle at the same speed. The specific effects of particle loading have been more recently studied by Huck et al. [2018], also for water droplets in a wind tunnel. Different regimes have been identified in these experiments: isolated particle response for $\Phi_V < 10^{-6}$, preferential sweeping effects at $\Phi_V \approx 10^{-5}$, then clustering with a saturation of the settling velocity enhancement for $\Phi_V \approx 10^{-4} - 10^{-3}$. Their observations also corroborate that as a whole clusters generate local downward forces that are superior to non clustering regions, further cementing the role of clusters in settling velocity enhancement for small particles. Petersen et al. [2019] have studied solid particles settling in air ($\Gamma \approx 100 - 2500$), in a chamber where homogeneous isotropic turbulence is achieved with random air jets. Their experiments confirm that clustering is most intense for $St \approx 1$, but also that particles with $St > 1$ cluster over larger regions. They also observe a threefold increase of the settling velocity of their particles with respect to the terminal velocity in a quiescent fluid.

Recent theoretical results have focused on extending the framework laid by Gatignol [1983], Maxey and Riley [1983]. Tom and Bragg [2019] were notably able to find results for particles of finite inertia, while previous equations were also limited to $St \ll 1$. They report that flow structure that affect a particle depend on its inertia. As St

increases, progressively larger and larger flow scale have to be considered to account for the increase in velocity that the particles exhibit. This indicates that a multi-scale mechanism is responsible for the alteration of velocity of falling particles, which they confirmed with numerical simulations. They put an emphasis on the distinction between preferential concentration and clustering. Those two terms are sometimes used equivalently but reflect different concepts that should not be confused. Clustering is a pronounced inhomogeneity in the particle concentration field, often characterised as the tendency for particles to form regions of high and low concentrations more often than what would be expected of a random uniform distribution of the same particles. Preferential concentration on the other hand is when particle positions correlate with properties of the flow. For example, they also show that for $Fr \ll 1$ and $St = O(1)$, particles do not cluster, i.e. no inhomogeneity of the particle concentration field, but they still exhibit an increased settling velocity. That is because, in that case, while particles do not preferentially sample the fluid flow at small scales, they still do it at larger ones.

1.4 Measurements and analysis techniques

This section will introduce some general concepts surrounding the measurement techniques used in the present work, as well as some important discussions regarding the analysis of settling dispersed two-phase flows.

Fluid measurement techniques are varied and can be adapted to many experimental devices. In this work, Particle Image Velocimetry (PIV) was used to obtain flow velocities. In its two dimensional form, a Laser sheet lights tracer particles in the flow and images of these tracers are taken at regular time intervals. These images are then divided in smaller interrogation windows, and a cross-correlation is performed on each interrogation window between successive images, giving a displacement in each window. This gives access to an Eulerian velocity field of the fluid, assuming of course that the particles on the images are all tracers. For a more in depth review of this measurement technique, see Adrian and Westerweel [2011]. This technique is now widely used, and commercial solutions are quite readily available.

For the inertial particles velocities, tracking techniques can be used. The Particle Tracking Velocimetry (PTV) is a Lagrangian measurement technique that also uses successive images of particles. Here, the general idea is to first identify each particle individually in each image. Once the positions of the particles are obtained, a matching step links the positions found in the two images. In its simplest form, the position taken is the closest one. This gives a displacement of the particles between the images, which corresponds

to their velocity. Performed on successive images, this gives access to particle trajectories. Some algorithms refine particle matching between frame using the previously computed displacements to predict where the particles should be in following frames, thus increasing the accuracy of this particle matching step.

As said in section 1.2, it is important to have access to both fluid and particles velocities to fully grasp the dynamics of the systems at stake here. Both PIV and PTV are widely used and available experimental techniques nowadays. They are commercially available and can be used with similar set-ups, i.e. a system of camera(s) and a Laser sheet. Their simultaneous use however poses difficult challenges that must be overcome to get the velocities of both the dispersed phase and the carrier fluid. The crucial point here is to develop ways to separate the tracers from the inertial particles. This has been worked on for decades now [Towers et al., 1999], and many different measurement techniques have been proposed, though no universally applicable technique has been proposed up to now. In most cases these techniques rely either on a difference in size or apparent intensity between the particles and the tracers. More details on the different measurement techniques proposed in the literature are provided in section 3.1. Because these techniques do not fit the parameter space that this thesis aims at studying (tracers and particles of similar size and/or intensity in the images), a new measurement technique had to be developed, and is the topic of chapter 3.

Once those measurements are done, an important aspect of their analysis is to measure the concentration field of the particles, to search for links between clustering and the properties of both phases (e.g. particle and fluid velocity, acceleration, vorticity field...). A first technique that can be used is a simple box counting. The particle field is divided in equally sized boxes and the particles are counted in each box to obtain their concentration field. If this technique is simple to implement, it however induces a bias, as choosing boxes of different sizes will probe the concentration field with a bias linked to the size chosen for the boxes. Voronoï diagram analysis are also used nowadays. This technique divide the space by associating a single and unique region to each particle, with the property that all points in a given region are closest to the particle contained in said region than to any other particle. These unique volumes can then be interpreted as an intrinsic measure of the local concentration of each particle, as particles in a larger (resp. smaller) region correspond to a low (resp. high) local concentration. This type of analysis provide a local insight on the particle distribution that can be used to identify particle clusters and voids in an unbiased way [Monchaux et al., 2012]. For this reason, the particle concentration fields will be computed using a Voronoï diagram analysis in this work.

When discussing whether a specific system exhibits enhanced or hindered settling velocities, an important question is also the choice of a reference for the particle velocity. As shown in the previous sections, many different systems can be considered, and the picture on a 'simple' sphere settling in a quiescent fluid is already rich. The settling velocity of a sphere assuming a Stokes drag model has been used for reference. This velocity is easy to compute and makes comparison between different publications easier as people then use a common reference point. However, the physical conditions for this model to be valid (creeping flow conditions) are extremely rare and often absent from most studied systems of dispersed two-phase flows (e.g. water droplets in air or solid particles in air or water). Because changing the drag model obviously changes the settling velocity obtained, this choice has an impact on whether the particle settling velocity measured in the experiments will be considered as enhanced or hindered. Moreover given the complexity of dispersed two phase flows, it can sometimes be hard to distinguish between collective effects and effects that arise from flow turbulence for example. In this regard, the settling velocity of an ensemble of particles in a quiescent fluid can also be used as a reference for the settling of particles in turbulence, as was done numerically by Fornari et al. [2016]. In addition to studying the mechanisms at play for the settling of particles in a quiescent fluid, the work presented here will also serve as a basis to compare how the same particles behave when turbulence is added in future studies.

Finally, an important question is also that of the fluid flow "seen" by each particle, which correspond in effect to how the slip velocity between particles and fluid is computed. Bagchi and Balachandar [2003] have proposed in their numerical simulations two definitions for the flow 'seen' by the particles: either the fluid velocity at the particle's position in a companion particle free simulation, or as the average of the fluid velocity on the surface of a sphere surrounding the particle. The first definition makes sense in the context of turbulence modulation by the presence of particles, but is not particularly relevant in the context of particles settling in a flow that they create themselves, the fluid being quiescent otherwise. For this reason the second definition has been more used in the context of numerical simulations of finite size particles [Kidanemariam et al., 2013, Uhlmann and Doychev, 2014]. For numerical simulations of point particles, an interpolation of the fluid velocity at the particle position can also be used (like in the work from Dejoan and Monchaux [2013]). These questions on numerical simulations are also relevant to experimental data. It is obviously difficult in an experiment to get the data for an identical flow realisation without particles, so the first proposition of slip velocity is then never used. Whether the slip velocity will be computed in a manner similar to Kidanemariam et al. [2013], Uhlmann and Doychev [2014] or Dejoan and Monchaux

[2013] depend then more on the spacial resolution of the system for the fluid flow compared to the particle size. For example, if the particles are large enough that the flow around them can be resolved accurately, averaging the fluid on the surface of a sphere (or circle in 2D) around them is feasible. If the fluid measurements do not have a spatial resolution that allows to make out the details of the flow around the particles, then the fluid velocities are already averaged over scales that are larger than the particles size, and using interpolation schemes or a simple nearest neighbour approach are more sensible. Because results from the experiments presented in this work fall in that last category, the nearest neighbour approach has been chosen for slip velocity computations (see section 2.3.2).

Chapter 2

Materials and methods

2.1 Particle populations

This section will describe the inertial particles used and how they are prepared for the experiments.

The project aims at disentangling the effects of the various non dimensional numbers that govern dispersed two-phase flows, and fine-tuning these parameters requires access to particles of various densities and sizes. The method chosen was then to acquire 'bulk' particle populations of different densities covering a range of particle sizes, and to then sieve them to obtain the final particle populations to use in the experiments. A total of 5 particle materials were selected for their range of densities and commercial availability. In order of increasing density these are: glass, ceramic, steel, inconel (a nickel and chromium based alloy) and tungsten carbide. This is summarised in table 2.1.

Material	Label	ρ_p [kg.m^3]	Γ
Glass	GLA	2 500	2.5
Ceramic	CER	4 000	4.0
Steel	STE	7 500	7.5
Inconel	INC	8 440	8.44
Tungsten carbide	TUN	15 630	15.63

TABLE 2.1: Properties of the particles used in the experiment: material, short label, mass density ρ_p and density ratio $\Gamma = \rho_p/\rho_f$ (using $\rho_f = 1000\,\text{kg.m}^3$). For the actual population sizes after sieving see table 2.2.

Each population received a unique denomination made of a three letters label for the material the particles are made of, followed by their minimal and maximal diameters in µm. For example, CER 125-250 is a population of ceramic particles of diameters ranging from 125 µm to 250 µm.

As one goal of the project as a whole is to study the dynamics of sub-Kolmogorov inertial particles in a turbulent flow, the size of the particles needs to be smaller than the Kolmogorov scale of the turbulence that the experimental device will produce. For this reason, the maximal diameter for the particles is set to 200 µm. In consequence, a set of sieves with mesh aperture 20 µm, 32 µm, 40 µm, 50 µm, 63 µm, 75 µm, 90 µm, 106 µm, 125 µm, 140 µm, 160 µm, 180 µm and 200 µm was used to sieve the bulk population. These sieves have a diameter of 100 mm, chosen to also fit the experimental set-up that will be described in section 2.2. For ease of reference, sieves will be referred to by their aperture, so sieves 020 and 125 are the sieves with mesh aperture of size 20 µm and 125 µm respectively. Table 2.2 lists all the bulk populations acquired and the particle populations that can be obtained from them given the sieves at our disposal.

Raw population	Sieved population diameter range [µm]														
	from	0	20	32	40	50	63	75	90	106	125	140	160	180	200
	to	20	32	40	50	63	75	90	106	125	140	160	180	200	∞
GLA 150-250												(✓)	✓	✓	(✓)
GLA 090-150									✓	✓	✓	(✓)			
GLA 053-106						✓	✓	✓	✓						
GLA 000-050		(✓)	✓	✓	✓										
CER 125-250											✓	✓	✓	✓	(✓)
CER 070-125							(✓)	✓	✓	✓					
STE 120-300										(✓)	✓	✓	✓	✓	(✓)
INC 045-090					(✓)	✓	✓	✓							
TUN 045-090					(✓)	✓	✓	✓							
TUN 000-045		(✓)	✓	✓	(✓)										

TABLE 2.2: Size ranges of available particle populations. Ticks in parentheses denote populations that do not sufficiently cover the whole range of diameters given in the table header or that do not have well defined boundaries. These were not used in the experiments presented in this thesis. Additionally, these population were observed to present less spherical particles, as can be seen in figure 2.1 Although all of these populations are obtainable and many have already been sieved, they have not all been used for experiments yet. The ones for which experiments have been performed are marked in red here.

The sieving is performed on a commercial sieving machine (AS 200 digit, from Retsch), using a dry sieving protocol. This protocol was defined following advice from the sieving machine manufacturer and information found in Allen [2003]. For each particle population, the sieving operations, i.e. vibration amplitudes and sieving time on the machine, are first tested to ensure the sieving is properly carried out. A stack of sieves of increasing mesh aperture is placed on the sieving machine, and an initial mass m_i of the population to sieve is put on the top sieve. The sieving is first done in increments of 5 minutes, each sieve being weighted with the particles on it at the end of these 5 min

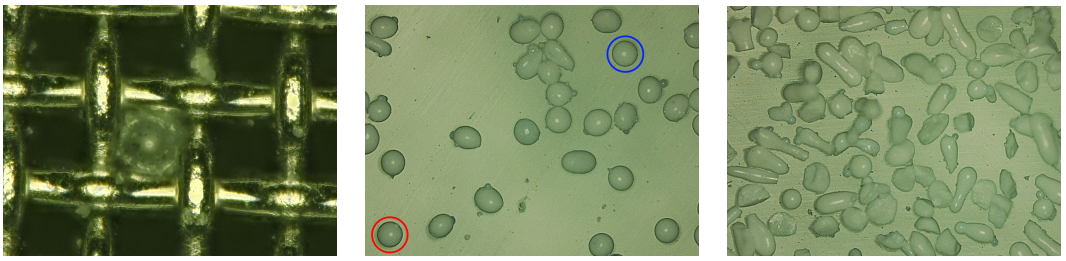

(A) (B) (C)

FIGURE 2.1: Images of particles taken with an optical microscope. (A): glass particle of diameter slightly greater than 50 µm stuck in the mesh of sieve 050, ×1000 magnifying. (B): particles of population CER 125-140, ×100 magnifying. The particle circled in red has a measured diameter of 139.7 µm and the one circled in blue is measured at 130.5 µm. Particles are mostly spherical with some being a bit oblong. (C): particles from bulk population CER 125-140 that went through sieve 125, ×100 magnifying. Due to their non spherical shapes and the lack of well defined lower diameter boundary, these were not used in experiments.

steps. The sieving is considered as finished when the mass of particle on each sieve does not changes by more than 0.5% of m_i after a 5 min operation. Subsequent sieving procedures on the same particle populations are then executed directly using the time necessary to reach the end of sieving criterion, with an additional 5 min for safety, without weighting the sieves every 5 min. This is done to speed up the sieving processes. For example, if the criterion is met after 25 min, the ensuing sieving sessions on the same particle population would directly be performed over 30 min.

After each sieving session, the sieves are inspected, and then cleaned in an ultrasonic bath if the sieving operation has left them too clogged, as particles get stuck in the sieve's mesh. This is done to prevent the sieves from clogging too quickly. Then they are dried, either in an oven at 50 °C for at least one hour if they are to be reused in the same day, or overnight at room temperature. Due to the size of the sieves, several sieving processes have to be completed to obtain sieved populations in quantities suitable to perform experiments.

Example photos of some particle are presented in figure 2.1. All particles ordered were selected to be reasonably spherical, although a small variability in their shape is to be expected. The particle manufacturer can generally only guarantee that for each particle population most particles are in a given range of diameter, but every particle population will still have a portion of particles outside these boundaries. These particles, in addition to being outside the prescribed diameter range, often stray further from the ideal of a spherical particle. For example, see the particles obtained below sieve 125 when sieving CER 125-250 in figure 2.1c.

As all particle populations are given with a range in diameter, an effective diameter will be computed for each of them as a weighted average:

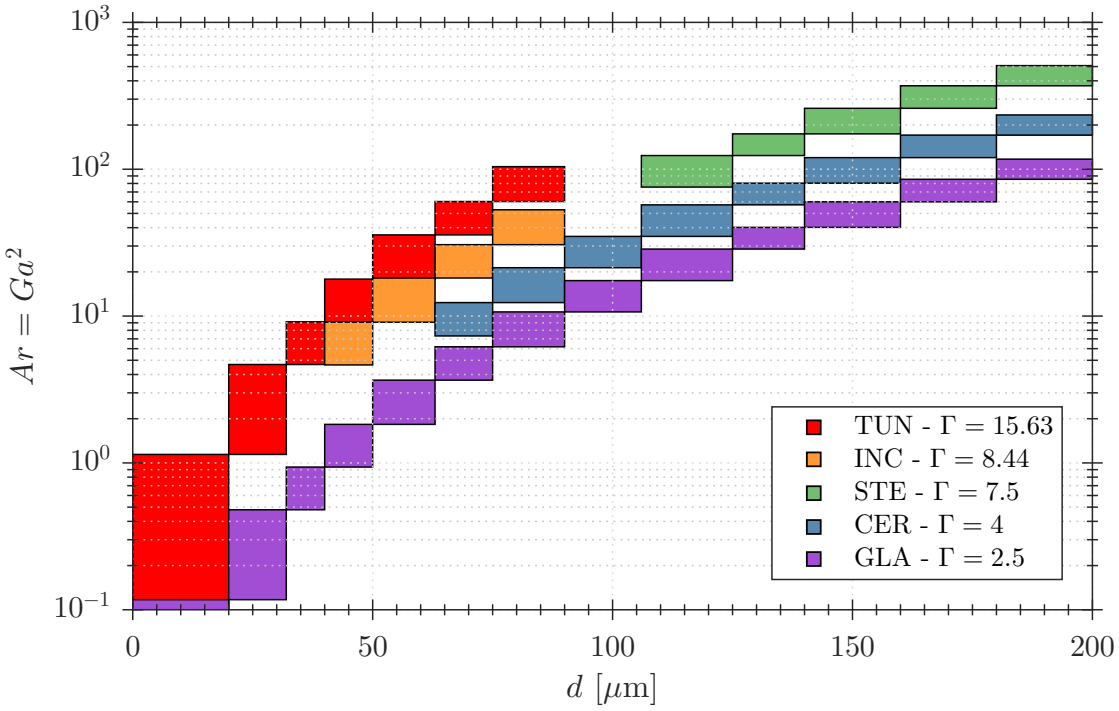

FIGURE 2.2: Archimedes numbers of all particle populations listed in table 2.2, computed at the effective diameter $\bar{d}$. The two particle population with a lower diameter limit of 0 have boxes that extend to $Ar = 0$, which are cropped here due to the logarithmic scale on the vertical axis. All Ar numbers computed correspond to Galileo numbers $Ga = \sqrt{Ar}$ that remain well below the transition value Ga ≈ 155 [Huisman et al., 2016]. So any particle from our populations, if isolated in a quiescent fluid, is expected to settle vertically with a steady wake.

$$\bar{d} = \frac{\int_{d_{min}}^{d_{max}} x w(x) dx}{\int_{d_{min}}^{d_{max}} w(x) dx}. \tag{2.1}$$

Assuming an equal distribution in the number of particles over the particle population range, the weighting function is taken as the particles' volume $w(d) = \frac{1}{6}\pi d^3$, and so:

$$\bar{d} = \frac{4}{5} \frac{{d_{max}}^5 - {d_{min}}^5}{{d_{max}}^4 - {d_{min}}^4}. \tag{2.2}$$

Figure 2.2 shows the Archimedes numbers of the particle populations obtainable after sieving our bulk populations, computed at their effective diameters $\bar{d}$. Overall, they vary between $Ar = 0$ and $Ar \approx 508$. In terms of Galileo numbers, this is between $Ga = 0$ and $Ga \approx 23$. Those numbers correspond to Galileo numbers that are well below the first threshold value Ga ≈ 155 for the wake transition described in section 1.1. This suggests that in our case, preferential concentration, if it were to be observed, would probably not be the result of particle wake interactions.

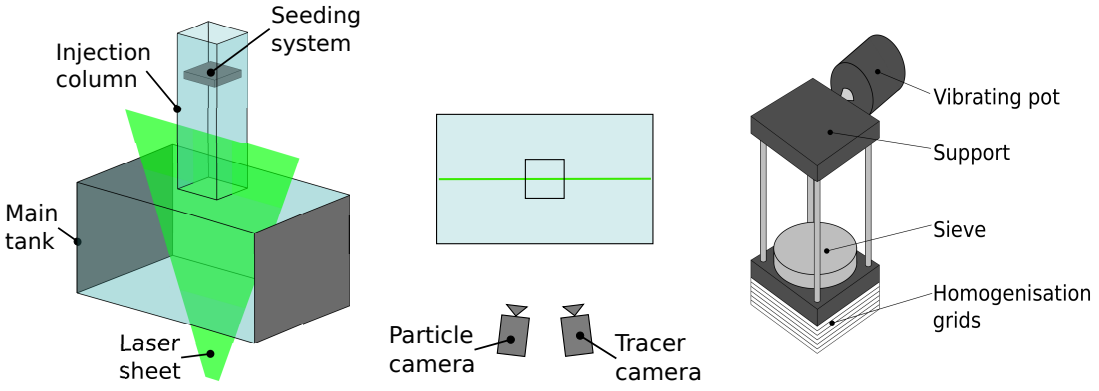

FIGURE 2.3: Diagram of the experimental set-up. (A): Perspective view of the experimental set-up. Only the bottom part of the seeding system is represented here. (B): Top view of the experimental set-up. (C): Diagram of the seeding system.

2.2 Experimental set-up

2.2.1 Device

Figure 2.3 shows a sketch of the experimental set-up. The water tank is composed of two parts: a main tank of size $350 \times 480 \times 350\,\mathrm{mm}^3$, and a square column on top, of dimension $130 \times 130 \times 410\,\mathrm{mm}^3$. Particles are injected through the top column.

The seeding system is of critical importance, especially in the case of experiments in an initially quiescent fluid as particles cannot be picked up from the bottom of the tank by turbulent eddies. An illustration of the seeding system can be found in figure 2.3c. It is composed of a vibrating pot linked to a support on which a sieve can be placed. The vibrating pot is attached to the top part of the support, while the sieve is placed on the bottom part. Particles are deposited directly on the sieve and fall in the tank by actioning the vibrating pot. Under the support, a stack of grids of mesh aperture 1 mm is placed to help homogenizing the clouds of particles falling from the sieve. The bottom part of the support is lowered inside the injection column so that the sieve and the stack of grids are submerged underwater. This is done so that, during experiments, particles do not have to cross the free surface of the water, where they could get stuck and form rafts due to surface tension effects. This system allows to control the quantity of particles injected to a certain degree by tuning the entry parameters of the vibrating pot: function used (e.g. sine wave or square function), amplitude and frequency. However, the particle loading Φ_V of an experiment depends on many other factors, such as the quantity of particles left in the sieve or which sieve is used with a given particle population (e.g. sieve 180 and sieve 200 can both be used for CER 160-180). For these reasons, Φ_V is

estimated after experiments are performed and should be viewed as an output parameter for the experiments.

A key point of the thesis is to put in place a way to perform double-measurements that can simultaneously perform inertial particle tracking and PIV on the fluid. The observations are carried out in the main tank. A Laser of wavelength 532 nm shoots a vertical sheet from the bottom of the set-up, and acquisitions are made with a two-camera LaVision stereo PIV system. The two cameras are identical 12 bits CMOS camera of 1700 x 2375 pixel^2 (Imager SX 4M by LaVision). One camera is used to make observations on the inertial particles, while the purpose of the other is to make measurements on the fluid when tracers are used in the experiments. The cameras are then respectively called particle camera and tracer camera. The tracers used for fluid velocimetry measurements are coated with a rhodamine layer, a fluorescent dye that absorbs light from the laser to emit it back at a peak wavelength of 568 nm. The tracer camera is equipped with an optical filter that cuts light with a wavelength below 570 nm to isolate only the light emitted by the rhodamine coated tracers through fluorescence. This way, the signal from the tracers can easily be separated from the signal of the inertial particles. However, the particle camera sees the signal from both particles and tracers. How particles are distinguished from tracers is the topic of chapter 3.

2.2.2 Calibration

This section describes the calibration process, and the associated error on the measurement of vertical velocities.

The first step in the calibration procedure is to align the Laser sheet with the vertical direction, i.e. gravity. This is done using a bubble level, which here gives an estimated angle error of 1.0° at worst, resulting in an error on vertical velocities of 0.015%. The calibration of the system is then performed using a dotted plate, like shown in figure 2.4. The plate is first positioned to be in the center of the experiment and aligned with gravity using a plummet. To obtain an upper limit of the error on the vertical velocity introduced here, the alignment is considered to at worst result in the dots on a vertical line of the calibration plate to be on either side of the plummet thread (see figure 2.4b). This lead to a maximum error angle of 0.65° which results in an error on vertical velocities (i.e. aligned with gravity) of 0.007%. Afterwards, using specific holes, the calibration plate is adjusted to line up with the Laser sheet (see figure 2.4c). Here, the worst case in alignment leads to an error angle of 1.6°, so an error of 0.04% on vertical velocities.

Both cameras are calibrated at the same time on the plate using the LaVision DaVis 8.4 software. To increase accuracy and improve the superposition of both cameras field of

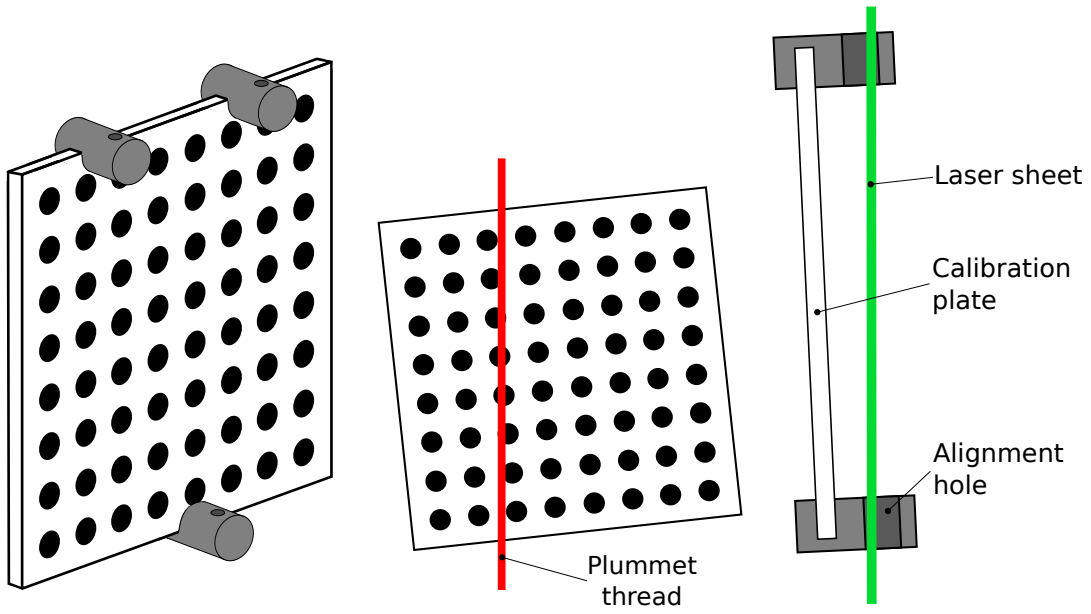

FIGURE 2.4: Diagram of the calibration plate and of the alignment procedures with gravity. The diagrams for the alignment processes are represented here with what is considered as the worst case when performing the calibration. (A): Perspective view of the calibration plate with the Laser sheet alignment holes. (B): Vertical alignment of the plate using a plummet. (C): Alignment of the plate on the Laser sheet.

view, the self-calibration algorithm implemented in DaVis was also employed. Essentially, this procedure consists in performing a cross-correlation on images of tracers from both cameras after doing a usual stereo calibration. The discrepancies measured are then used to correct the calibration model and recenter the images from both cameras. For more information on this calibration procedure, see Wieneke [2005]. Another advantage of this procedure is to be able to recover differences in the alignment between the calibration plate and the Laser sheet, as it also fits the calibration model back on the Laser sheet.

In any case, considering all sources presented here, the calibration gives a maximal error of 0.06% on the measurement of vertical velocities. This is below the standard error for PIV measurements. Across all experiments, the calibration resulted in a scaling factor ranging from 13.4 pixel/mm to 13.7 pixel/mm.

2.3 Experiments

2.3.1 Acquisitions

Two types of experiments were performed: particle only experiments and double phase measurement experiments. In the first case, no tracers are put into the experimental

device. This allows for experiments that are easier to process while still providing useful data and were mainly performed while the double measurement process of chapter 3 was still under development. Double phase measurement experiments had both falling particles and tracers inside the tank, to obtain tracking data from particles and measure the fluid velocity field simultaneously.

For particle only experiments, the tank is first filled with water. Next, the seeding apparatus is lowered in the injection column. A sieve with a mesh aperture equal to or larger than the particle population upper diameter limit is then placed in the seeding apparatus (e.g. sieve 180 or sieve 200 for CER 160-180). For a given particle population, taking larger sieves enables to reach higher Φ_V more easily, but will of course reduce the number of experiments for a given quantity of particles. The sieve must be dry to prevent the formation of a bubble beneath the sieve, as, due to the small mesh appertures, water surface tension is strong enough to prevent air trapped under the sieve to go through the mesh. Particles are finally placed on the sieve. Experiments are then performed by turning the vibrating pot on and recording particles falling inside the main tank. To ensure that the fluid was as still as possible, a minimal waiting time of five minutes was followed between experiments, and a live feed from the cameras is observed to ensure no movement can be seen in the fluid.

Double phase experiments follow a similar protocol to particle only experiments, except that tracers are put in the water while filling the tank. Doing it during the filling process enables tracers to be well distributed in the tank and the injection column. First attempts where tracers were injected afterwards and mixed manually in the tank led to differences in tracer repartition between the main tank and the injection column. The fluid dragged by the particles from the injection column had less tracers than the fluid in the main tank, which lowered the accuracy of PIV.

Recording starts as soon as the vibrating pot is turned on. All experiments use the 'double frame' mode classically used for PIV: two images, or frames, are taken with a given time step d_t in between them, synchronized with two Laser pulses, and these double frames are recorded with a given acquisition frequency F_a. Initially, experiments lasted for 90 s with $F_a = 15$ Hz, the maximal sampling frequency of the system. Due to technical limitations, experiments at that frequency could not last much longer and induced a long delay between experiments as the computer was storing the data. Additionally, particle tracking was not possible using $F_a = 15$ Hz in our system with the particles tested so far. However, d_t can be adjusted so that PTV can be performed between the two images of a double frame. A majority of the experiments were then done at $F_a = 2$ Hz, for durations of 180 s to 360 s.

Before doing PTV and PIV, an image of the minimal intensities observed is computed for each experiment. This minimal image is then subtracted from all other images in the experiment. This process is done to increase the signal to noise ratio, and typically reduces the background noise level from 50-60 in greyscale intensity to 0-10. Afterwards, the images are exported and PTV and Voronoï analysis are performed using Matlab scripts. PIV is done directly in the DaVis software using an adaptative algorithm, the resulting velocity fields being exported afterwards.

In the system of coordinates used here, the x axis is the horizontal direction (parallel to the Laser sheet), the y axis is perpendicular to the Laser sheet and the z axis is oriented upward, i.e., opposed to gravity. PTV gives the positions x_p and z_p of the particles in every images as well as their velocities v_x and v_z along the same axes. Due to the orientation of the z axis, settling particles will then have $v_z < 0$. The Voronoï analysis associate each particle with its local Voronoï cell area $\mathcal{A}_p(t)$ for every instant t. The velocities of the fluid u_x and u_z can be obtained on an eulerian grid that depends on the resolution used when computing the PIV and of the calibration of the experiment. In our case, the PIV were performed using PIV boxes of 16 by 16 pixels with a 50% overlap, which results in a space resolution of 0.58 mm to 0.60 mm.

2.3.2 Statistics and parameter estimation

Particle measurements

Post processing on the PTV results remain the same whether the results come from particle only or double measure experiments. After PTV, the next step is to appraise whether the experiments are suitable for further processing. This is done in two phases: identifying a time range where particles fall in a steady state regime for statistics computation, then getting rid of edge effects.

First, for each experiment, the histograms of the velocities for every instant are computed. These histograms are then brought together to form temporal histograms such as the ones presented in figure 2.5. The histogram binning is chosen to be consistent throughout each experiments, by taking 300 linear bins between the maximal and minimal velocity value observed over the experiment. The purpose of these figures is to identify velocity plateaus in the experiments. These plateaus are time intervals during which the observed settling velocity stays relatively the same. Statistics will only be calculated on these plateaus. However not all experiments produce such plateaus. For example, the seeding system produces jolts when being turned on and of which usually leads to higher numbers of particles at the beginning and the end of experiments (if the seeding system is turned off before the end of the experiment). For some experiment,

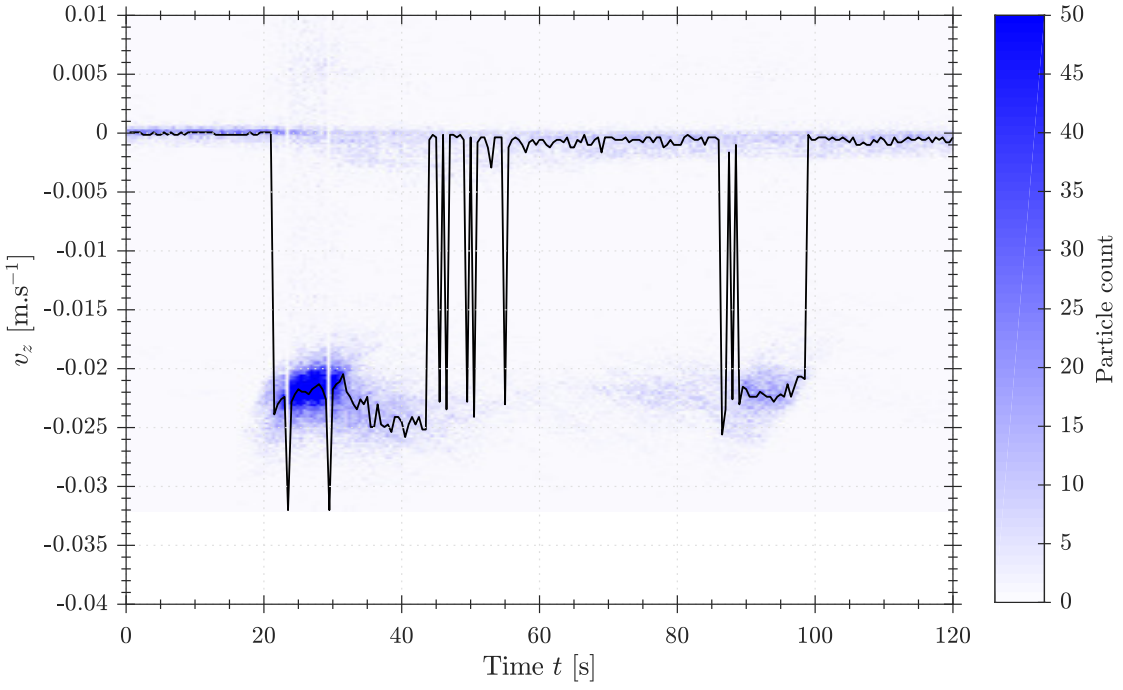

(A)

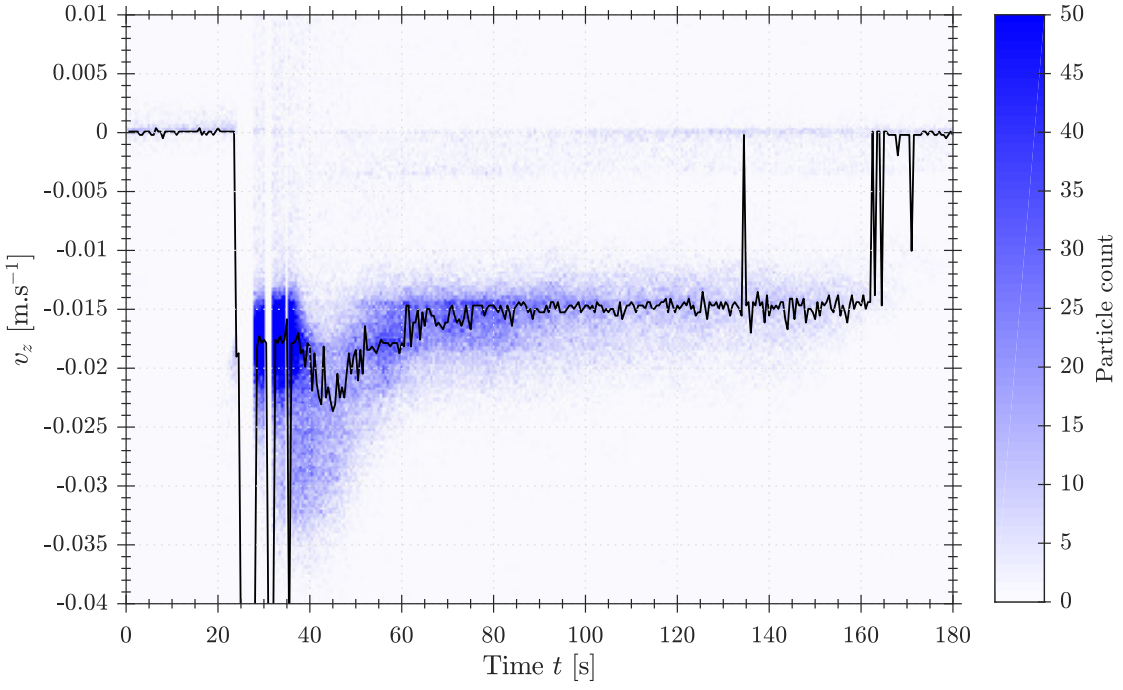

(B)

FIGURE 2.5: Examples of temporal histograms of the vertical particle velocity v_z. The mode of the histogram at each instant is represented in black. (A): CER 125-140 settling experiment. Here particles mainly fell at the activation of the seeding system and when it was shut down, resulting two clouds of particles falling during the experiment. (B): CER 106-125 settling experiment. More particles fall at the beginning of the experiment, to the point where PTV cannot be performed for some instants. This creates a transitory period before reaching a more stable plateau.

this results in two clouds of particles falling during the recording, one at the beginning and one the end, those two clouds sometimes being the only particles that fall during the experiment. The higher loading, especially at the beginning of the experiments, also means that performing PTV becomes more challenging and PTV might fail for the beginning of the experiments but succeed on the rest. Figure 2.5a shows a temporal histogram of an experiment where only two clouds of particle fell when turning the seeding system on and off. Figure 2.5b shows an experiment where a stable plateau suitable to compute statistics can be identified. An overview of the experiments performed and how many of them could be used for the study is presented in table 2.3.

Particle population	Particles only		Double phase	
	Performed	With plateau	Performed	With plateau
CER 180-200	42	26	14	10
CER 160-180	28	18	19	17
CER 140-160	16	11	0	0
CER 125-140	30	25	0	0
CER 106-125	19	11	6	0
CER 090-106	15	15	14	0
CER 075-090	17	15	13	0
TUN 075-090	13	6	1	0
TUN 063-075	24	21	17	16
Total	204	148	84	43

TABLE 2.3: Table summarising experiments done per particle population. The 'Performed' columns lists the number of experiments that were actually performed. 'With plateau' counts the number of experiments on which one or multiple plateaus could be defined for further statistics computation and analysis.

Once plateaus are identified, a region of interest (ROI) needs to be defined for each plateau. The field of view of the cameras is large enough that the settling particles typically form a column in the center of the field of view and leave the borders empty. This inhomogeneity creates a strong bias in the observed distribution of $\mathcal{V}$. Figure 2.6 shows an illustration of such bias from sets of randomly generated particles. A convention used here is that for a given framing, when computing Voronoï statistics, a cell will be discarded if any of its vertices is outside of the frame chosen, even if the particle that the cell belongs to is in the chosen frame. This typically means that particles that are close to the frame edges will be discarded. Figure 2.6a shows how this framing effect changes the distribution depending on whether particles on the border of the column are taken into account or not. The distributions of $\mathcal{V}$ obtained by keeping everything or only framing the column differ quite a bit, with the red frame staying close to the distribution of $\mathcal{V}$ for a set of randomly and uniformly placed particles. In figure 2.6b, the particle sets add some particles outside of the central region. This roughly mimics

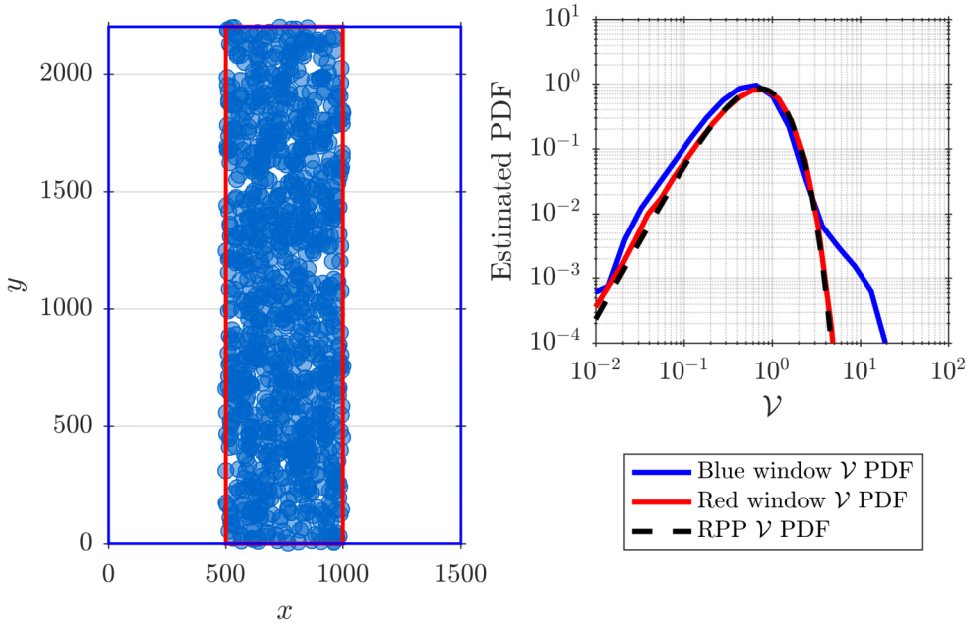

(A)

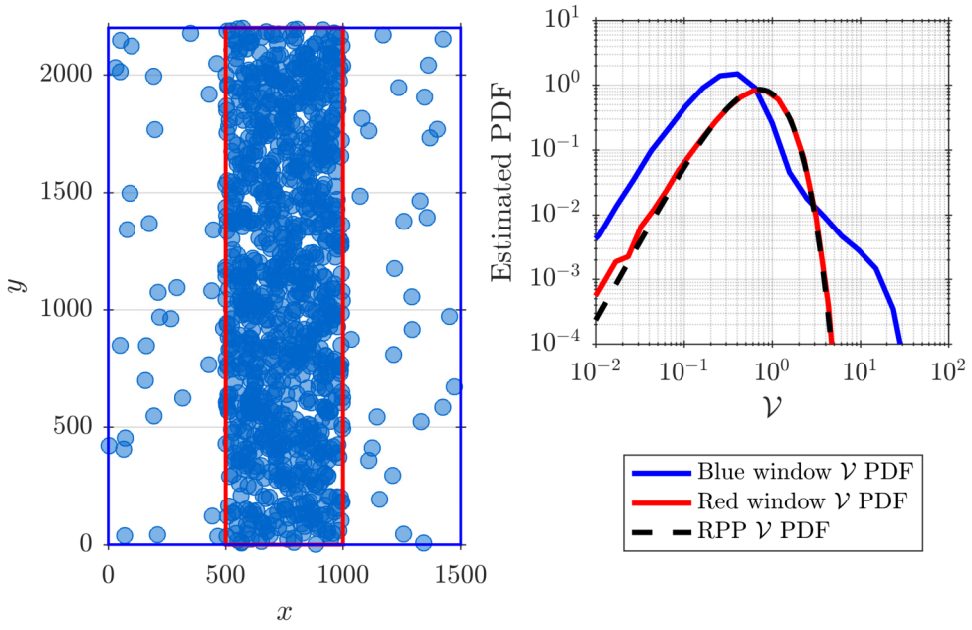

(B)

FIGURE 2.6: Illustration of the Voronoï framing bias. Random sets of particle positions were simulated with two cases, each type of set being generated 1000 times. Example of such sets are presented on the left side of the figures. (A) 1000 particles randomly uniformly generated in the center region (red frame). (B) 1000 particles randomly uniformly generated in the center region and an additional 100 over the whole region (blue frame). This roughly mimics the particle positions observed in the experiments. A Voronoï analysis was performed on these sets and estimated PDF of the normalised area of the Voronoï cells $\mathcal{V}$ was computed for the whole area (in blue) and only for the center region (in red). In both cases, a Voronoï cell is excluded if at least one of its vertex is outside the specified frame. The discontinuous black line is the expected PDF of $\mathcal{V}$ for particles that are randomly and uniformly placed (RPP stands for Random Poisson Process).

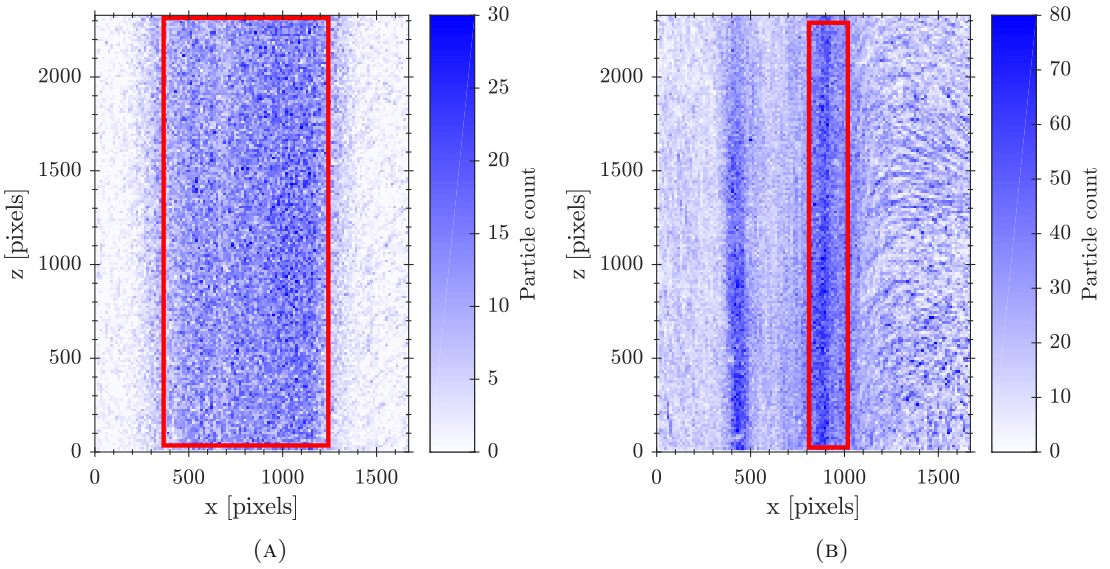

FIGURE 2.7: Examples of 2D particle presence histograms. The red rectangle corresponds to the ROI defined for these experiments. (A) Experiment of settling CER 160-180. Figure made over a plateau of 80 images, so over 40 s. In this case, particle settle in a large column at the center of the field of view. (B) Experiment of settling TUN 063-075. Figure made over a plateau of 522 images, so over 261 s. Here particle settle in two distinct columns. The column with more particles

particle detection on images from the experiments, where particles fall in a column in the center of the field of view with some detections on the sides mainly attributed to dusts floating in the experiment or other false detections. Here the results from the two framing differ even more as the effective positions of particles in the whole frame tend toward a bimodal distribution. This global inhomogeneity is a hindrance to try to observe potential preferential concentration effects which should occur only within the particle column.

To turn this bias, for each plateau previously identified, 2D particle presence histograms such as the one presented in figure 2.7 are used to define the ROI for the plateau (red frames in the figure). The 2D particle presence histograms are made by counting where particles are detected over time on the plateaus. The bin size in both direction is the same and corresponds to 1 mm. The ROI then defines which particle data will be accounted for when computing statistics. These figures also revealed that the distribution of particles varies quite a bit from one experiment to the next, often presenting strong inhomogeneities even when particles fall continuously. Figure 2.7b shows an example of this, where particles settle in two distinct columns. To investigate the origin of these inhomogeneities, some experiments were performed with a high speed camera pointed at the region right below the seeding system. This confirmed that these global inhomogeneities are already present when the particles leave the seeding system and remain consistent while the particles fall in the tank. They likely emerge from a combination

of factors including the quantity of particles and their distribution on the sieve or the activation sequence used for the vibrating pot, i.e., amplitude, frequency and function used. In case of inhomogeneities like these being observed, we choose to focus on the column of falling particles where more particles could be observed.

All further computations are then performed on results from the plateaus, taking only data from within the regions of interests.

A first and important parameter to compute is an estimation of the volumetric loading Φ_V. This is simply done by counting the number of particles in the ROI, dividing by the volume of the ROI and multiplying by the average volume of one particle. So for each instant t:

$$\Phi_V(t) = \frac{\pi}{6} N_p(t) \frac{\bar{d}^3}{A_{\mathrm{ROI}} th_L}, \tag{2.3}$$

where $N_p(t)$ is the number of particles in the ROI, A_{ROI} is the area of the ROI and $th_L = 2\,\mathrm{mm}$ is the thickness of the Laser sheet. This is then averaged over the plateau to have an estimation of the particle loading on the plateau. From there, the mass loading Φ_m can then also be computed as

$$\Phi_m = \frac{\Gamma \Phi_V}{1 + (\Gamma - 1)\Phi_V}. \tag{2.4}$$

For a global measure of the settling velocity over each plateau, an average of the vertical velocities of all particles is performed. However, in some instances a non negligible amount results coming from elements floating in the tank (e.g., dust) can be detected, with velocities close to zero. This effect can be seen in figure 2.5 where some 'particles' are always detected with a vertical velocity $v_z \approx 0\,\mathrm{m\,s^{-1}}$. To remove these false particles from the computation of the settling velocity, a simple velocity threshold V_{thresh} is used to count only the inertial particles:

$$V_z = \langle v_z \rangle, |v_z| > V_{\mathrm{thresh}}. \tag{2.5}$$

After observing the temporal histograms of all experiments, the value chosen for V_{thresh} was $0.005\,\mathrm{m\,s^{-1}}$.

For each instant t, the Voronoï cell area of each particles $\mathcal{A}_p(t)$ are normalised by the average area of the cells in the ROI:

$$\mathcal{V}_p(t) = \frac{\mathcal{A}_p(t)}{\langle \mathcal{A}_p(t) \rangle_t}, \tag{2.6}$$

and further statistics are then performed on this normalised quantity. Notably, for a given plateau, the standard deviation of this normalised area $\sigma_{\mathcal{V}}$ across every particles and over the duration of the plateau is computed.

Fluid and double-measurements

From the PIV measurements, the horizontal and vertical components of the fluid flow are obtained. These will respectively be called $u_x(x_i, z_i, t)$ and $u_z(x_i, z_i, t)$, where x_i and z_i are the coordinates corresponding to the centers of the PIV windows, and t is the considered instant. For a given plateau, the averages over time and space have been computed and are noted

$$U_x = \langle u_x \rangle \qquad \text{and} \qquad U_z = \langle u_z \rangle. \tag{2.7}$$

The standard deviations from these averages over space and time were also computed as std(u_x) and std(u_z).

To normalise these quantities, a characteristic velocity of the system has to be used. We decided to use the gravitational velocity used in the definition of the Archimedes number $v_g = \sqrt{(\Gamma - 1)gd}$, cited in section 1.1. This choice was made owing to the fact that this velocity does not presume of any drag model and because no specific fluid velocity is expected.

The slip velocities were also computed. The size the PIV measurement windows is already large compared to the size of the particles (16 pixels for the windows compared to a diameter of 4-5 pixels for the particles). Due to this, the PIV results already perform an averaging of the flow at scales that are larger than the particles. For this reason, the slip velocity will be computed simply by taking the fluid velocity on the PIV measurement grid that is closest to each particle. For the vertical velocity, this will be noted as $v_z - u_z$.

Chapter 3

Double measurement method

This chapter is an article currently in the process of submission to Experiments in Fluids. A list of the contributions of each author is presented here.

List of author contributions

David De Souza: data gathering, method conceptualisation, validation tests on the method, writing - original draft (excluding introduction and annex), editing. **Till Zürner:** data gathering, method conceptualisation, software implementation of the method, writing - annex, reviews. **Romain Monchaux:** original idea, data gathering, method conceptualisation, writing - introduction, reviews, supervision.

3.1 Introduction

Particle laden flows are ubiquitous in natural and industrial systems, and have received much attention in the last decades. When particle inertia is different from that of the fluid, the particle dynamics deviate from that of tracers which exactly follow fluid elements, and are usually used in fluid metrology to gain access to the fluid velocity field. Inertial particle trajectories sample the flow non-uniformly [Maxey and Corrsin, 1980] leading to preferential concentration, some regions of the flow being more visited than others due to their local properties (high/low strain or vorticity, vanishing acceleration...). When the particle loading is high enough, preferential concentration can lead to the formation of denser regions where particles accumulate as originally found by Brown and Roshko [1974]. This so called clustering can also be a consequence of the path history of particles and can thus occur in any region of the flow, regardless of its local properties [Gustavsson and Mehlig, 2011]. The high intermittency in the

concentration field due to clustering and/or preferential concentration can be an issue in many applications (e.g. for pollutant, plankton dispersion, mixing or fuel combustion in engines), but it may also have dramatic impacts on other relevant issues of particle laden flows: collisions, settling velocity alteration and carrier phase modulation. The collision probability depends on both the local particle concentration field and on the local velocity gradients [Falkovich et al., 2002]. The settling velocity is altered as soon as the carrier flow is turbulent [Maxey and Corrsin, 1980] but also when the local particle concentration is dense enough [Aliseda et al., 2002, Huck et al., 2018, Monchaux and Dejoan, 2017a]. Both cases depend non-trivially on many physical parameters (e.g. volume loading, phase density ratios, turbulence level or particle size). How the back reaction by the particles on the continuous phase modifies the carrier flow is just as complex and sensitive to the same parameters [Eaton, 2009, Elghobashi and Truesdell, 1993].

As direct on-site measurements of these processes (e.g. in clouds, marine snow, ash clouds or combustion chambers) are rarely possible, model experiments and numerical simulations are traditionally used to investigate the very rich physics of these flows. Due to the complexity of solving the flow in the vicinity of large numbers of finite sized particles, this kind of direct approach is still limited [Homann and Bec, 2010, Lucci et al., 2010]. Usually, the Navier-Stokes equations are solved for the fluid and model equations are used for the particles. Unfortunately, the available analytical model equations for the dynamics of inertial particles are obtained under the limiting assumptions of point particles and very large density ratio [Gatignol, 1983, Maxey and Riley, 1983] and involve many terms that are most of the time neglected in numerical studies. In addition, to reduce the computation time required to explore the wide parameter space described above, most numerical studies do not consider the back reaction particles exert on the fluid. Providing empirical models that allow for this back reaction to be numerically implemented without solving the whole velocity field in the neighbourhood of each particle is thus an essential challenge for the coming years.

To address this challenge, as well as providing model free data to understand the complex and intricate roles of the large number of parameters controlling particle laden flows, experiments have to provide detailed measurements in both phases, at the same time and location. Such measurements provide us with the slip velocity between the two phases, fluid-particle correlations or at least fluid statistics at the particle positions. All these quantities are key ingredients to understand the mechanisms at work in preferential concentration, clustering, settling velocity and collision alteration, and carrier phase modulation. Even though the development of such simultaneous measurements in both phases has started two decades ago [Towers et al., 1999], it is still far from being routinely used in laboratories and no commercial solution is available yet.

Fluid flow measurements are now available in any number of dimensions. Three dimensional (3D) Eulerian velocity fields are accessible through particle image velocimetry (PIV), that can even be time-resolved under certain conditions. Using particle tracking velocimetry (PTV), Lagrangian particle trajectories can also be measured at sufficiently high time resolutions to allow acceleration statistics to be computed [Ouellette et al., 2008]. The main drawback of the 3D measurements is its usually very limited volume. Probing wider regions of flows from both PIV and PTV is still the private preserve of two dimensional (2D) systems. Pointwise (0D) systems are also often employed in multiphase flow studies, particularly in wind tunnels to collect one dimensional (1D) data sets under Taylor hypothesis assumptions. These systems can be intrusive (hot wires, optical probes) or not (laser Doppler anemometer, phase Doppler particle analysis), some of them being able to discriminate between phases, see for example Muste et al. [1998]. However, it has been recently shown that the acquired 1D data may suffer from very strong biases that are difficult to overcome [Mora et al., 2018]. In the following we will focus on 2D systems.

Most 2D systems can be equally used to perform measurements on fluid tracers or on inertial particles. Indeed, as they are usually designed to see and/or follow tracers that are smaller than inertial particles, it is thus quite simple to use these same systems to image and/or track inertial particles that are often more visible on the acquired images than the tracers. The difficulty in measuring both phases thus mainly relies on the simultaneity, as these systems are usually not made to perform PIV on the fluid and PTV on the inertial particles at the same time. Several groups have designed such coupled measurement systems (see next two paragraphs) but, as mentioned above, it still remains a challenging issue. As both independent measurements are well developed, the key issue for simultaneously probing both phase is to manage the segregation between tracers and inertial particles. Depending on the carrier fluid, usually air or water, the tracer characteristics can be quite different. In water they are typically almost neutrally buoyant spherical particles whose diameters can range between 5 to 30 µm. In air, 1 to 2 µm oil droplets are traditionally used, but are increasingly replaced by 300 µm inflated neutrally buoyant soap bubbles. Regarding inertial particles, the range of particle size used by the different authors varies on orders of magnitude according to the wide range of corresponding applications. Larger particles are usually sand or beads whose diameters can be as large as a few millimetres while the smallest can be even smaller than tracers. While PIV tracers are designed to diffuse as much light as possible, inertial particles in general cannot be tailored to this purpose and come as they are. Depending on their size and material, they may scatter very little light.

Most successes in simultaneous fluid/particle measurements have been obtained when a large scale separation exists between particles and tracers. In this case, a classical 2D

PIV/PTV system is sufficient and particles and tracers are acquired on the same image by a single camera. Multiple authors designed different post-processing algorithms to achieve the segregation: simple discrimination by spot size has been used since the early two phase measurements by Chen and Fan [1992] or Hassan et al. [1992], but more sophisticated algorithms taking into account, for example, the relative brightness of tracers and particles [Khalitov and Longmire, 2002, Petersen et al., 2019], or filtering the tracers as a high frequency noise [Kiger and Pan, 2000] have been proposed. In many cases, the material and size differences between tracers and particles are obviously used in the separation algorithms.

In the absence of scale separation, a relevant idea is to use fluorescent dye [Elhimer et al., 2017, Poelma et al., 2007, Towers et al., 1999]. Under laser illumination, dyed tracers will emit light at a shifted wavelength while particles will only diffuse the incoming light as is. This seems to provide an easy way to perform the segregation. Single camera acquisitions can still be relevant if a colour camera is used. With green 532 nm laser and rhodamine coated tracers (a classical set-up), the green channel will ideally only see the particles while the red channel would only see the tracers. See Towers et al. [1999] for a more sophisticated application where both phases are dyed differently and a triple pulse laser is used to discriminate them. Unfortunately, the low resolution of colour cameras, the interpolation schemes used to compensate for the colour filtered array of pixels and the high level of induced pixel locking incite to avoid colour cameras. The obvious alternative is to use two cameras equipped with colour filters and aiming at the same field of view. The main issue then becomes the difficulty in matching the acquired fields of view. This can be achieved by using beam splitters, or by positioning both cameras very close to each other, aiming at almost the same field of view, and using a stereoscopic PIV calibration procedure to match the fields of view (the latter being our proposition). The use of a beam splitter avoids sophisticated calibration procedures since both cameras actually aim at the same field of view, but it implies a somewhat complex mounting and more importantly the loss of half the light budget, which may be an issue when particles do not diffuse much light. This was nonetheless successfully implemented by Elhimer et al. [2017]. In their study, a "cross-talk" between the two cameras remained. In fact, the inertial particles used were much larger than the tracers (more than 1 mm in diameter) and, due to their size, faint images of the inertial particles could be seen on the tracer images, as the fluorescent light emitted by the tracers was also scattered by the particles. This was solved with an additional post processing to separate particles from tracers thanks to their difference in intensity. The unusual use of a stereoscopic PIV system is made more appropriate and accurate nowadays with the recent development of so-called self-calibration algorithms that allow to almost perfectly match both fields of views. For more details on this calibration procedure see Wieneke

[2005]. In any case (colour or greyscale cameras, beam splitters or not), experimentalists are left with two sets of images. On the "red" one, only dyed tracers are visible, the flow field is thus easily accessible. However, on the "green" one, it might be more complicated. Indeed, the efficiency of the absorption and emission of the incoming wavelength by the dyed tracers is not 100%. As a result, tracers also directly scatter a portion of the laser light and are thus visible on the "green" images alongside the particles. Poelma et al. [2007] also refer to this as "cross-talk" between images. In their study, they manage to get rid of this cross-talk because, due to scale and brightness separation, the tracers' grey level is within background noise on the "green" images. When particles and tracers have similar sizes and when the particle material does not scatter much light, a way to remove tracers from these images has to be found.

In this article, we propose a method to achieve simultaneous velocity measurements of particles and tracers when no scale or brightness separation is present, by masking the tracers on images with inertial particles. The method developed here is generic and can be applied with most standard stereoscopic PIV systems. Section 3.2 of this article describes this method and outlines its potential pitfalls. To ensure that the method works and to examine its limitations, various tests are performed on experimental data sets. These testing procedures and their results are presented in section 3.3. Finally, section 3.4 gives recommendations on the method application and showcases some results from real-life experiments before concluding in section 3.5. The general application of PIV is not within the scope of this article and we refer to Raffel et al. [2018] for a comprehensive guide.

3.2 Tracer masking method

3.2.1 Method description

An overview of the method can be found in figure 3.1. The method starts from two synchronised image sources: one camera recording both particles and tracers, and one camera that only sees tracers. In the following these are denoted as particle camera and tracer camera, respectively. Both cameras record greyscale images, giving the light intensities $I_\mathrm{P}(x, y)$ for the particle camera and $I_\mathrm{T}(x, y)$ for the tracer camera.

The fluid velocity field can be calculated directly from I_T using PIV. To perform PTV on I_P, inertial particles have to be distinguished from tracers. This is achieved by creating a tracer mask from I_T that effectively removes the tracers from I_P. The inertial particles can then be tracked on the resulting filtered images. The characteristics on how to

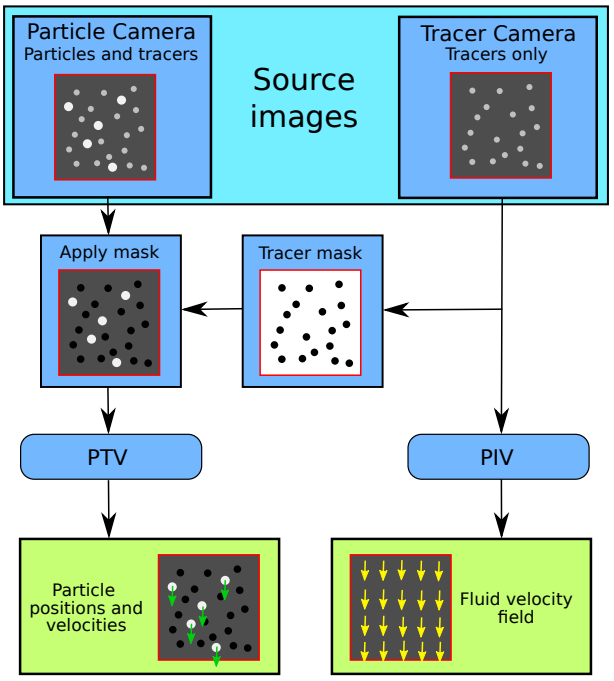

FIGURE 3.1: Flowchart of the method for simultaneous particle tracking and fluid velocity measurements by tracer masking. The illustration frames display particle and tracers with exaggerated color and size difference for easier distinction only (see figure 3.13 for real-life examples).

perform a good PIV or PTV will not be discussed in this article, and the parameters involved in these techniques will only be mentioned when relevant to the topic.

A flowchart of the mask creation process can be found in figure 3.2. The goal is to set the intensities of all pixels belonging to a tracer in I_P to zero. The first step is to detect

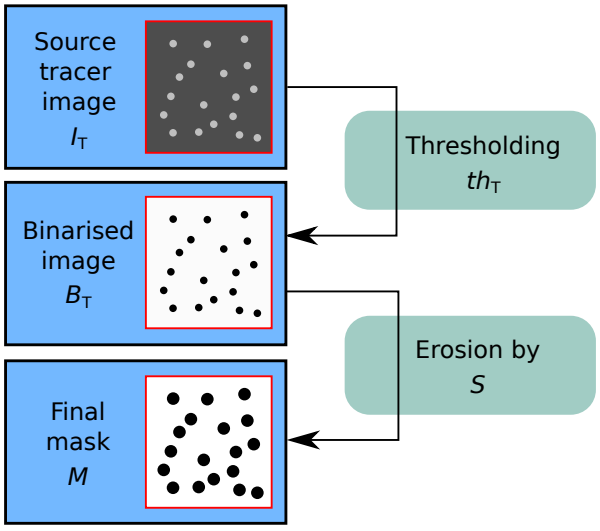

FIGURE 3.2: Flowchart of the mask creation process. On B_T and M, areas in white represent pixel values of one and areas in black are pixel values of zero.

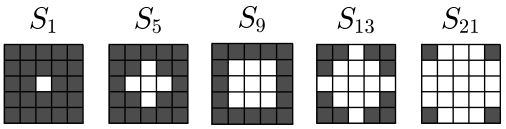

FIGURE 3.3: Examples of structuring elements. Each sub-square represents a pixel, zeros are in black, ones are in white. For the purpose of this article, they are designated by the number of pixels having a value of one.

the tracers on I_T. This is done by turning I_T into a binary image B_T that sets all pixels that belongs to a tracer in I_T with zero:

$$B_\mathrm{T}(x,y) = \begin{cases} 1, & I_\mathrm{T}(x,y) < th_\mathrm{T} \\ 0, & I_\mathrm{T}(x,y) \geq th_\mathrm{T} \end{cases}, \tag{3.1}$$

where th_T is the intensity threshold defining whether a pixel belongs to a tracer or not. Using the colour code of figure 3.2, the area of interest here becomes a white background, while the black spots of the tracers are the regions that will be discarded. However, depending on the configuration of the image sources, small discrepancies in shape, intensity, or even positions of the tracers might exist between I_P and I_T. These are further discussed in section 3.2.2. To accommodate for these discrepancies, an erosion is performed on B_T using a structuring element S. This morphological operation expands the black areas (zeros) in B_T, i.e., the areas marked as tracers are increased. Examples of structuring elements can be found in figure 3.3. The size of S corresponds to how much the tracer areas are enlarged by, e.g., S_1 does not change the image while S_{13} expands the black areas by a margin of about 2 pixel. More details on morphological operations can be found in Haralick et al. [1987]. The result of the erosion of B_T by S is the final tracer mask M.

The tracers are then removed from I_P. This removal is done by applying M to I_P with a simple pixel-wise multiplication:

$$I_\mathrm{M}(x,y) = I_\mathrm{P}(x,y)M(x,y), \tag{3.2}$$

where I_M is the final particle image, without tracers. The positions and velocities of the inertial particles can finally be obtained by performing PTV on I_M.

3.2.2 Error assessment

Generally speaking, errors resulting from the application of this method can have two main origins. The discrepancies in the tracers properties between the two source images I_P and I_T constitute one of these origins. For example, if a system with two cameras is

used, a tracer can be projected onto each camera with different intensities, shapes and positions. A difference in intensity is not an issue for the method presented here, as the choice of th_{T} is informed by the intensities of tracers in I_{T} only, and tracers masked in I_{T} will be removed from I_{P} regardless of their intensities. However, differences in shape or position may lead to M not properly covering the tracers in I_{P}. In this instance, tracers detected in I_{T} may remain in I_{M} and particles might have been erroneously deleted by the mask. The second category of error sources is an inadequate choice of the method parameters th_{T} and S. Going to extreme cases, if th_{T} is low enough to catch the background noise level of I_{T}, pixels that are not from tracers will be set to zero in B_{T}, resulting in an unnecessary loss of data in I_{M}. Conversely, putting th_{T} too high will leave all tracers in the image. For S, if it is too small, the erosion will not make up for the discrepancies between I_{P} and I_{T}. But picking one that is too big will end up with a mask that deletes portions of the image that could have been kept.

From these two origins, three main errors can occur: tracers can remain in I_{M}, particles can be completely removed when applying the mask or they can be partially removed. These errors will be referred to as false particle error, erased particle error and altered particle error respectively. First, the false particle error adds false positives, which can skew the tracking results as tracers are mistaken as particles. Second, the erased particle error leads to false negatives, resulting in a loss of data. Finally, the altered particle error will change the particle's detected position, as altering the shape of a particle will change where the center of the particle is detected. In addition to their effects on the trajectories computed by PTV, these errors will influence the apparent concentration field, which is crucial to understanding the mechanics of dispersed two-phase flow systems.

3.3 Method Validation

To evaluate the response of the method to the errors outlined in section 3.2.2, two testing procedures have been devised. These procedures involve images from experiments as the basis of the tests. This section first describes the experimental set-up used to obtain these images before covering each testing procedure and their results.

3.3.1 Experimental set-up

An illustration of the experimental set-up can be found in figure 3.4. The main part is a tank of dimension $350\times480\times350\,\mathrm{mm}^3$. A column, of square cross-section with side length 130 mm and height 410 mm, sits on top of it. This structure is filled with water. On top

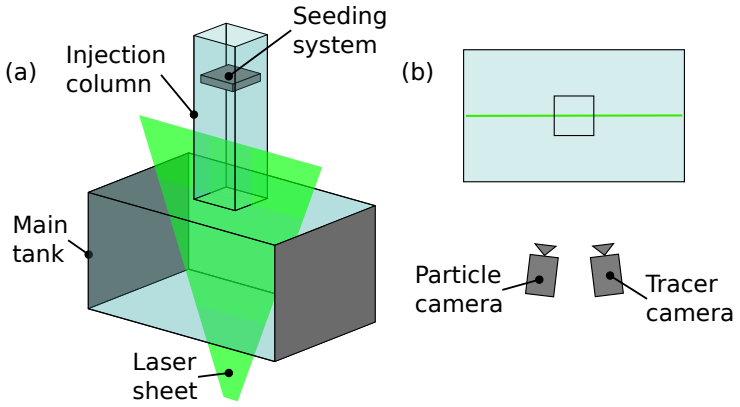

FIGURE 3.4: Experimental set-up: (a) overview without the cameras, (b) top view.

of the column, a vibrating sieve serves as the seeding system for the apparatus. Particle injection is controlled by pouring particles onto the sieve and turning the vibration on.

Observations are done in the main tank. Images are recorded with a LaVision stereo PIV acquisition system of two VC-Imager SX 4M cameras synchronised with a vertical pulsed laser sheet of wavelength 532 nm produced by an Nd:YAG Dual Power 135-15 laser from Dantec Dynamics. The two cameras are mounted with $f = 50$ mm focal length lenses through Scheimpflug rings to compensate the lens plane tilt. The tracers used are 20 µm melamine resin based polymer particles coated with fluorescent rhodamine B sold by Dantec Dynamics. Accordingly, the tracer camera is equipped with an optical filter that lets the fluoresced light emitted by the rhodamine of wavelength above 570 nm pass through and blocks the laser wavelength. Its aperture is set to $f/1.8$ while that of the particle camera is set to $f/8$ in order to achieve similar intensities on I_{P} and I_{T}. Both cameras are calibrated on the same area of the laser sheet using a dotted plate and the self-calibration method previously mentioned.

The two cameras record two images or frames each, in quick succession, and the time in between the two frames can range from 10 to 30000 µs. These double frames from both cameras are recorded with an acquisition frequency of up to 15 Hz. After applying the tracer removal method, the instantaneous particle positions and velocities, and the fluid velocity field are obtained. However, the maximal sampling frequency of the system does not allow to track particles between double frames, i.e., long-term particle trajectories are not accessible in the present experiments. In other terms, PTV is performed on each double frame recorded as if it were independent of the previous and following double frames in the experiment. However, the method presented in this article does not depend

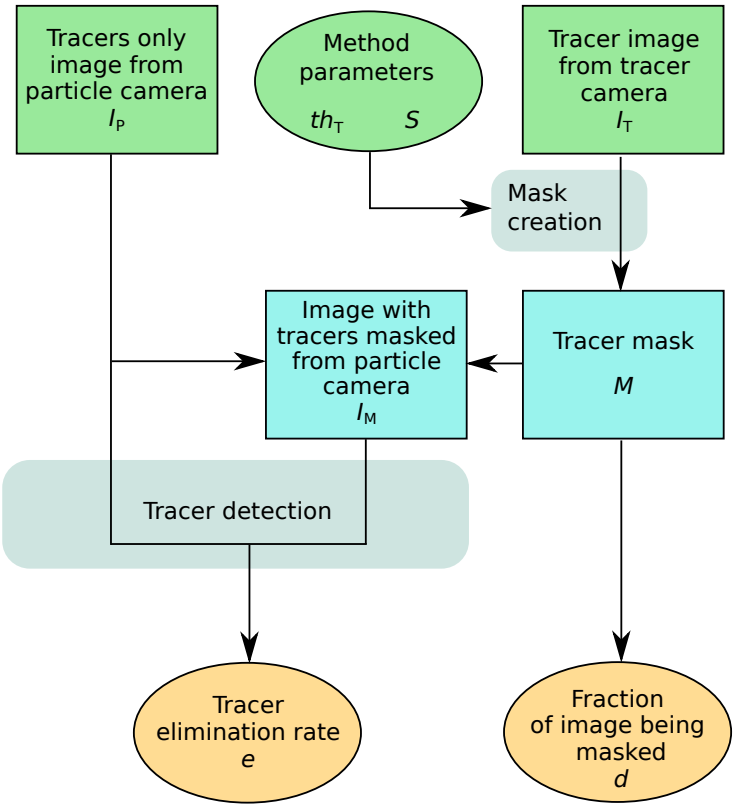

FIGURE 3.5: Flowchart of the testing procedure on errors coming from discrepancies between I_P and I_T.

on the acquisition frequency and and can be applied to systems with higher sampling rates.

The images have a resolution of 1700 by 2375 pixel, with each pixel having an intensity ranging from 0 to 4095. Overall the acquisition system has a scaling factor of 13.7 pixel/mm which then corresponds to an area of 124 by 173 mm of the laser sheet used for observation. For each experiment, an image of the minimal intensities observed on the experimental run is computed and then subtracted from all images to increase the signal to noise ratio. After this operation, the images typically have a background noise below 10 in pixel intensity. The apparent diameter in pixels of the particles obviously depend on their size and the material they are made of but the smallest tested up to now span 4 to 5 pixel. The rhodamine coated tracers have an apparent diameter of 2 to 3 pixel.

TABLE 3.1: Overview of the parameters tested in the tracer removal test procedure (section 3.3.2), and of the characteristics of the images tested. For an illustration of the structuring elements' shapes, see figure 3.3. All the images used are from different experimental runs.

Parameter	**Values, range or number**	**Unit**
th_T	{5; 10; 20; 35; 50; 70}	greyscale intensity
Structuring elements' shapes	S_1, S_5, S_9, S_{13}, S_{21}	-
Number of images	77	-
Tracer diameter	2 to 3	pixel

3.3.2 Tracer removal test procedure

The first testing procedure is a tracer elimination check done mainly to test the method's response to the errors from the discrepancies between I_P and I_T, and how its parameters can be tuned to yield reliable results. A flowchart of this procedure can be found in figure 3.5. It is designed to ensure that the method removes all tracers while deleting as little of the image as possible. The test images I_P and I_T used here contain only tracers. That way when applying the tracer masking method, the resulting I_M should ideally be empty. Then, by applying PTV on I_M, any particle detected will in fact be a tracer that was not removed. The images I_P and I_T used were taken from experiments conducted on the device described in section 3.3.1. For a given pair of tracer-only images I_P and I_T, the only other inputs for the testing procedure are th_T and S, the parameters of the tracer removal method. A particle detection (i.e., the first step of PTV) is performed on the tracer-only particle image I_P and on the masked image I_M, resulting in a number of detected particles for each of these images. These numbers will respectively be called N_P and N_M. A tracer elimination rate e is then computed as $e = (N_P - N_M)/N_P$. In addition, the fraction d of the image deleted by the method can also be computed from the mask itself, as the number of pixels at zero in the mask over the total number of pixels. An overview of the inputs used for this testing procedure can be found in table 3.1.

Both e and d take values between zero and one. Ideally, e should be as close to one as possible (at $e = 1$ all tracers have been eliminated). At the same time, d should be minimised ($d \to 0$) to avoid excessive image alteration. The idealistic case of $d = 0$ cannot be achieved as it is only possible if no tracers are detected in I_T. Thus, the minimisation process of d has to be understood as choosing the method parameters that give the smallest d without significantly affecting $e \sim 1$.

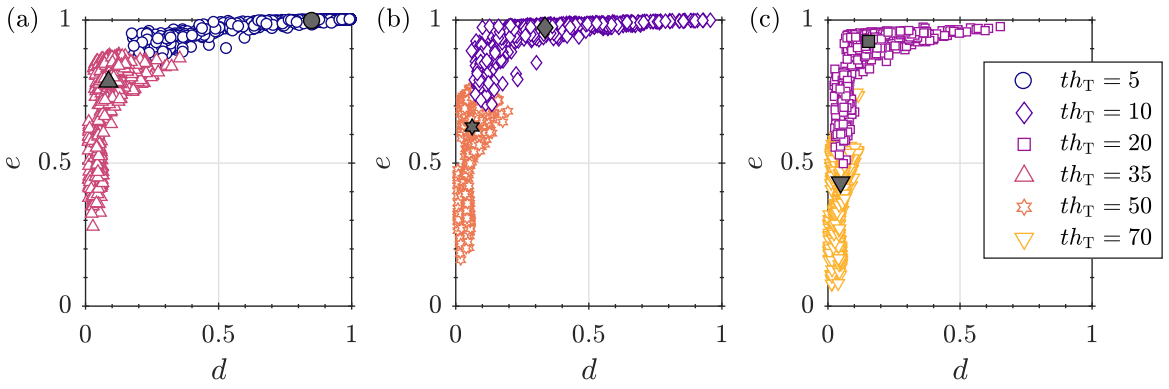

FIGURE 3.6: Scatter plots of e against d, distinguished by values of th_T, for all S. These are spread in three separate plots for clarity, to avoid overlapping too many points. The median of each dataset is plotted as filled marker of the corresponding shape. Among the tested thresholds, $th_T = 20$ (squares) results most consistently in low d and high e.

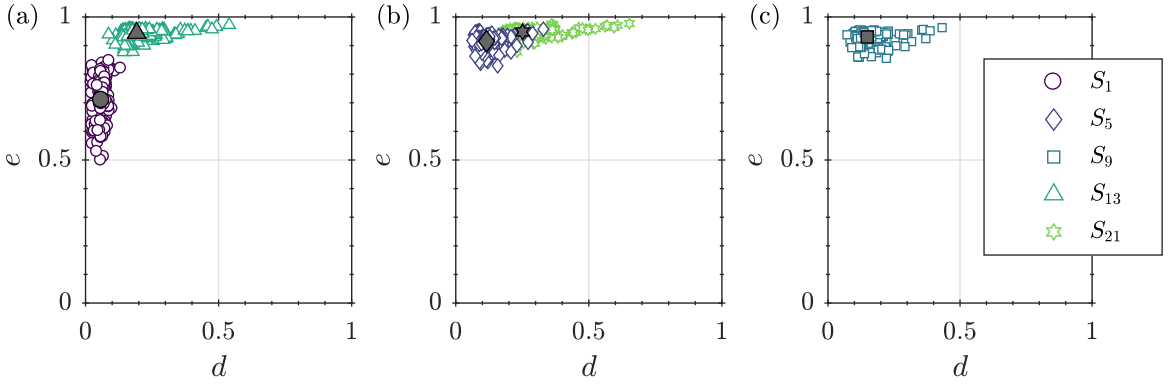

FIGURE 3.7: Scatter plots of e against d, for $th_T = 20$ (square markers in figure 3.6c), distinguished by S. These are spread in three separate plots for clarity, to avoid overlapping too many points. The median of each dataset is plotted as filled marker of the corresponding shape. S_5 and S_9 lead to the best results in terms of e and d.

In figure 3.6, e is plotted against d, separated and coloured by values of th_T used in the tests. th_T is shown to have a clear impact on both e and d. The observed response can be explained as follows. Taking a value for th_T that is too low will identify the background noise of the image as tracers and extend the area removed by the mask to regions where there are in fact no tracers. This results in all tracers being removed but at the cost of deleting a large portion of the image, thus in high e and high d. On the other hand, setting a value for th_T that is too high will miss a lot of the tracers in I_T, causing them to remain after M has been applied, as described in section 3.2.2. As fewer tracers are marked for removal, a smaller fraction of the image will be deleted, which leads to both low e and low d. th_T needs to be selected carefully in order to get appropriate results, i.e., high e and low d. To this end, the median values of each dataset are shown in figure 3.6 as filled marker. In the tests presented here, the median value of $th_T = 20$

(square) achieves the best results in terms of consistently high tracer elimination e and low image deletion d. Note that this value is specific to the images tested here, and depends on the image acquisition system and potential post-processing applied to the image (such as background image subtraction or noise filtering). The method may still perform well for $th_{\mathrm{T}} < 20$, as, even if more of the image is deleted, more tracers will be removed without necessarily diminishing the number of inertial particles that can still be found by the method.

The impact of S can then be seen in figure 3.7, where e is plotted against d for a fixed $th_{\mathrm{T}} = 20$, separated and coloured by S. S_1, which corresponds to no erosion being performed at all, does not remove all tracers but keeps d at low values. By increasing the size of the structuring element to S_5 and S_9, e gets higher without deleting too much of the image yet. Beyond that for S_{13} and S_{21}, e remains in the same range but d increases. Overall, this is because larger S widen the areas detected as tracers more than smaller S when applying the erosion. This results in smaller S deleting less of I_{P} than larger ones but also being less likely to catch discrepancies between the position or shape of a tracer in I_{T} and in I_{P}. The images I_{P} and I_{T} used in these tests match one another with a precision of ± 1 pixel. This explains the better results obtained for S_5 and S_9, as seen in their median values (filled markers): these two elements extend the areas detected as tracers in B_{T} over that ± 1 pixel range for the final mask M.

This procedure confirms the trends mentioned in section 3.2.2 on the influence of the choice of th_{T} and S. These parameters need to be chosen carefully and tuned according to the images and the system used.

3.3.3 Particle matching test procedure

The second procedure is designed to test errors resulting specifically from an inadequate choice of the parameters th_{T} and S. A flowchart of this procedure can be found in figure 3.8. The objective here is to ensure that tracked particles can faithfully be recovered after the method has been applied, while still removing the tracers. To separate this test from errors coming from discrepancies between I_{P} and I_{T}, it is performed on images with a perfect superposition between the two cameras. To achieve this, an image where only particles are visible I_{P0} is taken and combined with a tracer image I_{T} into a synthetic image I_{C}. I_{C} is made by taking the maximal intensity between I_{P0} and I_{T} for each pixel: $I_{\mathrm{C}}(x, y) = \max(I_{\mathrm{P0}}(x, y), I_{\mathrm{T}}(x, y))$. By doing so, I_{C} has both particles and tracers, tracers perfectly match between I_{T} and I_{C}, and I_{P0} gives access to what I_{C} looks like without tracers. The goal is then to recreate I_{P0} by applying the tracer removal method to I_{C} and see if tracking results are the same when PTV is performed on

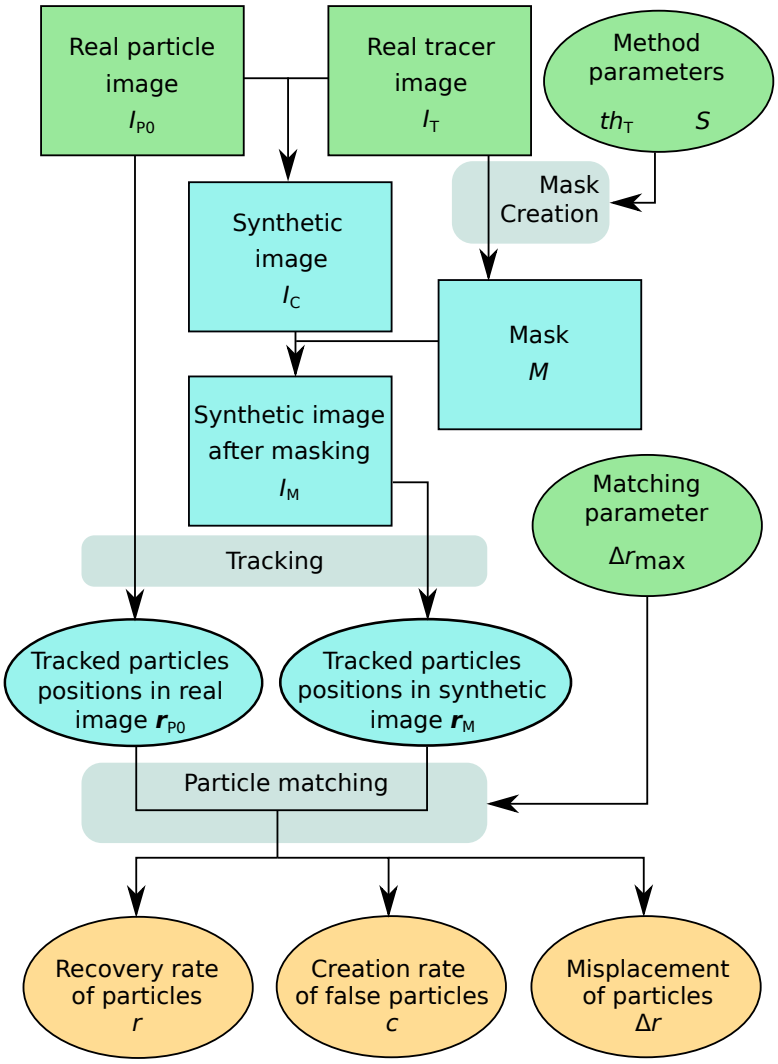

FIGURE 3.8: Flowchart of the testing procedure on inadequate parameter choice.

I_{P0} and on I_C after removing the artificially added tracers. The tracer removal method is used on I_C which results in a masked image I_M, and PTV is then performed on I_{P0} and I_M. This gives access to the positions $\boldsymbol{r}_{P0}$ and $\boldsymbol{r}_M$ of particles successfully tracked in these images (i.e. particles for which a track has been found, providing both particle position and velocity). A particle matching is then performed, by comparing the particle positions $\boldsymbol{r}_{P0}$ and $\boldsymbol{r}_M$, pairing particles in I_{P0} and I_C with a maximal distance between them of Δr_{max}. Overall, the inputs of this testing procedure for a given pair of images I_{P0} and I_T are the method parameters th_T and S, and the matching parameter Δr_{max}. After the particle matching is done, particles can be divided into three categories: particles only found in I_{P0}, particles only found in I_M, and particles that have been successfully matched between I_{P0} and I_M. The number of particles in each of these categories are denoted as N_{P0}, N_M and N_b, respectively. The rate of particle recovery

TABLE 3.2: Overview of the parameters tested in the particle matching test procedure. For an illustration of the structuring elements' shapes, see figure 3.3. The images I_T and I_{P0} come from various experiments using tungsten carbide particles of diameter comprised between 63 µm and 75 µm and ceramic particles with diameters between 180 µm and 200 µm.

Parameter	**Values, range or number**	**Unit**
th_T	{10; 20; 35; 50; 70}	greyscale intensity
Δr_{max}	0.2 to 5	pixel
Structuring elements' shapes	S_1, S_5, S_9, S_{13}, S_{21}	-
Number of I_T	6	-
Number of I_{P0}	75	-
Tracer diameter	2 to 3	pixel
Particle diameter	4 to 7	pixel

r is then computed as: $r = N_b/(N_b + N_{P0})$. r then varies between zero and one, with zero meaning that all initially tracked particles in I_{P0} were lost while going through the test, and one meaning that all of them where recovered. In the same manner, the tracers left in I_M appear as newly created particles, and correspond to the number N_M. Accordingly, the creation of false particles is computed by the creation rate c, given by: $c = N_M/(N_b + N_{P0})$. Additionally, the particle matching gives the misplacement Δr for each particle detected in both I_{P0} and I_M, that is to say $\Delta r = ||\boldsymbol{r}_M - \boldsymbol{r}_{P0}||$.

An overview of the input parameters used in this procedure is presented in table 3.2. Although tests have been performed for all the structuring elements S presented in figure 3.3, the best results where systematically obtained with S_1, which is equivalent to not applying any erosion when making the mask. This is in line with the fact that, in this testing procedure, the images have a perfect superimposition, and the areas of the mask that will remove the tracers do not need to be extended to cover any discrepancies between the particle image and the tracer image. All data presented in this section hereafter is obtained using S_1 as the structuring element.

As Δr_{max} fixes the maximum misplacement error that can be measured in these tests, its value may influence the results obtained by the procedure. To avoid the introduction of biases, the mean recovery and creation rates $\langle r \rangle$ and $\langle c \rangle$ (averaged over all test cases for a given th_T) are plotted against Δr_{max} in figure 3.9. For Δr_{max} between 1 and 2 pixel, $\langle r \rangle$ and $\langle c \rangle$ saturate on plateaus whose values depend mainly on the chosen threshold th_T. This fixes an upper limit to the misplacement of particles by the method to 2 pixel, as increasing Δr_{max} beyond this value does not change the results. This limit can be high depending on the resolution of the system, but will be discussed further at a later

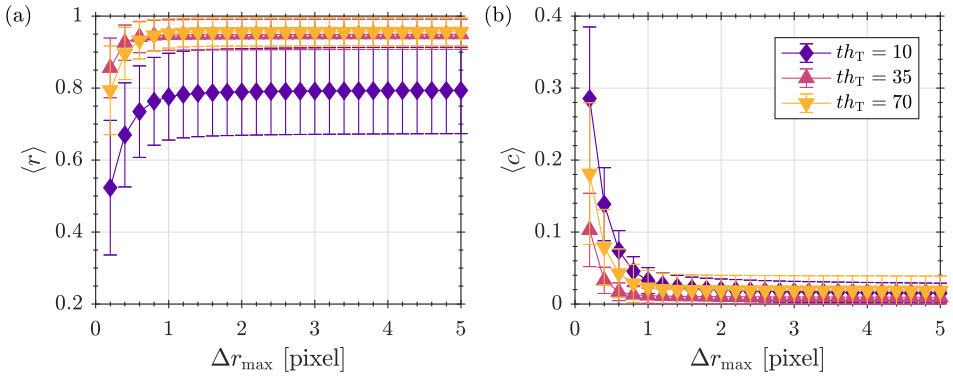

FIGURE 3.9: Averages of r and c, as functions of $\Delta r_{\max}$, coloured and separated by th_{T}. Only some values of th_{T} are presented here to show the general trends. The error bars are of one standard deviation above and below the mean value. Both $\langle r \rangle$ and $\langle c \rangle$ stabilise at plateau values reached generally between 1 to 2 pixel for $\Delta r_{\max}$. These plateau values are mainly influenced by th_{T}.

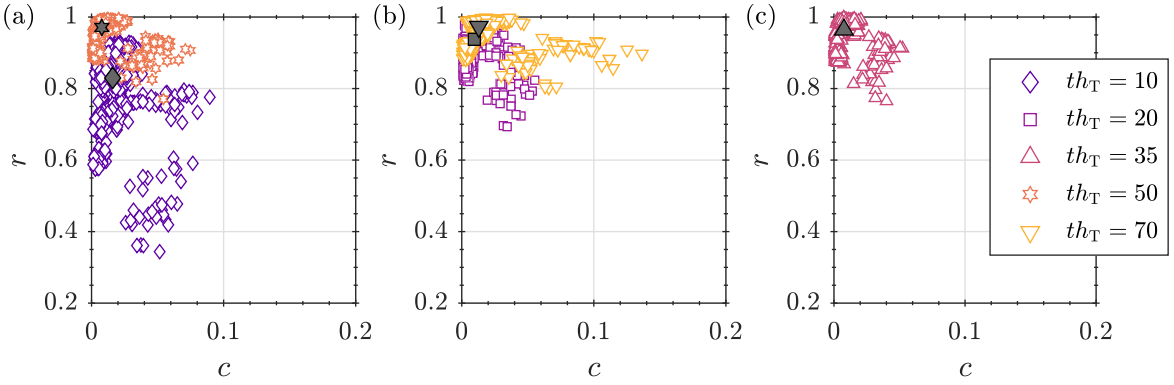

FIGURE 3.10: Scatter plots of r against c for $\Delta r_{\max} = 2$ pixel, distinguished by values of th_{T}. These are spread in three separate plots for clarity, to avoid overlapping too many points. The median of each dataset is plotted as filled marker of the corresponding shape. The threshold that reaches high r and low c most consistently is $th_{\mathrm{T}} = 35$.

point in this section. To further study r and c, $\Delta r_{\max} = 2$ pixel will be used in the following analysis.

For this procedure, a good parameter choice should result in high r and low c. Here, again, th_{T} is shown to be crucial. Scatter plots of r against c distinguished by th_{T} are presented in figure 3.10. Over these plots, as th_{T} increases, r increases overall to values getting closer to one. The values of c start to spread over a 0 to 0.1 range for $th_{\mathrm{T}} = 10$. That range first decreases as th_{T} increases, reaching a minimal spread and best median value (filled marker) for $th_{\mathrm{T}} = 35$. The data for $th_{\mathrm{T}} = 50$ has a similar median but for it and higher values of th_{T}, the range of c values increases again. This confirms yet again that picking too low or too high of a value for th_{T} leads to poorer performance for the method, as low values generate masks that delete a larger area than necessary and high

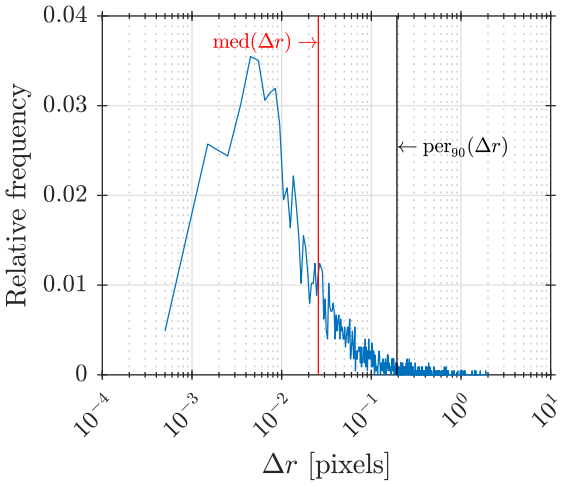

FIGURE 3.11: Typical example of an histogram of Δr. The counts are normalised by the total number of samples (i.e., the number of particles successfully matched N_b) to obtain a relative frequency. This histogram comes from a test case with $th_\mathrm{T} = 35$, S_1 and $\Delta r_\mathrm{max} = 2\,\mathrm{pixel}$. The median and 90$^\mathrm{th}$ percentile of the distribution are marked by vertical lines.

values fail to remove some tracers. Over the tests presented here, $th_\mathrm{T} = 35$ seems to achieves the best results.

By design of the test method, for each set of given inputs, $\Delta r \leq \Delta r_\mathrm{max}$. To obtain a finer measure of the misplacement error of the method, the distribution of Δr has to be studied. The misplacements Δr of all detected particles have been compiled in histograms such as the one presented in figure 3.11. All histograms obtained are heavily skewed toward low values for Δr, typically less than 0.1 pixel. To have a better estimation of the misplacement error, the median and 90$^\mathrm{th}$ percentile of the distribution of Δr have been computed for every test case. Figure 3.12 shows these quantities averaged for a given th_T and Δr_max. Both the median and 90$^\mathrm{th}$ percentile of Δr have a minimal value reached for $th_\mathrm{T} = 35$ in the tested cases, confirming the previous result that this is the best value for th_T over the tests made in this procedure. In this case, half of the particles are on average misplaced by less than 0.05 pixel by the method, and 90% by no more than 0.21 pixel. These results are also stable for $\Delta r_\mathrm{max} > 2\,\mathrm{pixel}$, while values lower than that lead to slightly lower values of the median and 90$^\mathrm{th}$ percentile.

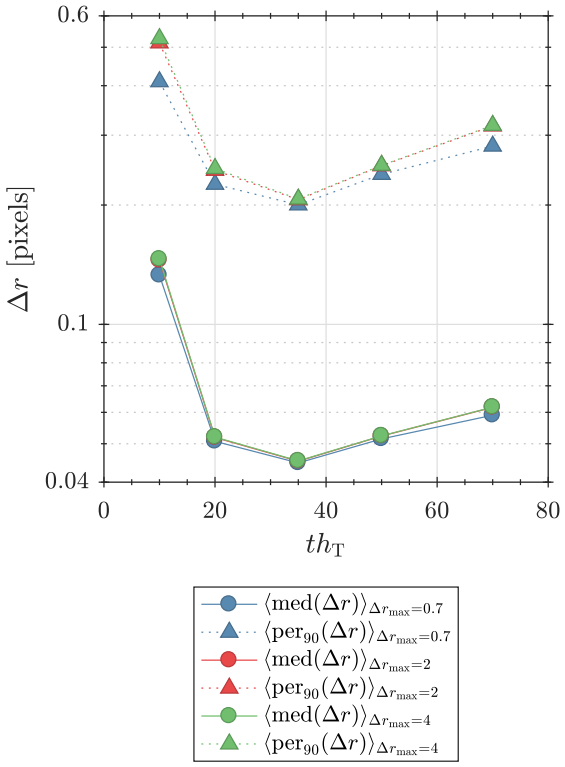

FIGURE 3.12: Mean of the median and 90^{th} percentile of Δr over the tested cases against th_{T}, and separated by Δr_{max}. Three Δr_{max} have been chosen here to showcase the trends observed. The results for $\Delta r_{\mathrm{max}} = 2$ (in red) and $\Delta r_{\mathrm{max}} = 4$ (in green) are almost superimposed.

3.4 Method results

3.4.1 Recommendations

The starting step to use the method is to acquire the images. First, the tracer images should be suitable to perform PIV. This means having a sufficient tracer seeding in regard to the image resolution and the PIV interrogation windows, typically 3 to 5 tracer per interrogation window. However, as the method removes the part of the image that corresponds to tracers, it is recommended to aim at the lowest possible density in tracers that still allows accurate PIV to be performed (i.e., within the range of seeding densities appropriate for PIV, the lower end is preferable). This will of course be dependent on the acquisition system and on the PIV algorithm used. Secondly, the particle images should also enable PTV to be performed. Overall, this also translates to having a good resolution of the particles on the images to accurately find particle positions. Once again this will depend on the systems and algorithms used. For the acquisition system presented in section 3.3.1, having an apparent diameter of 5 pixel was enough to detect particle centers with sub-pixel precision. Finally, and perhaps most importantly, both

image sources must be synchronised and calibrated in a way that allows them to be superimposed. The superposition should be as accurate as possible, to allow for a smaller structuring element S to be used which reduces the risk of erroneously deleting particles with the tracer mask (see section 3.3.2).

To use the method itself, the choice of th_{T} is the most important parameter to decide on, as evidenced by the tests of sections 3.3.2 and 3.3.3. th_{T} should be chosen so that it is above the background noise of I_{T}, to avoid the removal of portions of the image where no tracers are present. Other than that, we recommend to set th_{T} as low as possible to ensure all tracers are removed. Typically, for the images obtained from the experimental set-up described in section 3.3.1, $th_{\mathrm{T}} = 10$, when paired with S_9 results in almost all tracers being eliminated from I_{P} while still being able to track at the very least 80% of inertial particles.

The choice of the structuring element S is then also important. This will depend on how well I_{P} and I_{T} can be superimposed. In the case of a perfect superposition, (i.e., all tracers in both images perfectly overlap) no erosion (S_1) is required for the method to work correctly. Otherwise, a measure of how much disparity remains between I_{P} and I_{T} is needed to choose the structuring element. A simple approach is to perform a cross-correlation on sub-areas of images I_{P} and I_{T} when only tracers are visible. This is in fact similar to how the correction from the self-calibration method is computed [Wieneke, 2005], and akin to how PIV is performed in general. The resulting disparity map gives the remaining local misplacement between I_{P} and I_{T}. Then the larger the disparities are, the larger S will have to be. For example, for differences of ± 1 pixel, S_9 would be a good choice, as this element will cover all disparities in that range. For discrepancies of ± 2 pixel or more over large parts of the images, a re-calibration of the PIV system should be considered.

Finally, we would like to point out that the structuring elements tested here where chosen to have no preferential orientation. This is because the present discrepancies between I_{P} and I_{T} did not show any preferred axis. However, depending on the experimental set-up, anisotropic distortions can occur and remain consistent through time. Examples of such distortions include curved windows between the cameras and the laser sheet (e.g. cylindrical tanks) or astigmatism which can be induced by some optical filters. When such time-consistent distortions occur, S can also be deformed and stretched along the direction of these distortions.

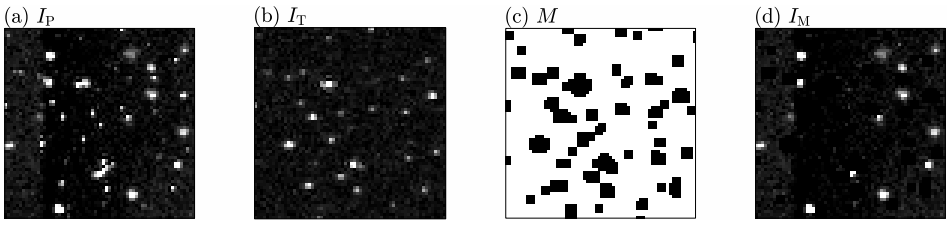

FIGURE 3.13: Examples of the source images and the method results. (a) Particle camera image I_P. (b) Tracer camera image I_T. (c) Tracer mask M generated from I_T using $th_T = 10$ and S_9. (d) Masked particle image I_M. The images are 64 pixel × 64 pixel sub-sections of the full images and correspond to the experiment in figures 3.14 and 3.15 at time $t = 20\,\mathrm{s}$. The brightness values in (a), (b) and (d) are shown in greyscale from zero (black) to 64 (white).

3.4.2 Example results

This section showcases some results obtained with the tracer removal method. These come from an experiment where ceramic particles with diameters between 160 µm and 180 µm are settling in water. The fluid is initially quiescent and seeded with neutrally buoyant tracers coated with rhodamine. The experimental set-up and the tracers are as described in section 3.3.1.

An exemplary sub-section of the source images I_P and I_T with the corresponding tracer mask M and masked particle image I_M are shown in figure 3.13. Bright spots in I_T indicate tracers that are also visible at the same position in I_P. These are removed by applying M and the remaining bright spots in I_M are the inertial particles.

The recording starts as soon as the seeding system is turned on ($t = 0\,\mathrm{s}$). Figure 3.14 shows the evolution of the vertical velocity v_z of the detected particles over time. Histograms of v_z have been computed for each timestep and compiled into a colour plot. Additionally, the mode of the histogram is shown as a solid line. Negative values of v_z denote a downward motion of the particles. In the first instants, the particles have not reached the field of view of the cameras so any detected particles are false positives from tracers, which explains the histograms' modes lingering around $v_z \approx 0$. At $t = 12\,\mathrm{s}$ particles start passing in the camera field of view and can be detected. The first cloud of particles falls with a settling speed of $v_z \approx -0.32\,\mathrm{m/s}$. In their wake, subsequent particles are accelerated to velocities of $v_z \approx -0.42\,\mathrm{m/s}$ ($t \approx 40\,\mathrm{s}$). Finally, the particles reach a stationary behaviour ($t > 90\,\mathrm{s}$) while falling with a velocity of $v_z \approx -0.34\,\mathrm{m/s}$.

Figure 3.15 shows two examples of instantaneous particle velocities and fluid vertical velocity fields from the same experiment. They were taken at $t = 20\,\mathrm{s}$ for figure 3.15a and $t = 60\,\mathrm{s}$ for figure 3.15b to have similar average particle velocities. Figure 3.15a shows the particles settling in a column with a downward fluid flow. The same can be

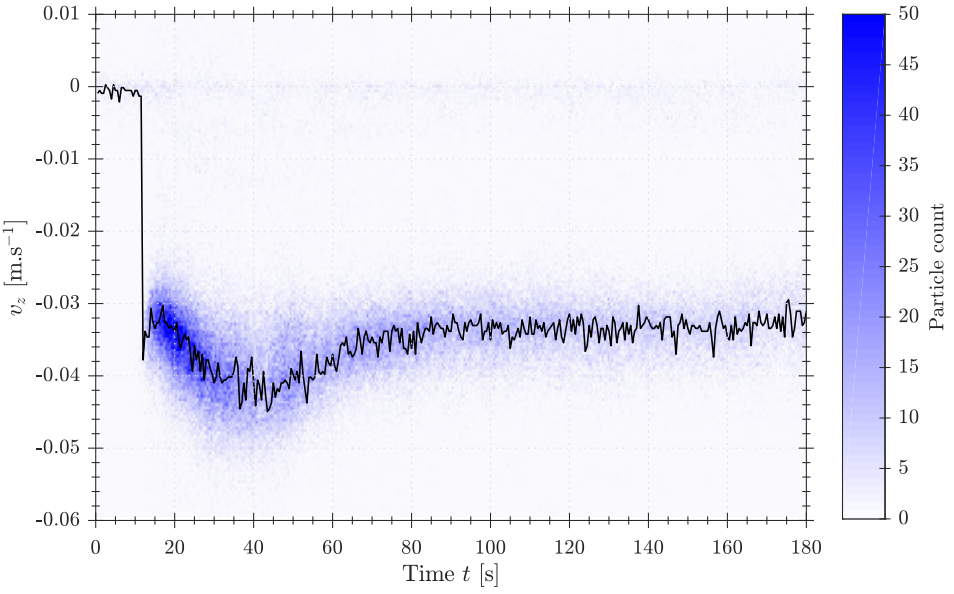

FIGURE 3.14: Temporal histogram of the vertical velocity v_z for ceramic particles of diameters between 160 µm and 180 µm settling in quiescent water. The black line corresponds to the mode of the histogram at each instant in time. The vertical axis z of the experiment is oriented upward, so falling particles have negative velocities.

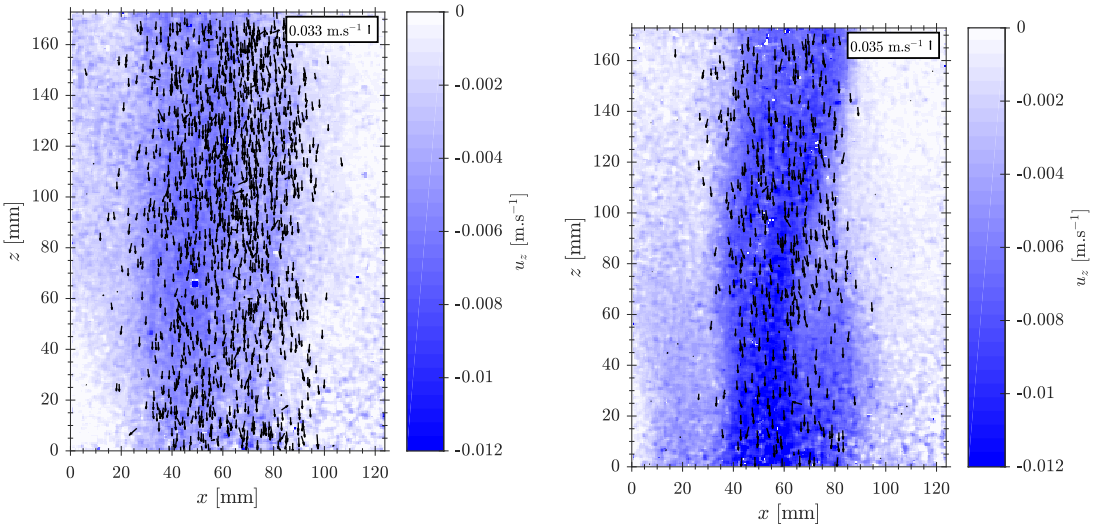

(A) (B)

FIGURE 3.15: Instantaneous particle velocities (arrows) and fluid vertical velocity fields u_z (colour-plot) at (a) $t = 20\,\mathrm{s}$ and (b) $t = 60\,\mathrm{s}$, of the same experiment shown in figure 3.14. Arrows of the average velocity magnitude of the particles are in the top-right corners of each plot for scale.

said for figure 3.15b, however the number of particles is smaller and the downward fluid flow is more intense and localised in the column of settling particles. The evolution of the fluid velocity flow suggest the development of large scale flows in the experimental set-up.

The tracer removal method could then give access to data from both phases simultaneously and showcase the importance of having access to both velocity fields to better study dispersed two-phase flow systems. Statistics on the evolution of other relevant quantities such as the local slip velocity (i.e., the difference between the particle velocity and the fluid velocity at the position of the particle) will be investigated in future studies.

3.5 Conclusion

A method to distinguish particles from tracers in the study of dispersed two-phase flow has been developed. This method relies on the use of both optical filtering paired with adequately dyed tracers (rhodamine coated tracers in this case) and post-processing operations to segregate inertial particles from tracers. This tracer removal method can function properly even when particles and tracers are undistinguishable in size or intensity through usual visualisation techniques. The method was tested to ensure its proper operation, and to assess its response to various input parameters. From these tests, suitable parameters for the method were found. Although these parameters are specific to the experimental set-up on which the method is used, general rules on how to properly choose them have been provided. This method works on a variety of particle material and size, opening the possibility to access large ranges of the parameter space experimentally.

Appendix: Exemplary implementation

This section outlines an example implementation of the tracer removal method in MATLAB R2016b. The particle image I_P and the tracer image I_T are stored in the variables `I_P` and `I_T`, respectively, as $(N_1 \times N_2)$-matrices of type `uint16`. The position of the tracers in I_T are detected by a threshold value th_T of, for example, 35.

```
>> th_T = 35;

>> B_T = I_T < th_T;
```

The variable `B_T` holds the binarised image B_T. For the erosion of B_T, the structure element S_5 is chosen.

```
>> S_5 = [0 1 0; 1 1 1; 0 1 0];
```

```
>> M = imerode(B_T, S_5);
```

The variable `M` is a $(N_1 \times N_2)$-matrix of type `logical` containing the tracer mask M. To calculate the masked particle image I_M, the mask is applied to I_P.

```
>> I_M = I_P .* cast(M, 'like', I_P);
```

The variable `I_M` is a $(N_1 \times N_2)$-matrix of type `uint16` and contains the image I_M with only particles remaining. It can now be further evaluated, for example, by applying a PTV algorithm.

Chapter 4

Results

In this chapter, the first two sections presents results from PTV measurements, without looking at the fluid flow. The presented results all come from data acquired on experimental plateaus defined in section 2.3.2. Results on settling velocities will be presented first, then results from the Voronoï analysis. Results from PIV are presented in a third section, first looking only at the fluid flow, before looking at the slip velocities.

4.1 Settling velocities

4.1.1 Global measurements

Many experiments where performed, which span a large number of parameter values. The majority of the experiments performed used ceramics particles (i.e. $\Gamma = 4$). As such, much data was gathered on that specific density ratio, and potential effects of other parameters like Ar and Φ_m can be assessed on these experiments. More experiments using particles made of different materials are required to truly disentangle the effects of all control parameters. This is achievable with the particle populations already available in our laboratory.

Figure 4.1 presents a scatter plot of the settling velocities V_z measured on each plateau as a function of the diameter of the particles. The average diameter $\bar{d}$ of the particle populations are used here. The model curves of the settling velocity of a single sphere using either a Stokes or a Schiller-Naumann drag model are also represented for each particle type (ceramics at $\Gamma = 4$ and tungsten carbide at $\Gamma = 15.63$). As an indication, each point is also coloured according to the mass loading Φ_m measured on the plateau. The points seem to overall follow the trend set by the Schiller-Naumann drag model more than the Stokes drag model.

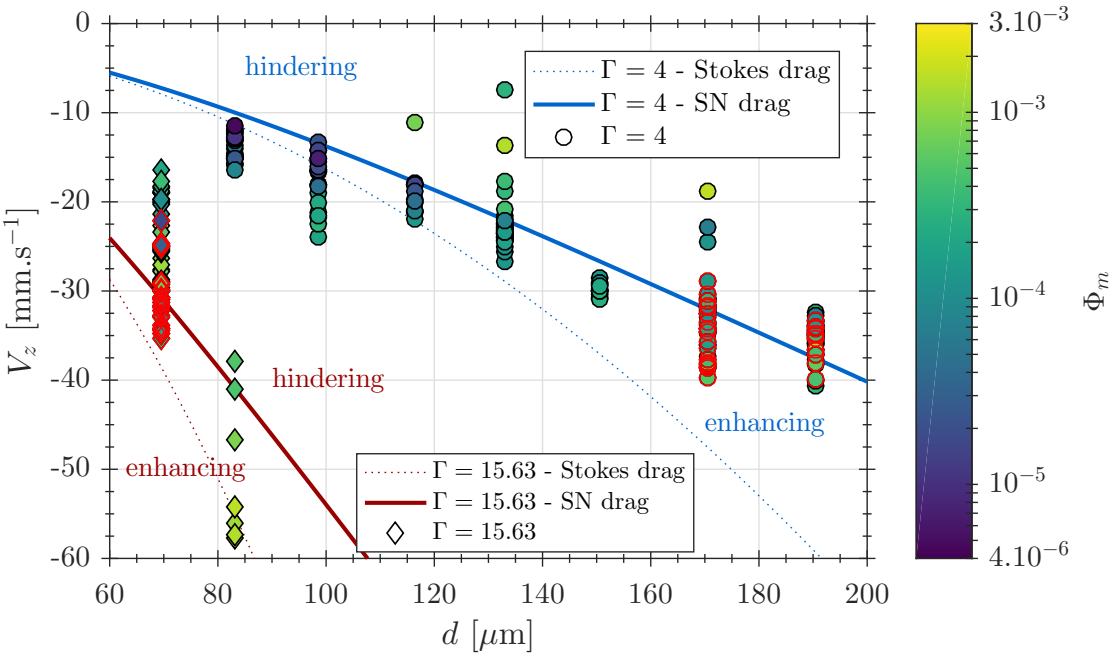

FIGURE 4.1: Scatter plot of V_z versus $\bar{d}$. Each point represents the results from one plateau. Marker shape distinguishes between particle material and colour stands for for Φ_m. Red borders are placed over the marker edges of points when simultaneous PIV/PTV was performed. The theoretical curves of the settling velocity of a single sphere expected with either a Stokes or Schiller-Naumann (SN) drag model are also represented (blue for $\Gamma = 4$, red for $\Gamma = 15.63$). Regions of settling velocity hindering or enhancing are placed with respect to the Schiller-Naumann model.

The data presented in figure 4.1 can also be viewed in a non dimensional form. V_z can essentially be turned in the particle based Reynolds number R_p, while both Γ and d can be condensed into the Archimedes number Ar. Figure 4.2 then represents the same data as figure 4.1 viewed in an (Ar, R_p) plane. As per equation 1.6, the theoretical curves then collapse into a single line for each model. The Ar numbers of each particle populations are computed using their density ratios Γ and average diameters $\bar{d}$. For the populations used up to now, all resulting Ar numbers are distinct, so one Ar number only corresponds to one population of particles. The points still follow the trend of the Schiller-Naumann model, more so here than in the previous figure, and, with two exceptions (TUN 063-075 or $Ar = 48$ and CER 180-200 or $Ar = 204$), most particle populations present enhanced settling velocities overall, with respect to the Schiller-Naumann reference. The values of the particle based Reynolds numbers R_p corresponding to every V_z measured range from 0.95 to 7.73. This falls in the validity domain of the Schiller-Naumann model. This explains why the overall trend followed by the points seems to align more with the Schiller-Naumann drag model, which will be used as our reference case from now on. The significant deviations observed from the model likely arise from either collective effects or from the fluid flow, as the model is valid only for a single particle settling in quiescent fluid.

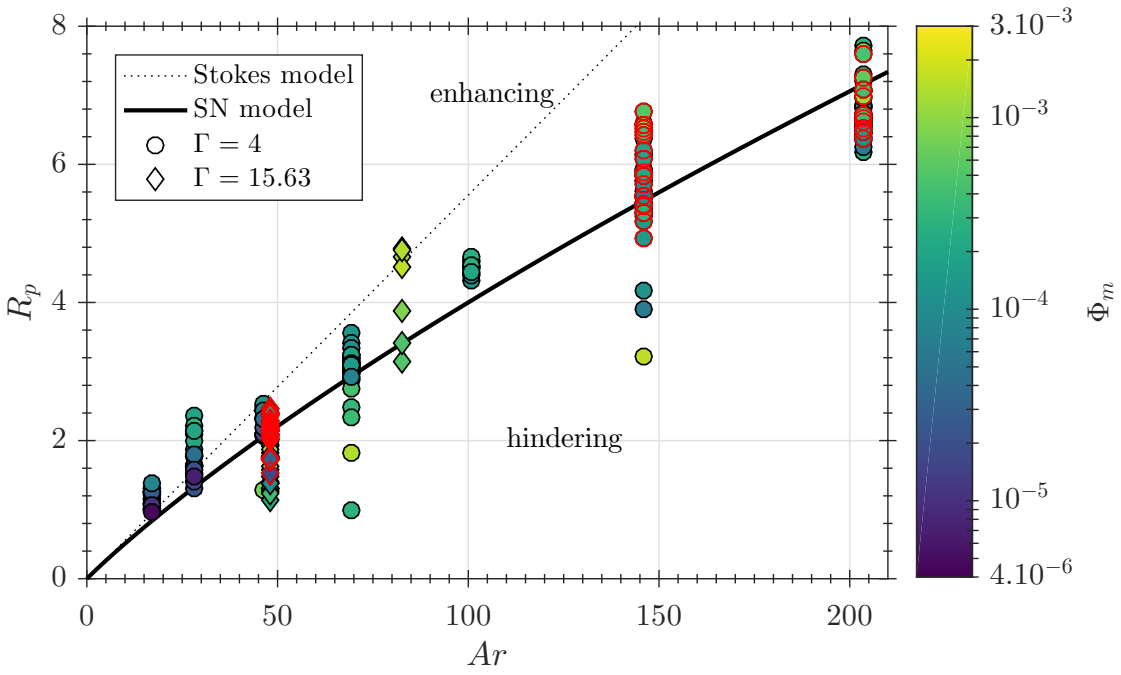

FIGURE 4.2: Scatter of the particle based Reynolds number R_p computed from the settling velocities V_z over each plateau as a function of the particle populations' Archimedes numbers Ar. Red borders are placed over the marker edges of points where simultaneous PIV/PTV was performed. Compared to figure 4.1, the curves for the theoretical models collapse as expected into one line for each model, and, as R_p is taken as positive by convention, the hindering and enhancing regions are also reversed with respect to figure 4.1.

It is important to note here that both in figure 4.1 and in figure 4.2, the experiments combining both PTV and PIV (red outlines on the markers in the figures) do not particularly differ from the results of experiments where no tracers were present. This further validates the double measurement method presented in chapter 3. As noted, a great variability in the results between experiments is also present. Part of this variability likely comes from the way experiments are performed and the experimental device rather than the dynamics of the system we want to study here. For example, as noted in section 2.2, the seeding apparatus itself is responsible for a portion of this variability. The repartition of particles in the seeding apparatus will change the shape of the particle column for each experiment, and sometimes a large portion of the particles may fall outside of the laser sheet. Although it is indicated by the colour of the markers in figures 4.1 and 4.2, Φ_m varies also a lot between experiments and certainly plays a major role in the observed variability.

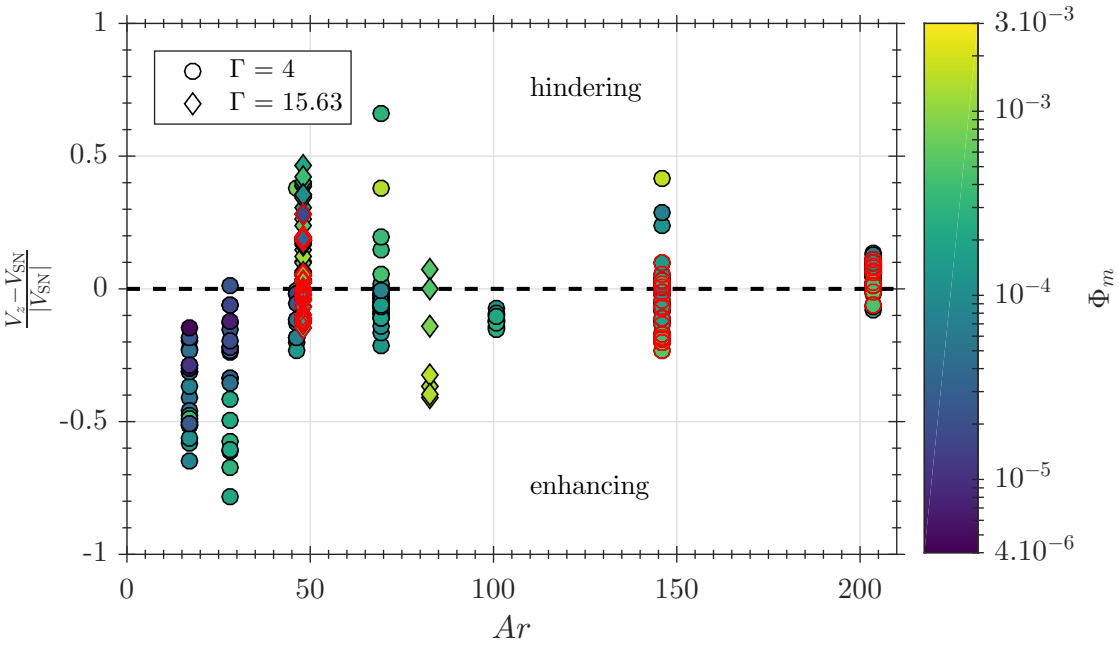

FIGURE 4.3: Velocity alteration with respect to the Schiller-Naumann reference vs Ar. Both V_z and V_{SN} are negative here for settling particles (upward z-axis). An enhancement (resp. hindering) of the settling velocity then corresponds to negative (resp. positive) values. Red borders are placed over the marker edges of points where simultaneous PIV/PTV was performed.

4.1.2 Settling alteration: influence of Ar and Φ_m

For each velocity plateau, the settling velocity alteration with respect to the Schiller-Naumann reference is then computed as $\frac{V_z - V_{SN}}{|V_{SN}|}$, where V_{SN} is the settling velocity computed using a Schiller-Naumann drag force with parameters matching the particle population of the considered experiment. Figure 4.3 shows a scatter plot of $\frac{V_z - V_{SN}}{|V_{SN}|}$ against Φ_m. All particle populations present mostly enhanced velocities, with the exceptions previously noted (TUN 063-075 or $Ar = 48$ and CER 180-200 or $Ar = 204$). Over all experiments, $\frac{V_z - V_{SN}}{|V_{SN}|}$ ranges from -0.78 to 0.66, which roughly corresponds to a 78% increase for one and a 66% decrease for the other in settling velocity. However, this large range includes inter-experiment variability which hide other dynamics, notably particle-fluid interactions, as the settling particles generate a flow and interact with it. This will be discussed in section 4.3

The effects of Φ_m in particular are difficult to assess from figure 4.3. An attempt at visualising potential trends with Φ_m is shown in figure 4.4, where the velocity alteration has been averaged over different Φ_m ranges and plotted against Ar. Those ranges where chosen so that the same number of experiments would be in each category over all experiments. Because Φ_m is an output of each experiment, it is difficult to control it precisely. Moreover, it is easier to achieve higher Φ_m values with larger and/or denser particles. To remove cases in figure 4.4a where not many experiments were performed,

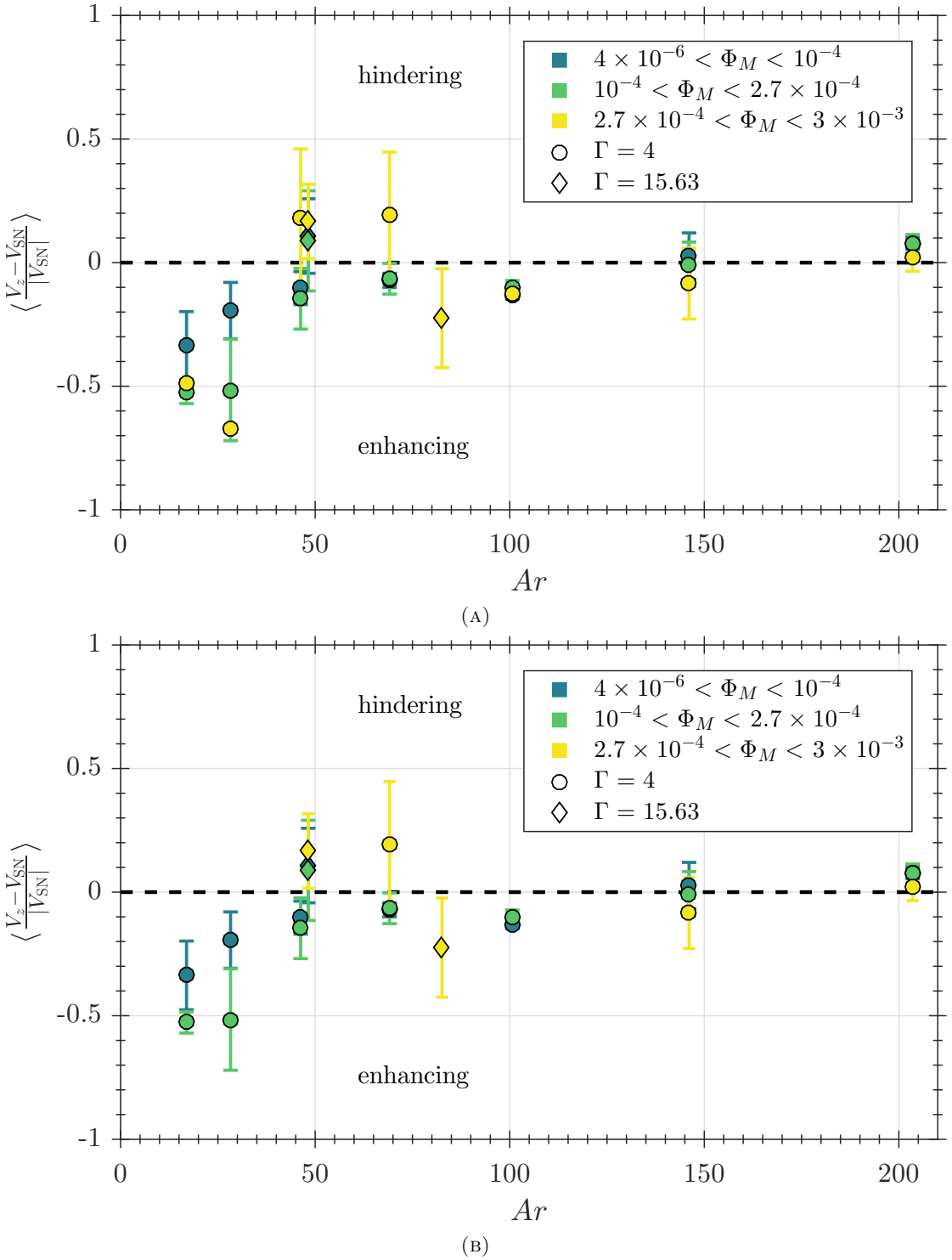

FIGURE 4.4: Mean of velocity alteration with respect to the Schiller-Naumann reference against the Ar number, grouped by ranges of Φ_m. These ranges where chosen so that the same number of experiments fall in every one of them. Subfigure (A) represents all data. Points that would represent only one or two experiments have been removed in subfigure (B). The error bars here represent one standard deviation above and below the mean, i.e. a total span of 2 standard deviations. Both V_z and V_{SN} are negative here for settling particles (upward z-axis). An enhancement (resp. hindering) of the settling velocity then corresponds to negative (resp. positive) values of the velocity alteration.

figure4.4b represents only points where at least three experiments where performed. This figure shows that deviation from the Schiller-Naumann model is more pronounced at lower Ar number values. For $Ar < 40$, results clearly point to an enhancement of the settling velocity, with increases of at least 10% and up to 70%. At $Ar > 110$, no significant deviation from the Schiller-Naumann model is observed, except maybe for a slight hindering for lower loadings for CER 180-200 ($Ar = 204$). The middle range is more difficult to interpret, notably due to a lack of data. Because the data is spread over many parameter values, a true statistical analysis would probably require more experiments to be performed to increase the number of data points, especially in missing categories (e.g. high mass loadings with really small particles). Obvious examples of that are: the TUN 075-090 population ($Ar = 83$, $\Gamma = 15.63$), where few experiments were performed (7 points only) and the results obtained all correspond to $\Phi_m > 2.7 \times 10^{-4}$, and CER 075-090, CER 090-106 and CER 140-160 (resp. $Ar = 17$ $Ar = 28$ and $Ar = 101$, for $\Gamma = 4$), where only one plateau falls in the higher loading range $\Phi_m > 2.7 \times 10^{-4}$ (not represented on figure 4.4).

The Ar number can be viewed as a loose measure of a particle's inertia, in the sense that higher inertia particles will correspond to higher Ar values and vice versa. In our case, looking at figure 4.3, this would mean that particle with higher inertia either are not affected as much by what causes the settling velocity modification as lower inertia particles, do not trigger the mechanisms responsible for settling enhancement, or both. For example, higher inertia particles would not be affected as much by the surrounding flow, and would then tend to stick to the reference case. Lower inertia particles on the other hand are more sensitive to changes in the fluid velocity field and could for example be more likely to be pulled by the background flow, or to stick in another particle's wake (e.g. as observed in Huisman et al. [2016] although for particles with a lower Γ but a larger diameter). This will be further discussed when looking at the results obtained for double measurements experiments in section 4.3.

Figure 4.5 shows the velocity alterations of all experiments plotted against Φ_m, in separate subfigures for each Ar number. First, for lower Ar numbers (top row of subfigures), higher Φ_m do seem to result in higher enhancements of the settling velocity than lower mass loadings. Increases of more than 50% are even observed for $Ar = 17$ and $Ar = 28$. The $Ar = 83$ figure also seems to show such a strong trend, but it remains difficult to say due to the lack of data points. But for $Ar > 40$ in general, this effect of Φ_m is either not as strong or simply absent, even though most experiments present enhancements of 5 to 10%. For the tungsten particles of case $Ar = 48$, Φ_m seemingly has no impact on the alteration of the settling velocity, and many cases here present hindered velocities. Despite having experiments with loadings one order of magnitude higher than $Ar = 28$,

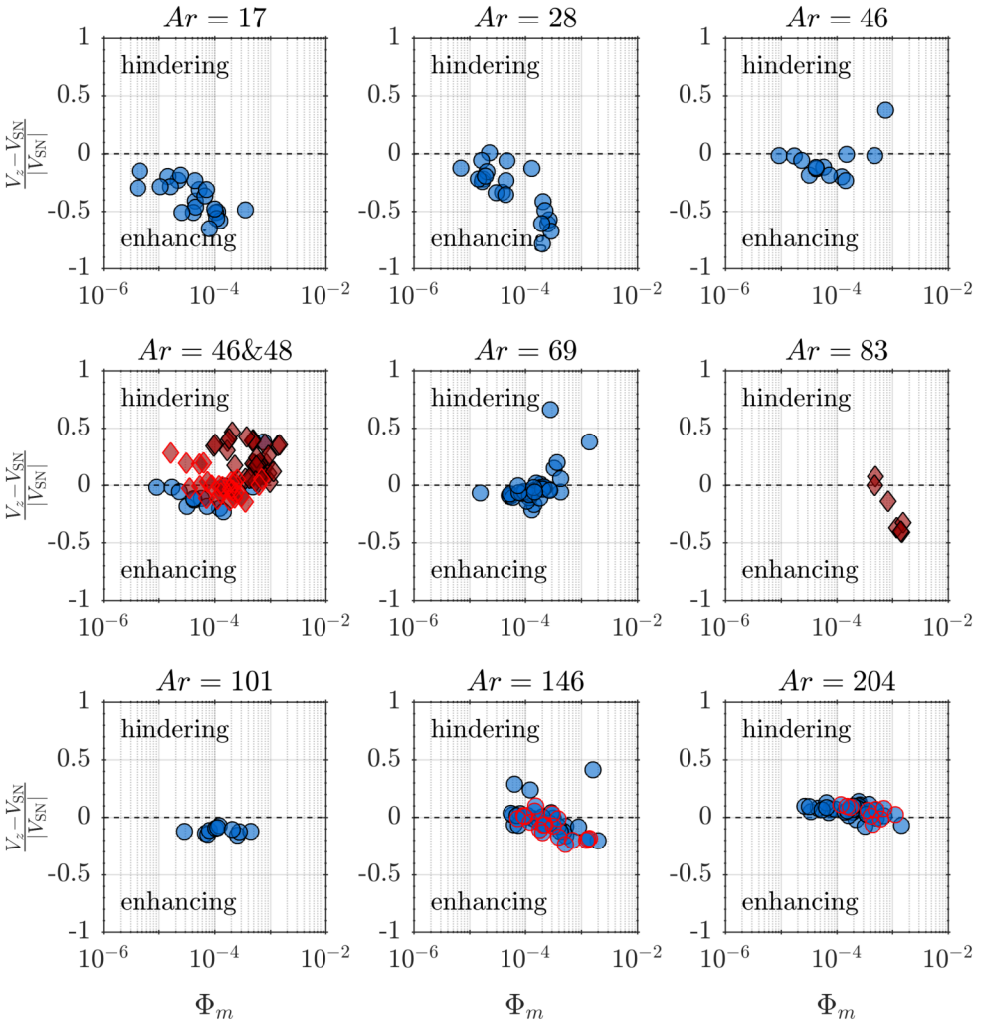

FIGURE 4.5: Settling velocity alteration measured on each plateau plotted against Φ_m, separated by Ar number values. Blue circle markers are from ceramic populations, red diamonds are from tungsten carbide populations. Red borders are placed over the marker edges of points where simultaneous PIV/PTV was performed. Since the CER 106-125 and TUN 063-075 have close Ar numbers values (resp. $Ar = 46$ and $Ar = 48$), both are plotted together in the same subfigure. As many points are then plotted in the same figure, the CER 106-125 are also plotted separately to clearly see their distribution and contribution.

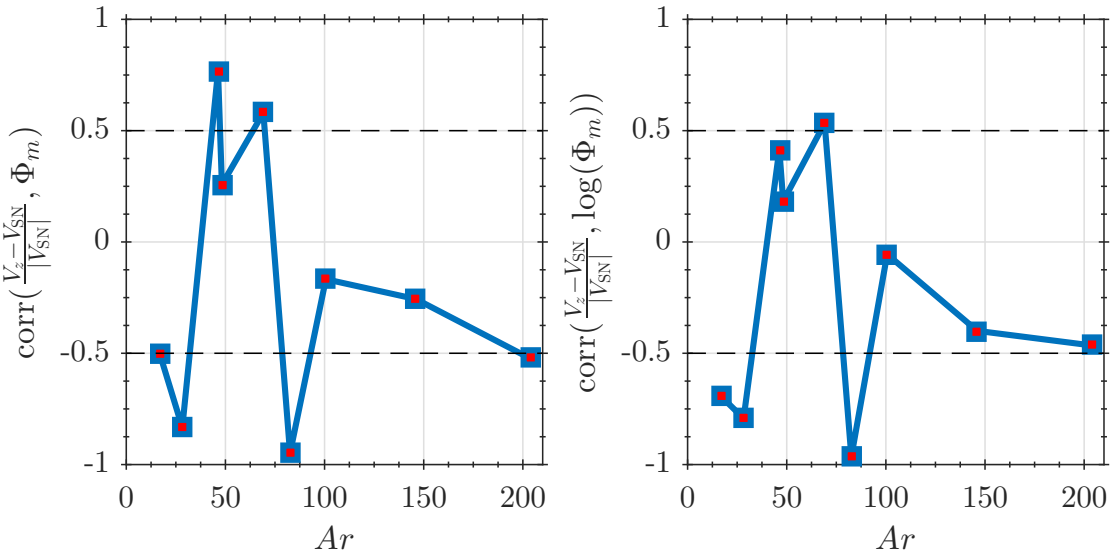

FIGURE 4.6: Pearson correlation coefficients obtained between $\frac{V_z-V_{SN}}{|V_{SN}|}$ and Φ_m on the left, and $\frac{V_z-V_{SN}}{|V_{SN}|}$ and $\log(\Phi_m)$ on the right. Both are done by particle populations, i.e. by fixed Ar.

the highest Φ_m of $Ar = 146$ lead to about a 20% increase in the settling velocity compared to the 70 to 80% increases observed for $Ar = 28$. So, while a trend of higher Φ_m resulting in higher enhancements can also be seen for $Ar = 146$, it is at a much reduced effect when compared with lower Ar numbers cases. Finally, the $Ar = 204$ population shows mostly hindered settling, with an observed reduction of 4 to 10%. Some higher loadings lead to higher settling velocities, but that trend remain feint and difficult to assess.

Attempts at computing whether Φ_m and $\frac{V_z-V_{SN}}{|V_{SN}|}$ are correlated were made for fixed Ar, using a Pearson correlation.The results from these computations are presented in figure 4.6. For two variables X and Y, this simple method looks for linear correlations between them by computing $\mathrm{corr}(X,Y) = \frac{\mathrm{cov}(X,Y)}{\sigma_X \sigma_Y}$, where $\mathrm{cov}(X,Y)$ is the covariance of X and Y, and σ_i is the standard deviation of variable i. The closer the correlation coefficient is to 1 (resp. -1), the stronger the tested variables are positively (resp. negatively) correlated. It is important to remember that the simple correlation coefficient chosen here is made to look for linear correlations, and other types of correlations might be completely missed. However, it can still give an indication of whether the two variables considered evolve in similar or opposite ways (e.g. high values for one corresponding to high values for the other). This correlation was computed first between $\frac{V_z-V_{SN}}{|V_{SN}|}$ and Φ_m, then between $\frac{V_z-V_{SN}}{|V_{SN}|}$ and $\log(\Phi_m)$. The two smallest Ar populations seem negatively correlated, which confirms the previous observation that higher loading increase settling velocities for low Ar numbers. The next three points swing towards positive correlations, however, when looking at the data distribution in figure 4.5 for $Ar = 46$

and $Ar = 69$, these correlations seem more driven by what seems like outliers, in the absence of more data. Additionally, the correlation coefficient remains quite low for $Ar = 48$ (i.e. smaller than -0.5 in absolute value). $Ar = 83$ results in a strong negative correlation, but this remains questionable as it is based on the smallest data set among the different particle populations, only 7 plateaus. For $Ar = 101$ and $Ar = 146$, no evidence of a strong correlation is found. Finally $Ar = 204$ nears a coefficient of -0.5 which might indicate the presence of a small correlation. Overall, these results are in line with what was observed in figure 4.5.

It is clear that the mass loading Φ_m can have an impact on the settling velocity. In our results higher Φ_m lead to increased settling velocities. This is in line with observations in the literature made with similar particle loadings. This impact of Φ_m is more pronounced for lower Ar numbers. Overall, Ar seems to have a stronger influence on the behaviour of the different particle populations observed here than Φ_m. However, the results still vary a lot, both within each particle population (fixed Ar) and across all parameters, and no other trend can firmly be established over the data produced here. As mentioned, this might come from a lack of data points on already tested particle populations, which the current set suffers from (especially for $Ar = 83$ and $Ar = 101$). But it might also come from other parameters and phenomena, not represented in the figures shown here. For example, the tungsten carbide populations might produce results that are clearly distinct from ceramics populations. Due to their density ratio Γ being almost 4 times higher than the ceramics, the way they interact with the fluid, and the flow they generate, can be different from other particles at similar Φ_m and Ar number. An additional parameter not studied here that could influence the behaviour of the system is the particle number density (number of particles over the considered volume). In fact, this parameter has been shown to have an influence on the decay of turbulence in particle laden flows [Letournel et al., 2020], or the energy required to maintain a given level of turbulence [Vessaire, 2020]. It is then plausible that this parameter can influence the way particles generate a flow in an initially quiescent fluid, which in turn could alter the way particles settle.

4.2 Concentration and clustering

4.2.1 Distribution of Voronoï cell areas: clustering

The distributions of the normalised Voronoï cell areas of the particles $\mathcal{V}$ are studied to find whether particles are clustering or not. To first illustrate these distributions,

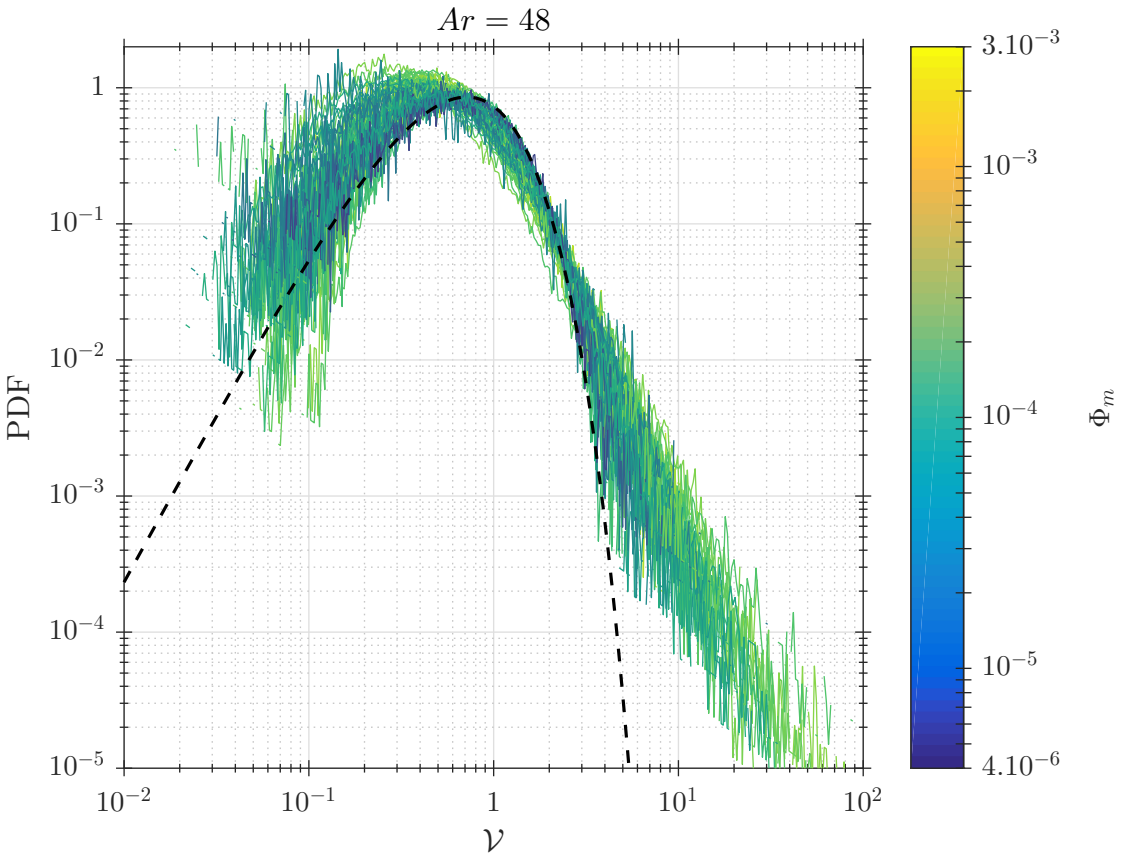

FIGURE 4.7: Distribution of the normalised Voronoï cell area $\mathcal{V}$ for all plateaus of experiments from $Ar = 48$ (TUN 063-075, $\Gamma = 15.63$). Each distribution is coloured according to the measured mass loading Φ_m. The black dashed line corresponds to the distribution of normalised Voronoï cells areas for randomly and uniformly placed particles (Random Poisson Process).

figure 4.7 shows the distributions of $\mathcal{V}$ for all plateaus at $Ar = 48$. One curve represent the distribution observed over one plateau. The dashed black line stands for the distribution of the normalised Voronoï cell areas of randomly and uniformly distributed particles, typically using a Random Poisson Process (RPP). The distributions presented in figure 4.7 are difficult to interpret as they have noisy tails. Higher mass loadings Φ_m seem to correspond to PDFs that deviate more from the RPP reference, presenting both more particles with large ($\mathcal{V} > 2$) and small ($\mathcal{V} < 0.5$) areas and less particles with intermediate areas. On a converged PDF, such behaviour would be indicative of clustering in the experiment, as both regions of high concentrations and voids become more observed than if particles followed the RPP distribution. But because our PDFs are not converged, such claim are difficult to affirm without a doubt. To reach more converged PDF, the data from multiple experiments can be combined to increase the quantity of raw data available. This however require a careful examination of the experiments to ensure that they fall in similar categories for the control parameters. This is especially true for Φ_m. This combination work is still under way.

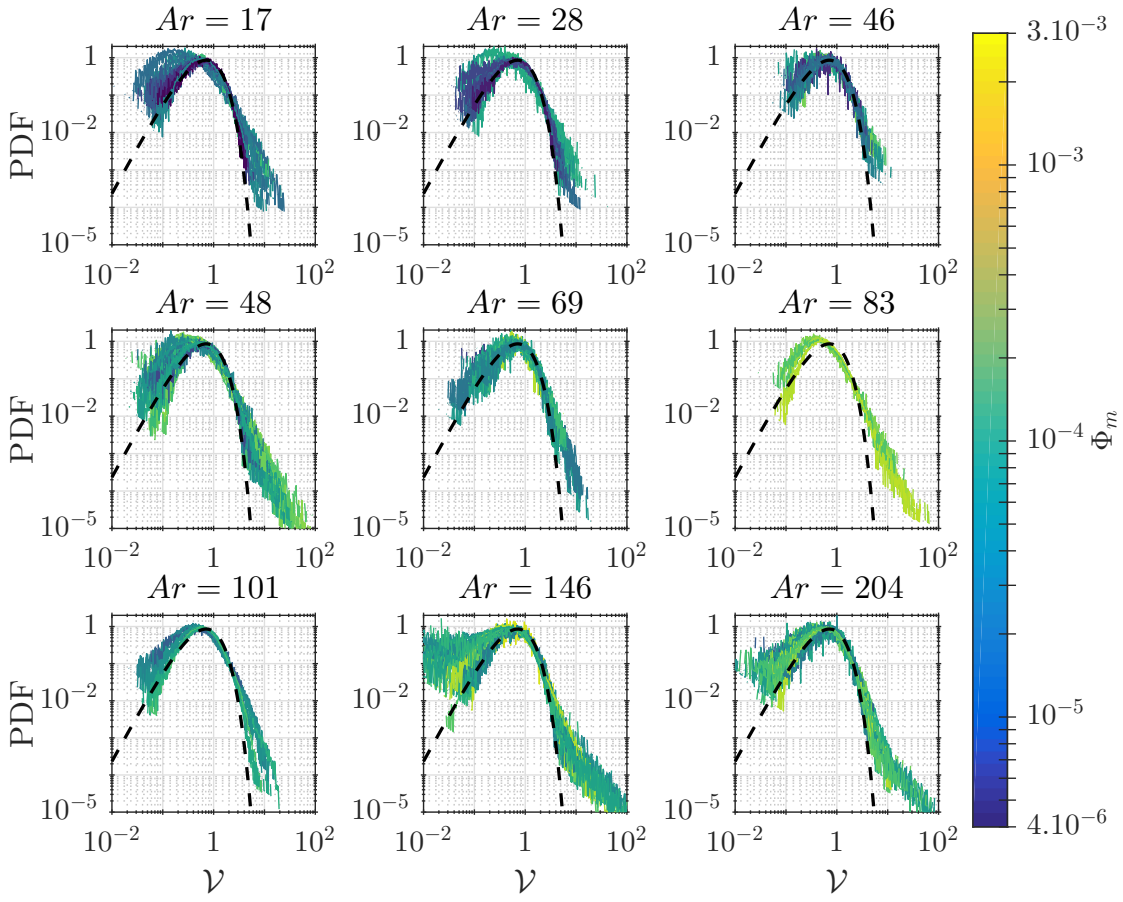

FIGURE 4.8: Distribution of the normalised Voronoï cell area $\mathcal{V}$ for all plateaus grouped by Ar number. Each distribution is coloured according to the measured mass loading Φ_m. The black dashed line corresponds to the distribution of normalised Voronoï cells areas for randomly and uniformly placed particles (Random Poisson Process).

The PDFs of $\mathcal{V}$ were also examined for all the plateaus at other Ar values. Figure 4.8 shows the distributions of $\mathcal{V}$ for all particle populations. For all particle populations, the presented PDFs have noisy tails. Like what was observed on figure 4.7, higher Φ_m seem to deviate more from the RPP reference for $Ar = 17$, $Ar = 28$, $Ar = 48$, $Ar = 83$. $Ar = 146$ and $Ar = 204$ are particularly difficult to interpret as they present PDFs over a large range of $\mathcal{V}$ that are particularly noisy. No trend in relation to $\mathcal{V}$ can easily be identified from these PDFs, as more converged tails would be required to be sure of any potential effect.

To quantify how each experiment compares with the RPP reference, the standard deviation of the normalised Voronoï cell areas $\sigma_\mathcal{V}$ has been computed. As none of the PDFs presented here show specific shapes, e.g. a peaked distribution which would indicate an ordered system, $\sigma_\mathcal{V}$ can then be measured against the value expected of an RPP distribution $\sigma_\mathcal{V}^{\text{RPP}} = 0.53$ [Ferenc and Néda, 2007]. The greater $\sigma_\mathcal{V}$ is above $\sigma_\mathcal{V}^{\text{RPP}}$, the more likely it is that clustering is present. However this has to be pondered by the fact that the PDFs are very noisy, and their irregular tails might factor a lot in the computation

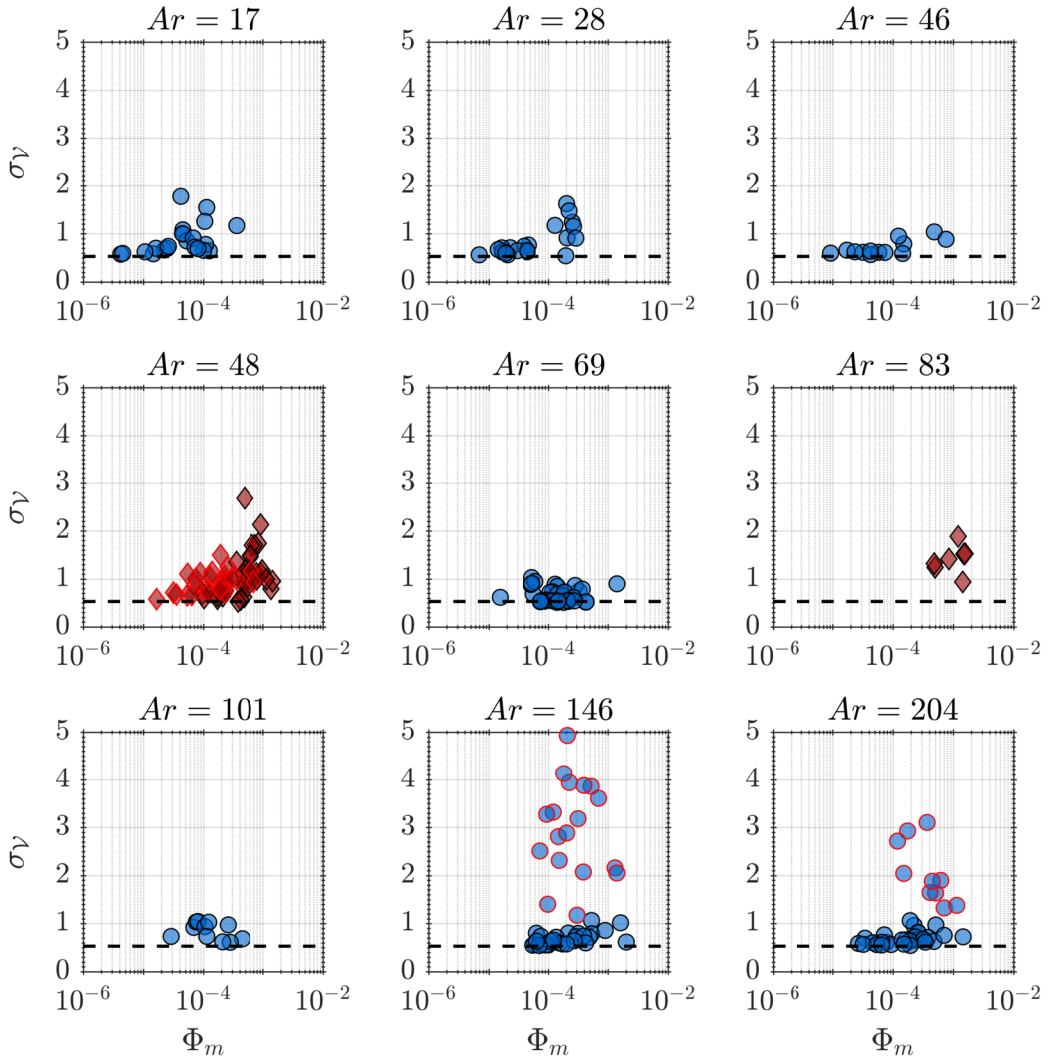

FIGURE 4.9: Standard deviations of $\mathcal{V}$ for all experiments, grouped by Ar number. Blue circle markers are from ceramic populations, red diamonds are from tungsten carbide populations. Red borders are placed over the marker edges of points where simultaneous PIV/PTV was performed. The black dashed line corresponds to the standard deviation of the distribution of normalised Voronoï cells areas for randomly and uniformly placed particles (Random Poisson Process).

of $\sigma_\mathcal{V}$. Figure 4.9 represents scatter plots of $\sigma_\mathcal{V}$ for each experiments against Φ_m for all particle populations. It is clear there that for populations CER 160-180 ($\Gamma = 4$, $Ar = 146$) and CER 180-200 ($\Gamma = 4$, $Ar = 204$) the experiments for which PIV was performed detach themselves from the rest of the data. This is however not the case for population $Ar = 48$. A possible interpretation of this will be given at the end of the present section. The previously mentioned trend of higher Φ_m leading to greater deviations from the RPP reference can somewhat be seen for $Ar = 17$, $Ar = 28$, $Ar = 48$ and $Ar = 83$. This point toward an influence of Ar and Γ similar to what was observed for $\frac{V_z - V_{SN}}{|V_{SN}|}$ in section 4.1.2, but on the development of clustering in this case, although

the values of $\sigma_{\mathcal{V}}$ have to be taken with caution here.

The values of $\sigma_{\mathcal{V}}$ have also been averaged for each population by categories of Φ_m, and are plotted against Ar in figure 4.10. The categories of Φ_m chosen are the same as those from figure 4.4. The trends previously outlined can also be seen here. The two highest Ar populations present points with extremely large error bars due to the previously mentioned non resolved issue between experiments performed with and without tracers. They cannot be representative of any trend due the high variability in the results and will be ignored for now. For similar Ar values, the higher Γ population lead to higher values of $\sigma_{\mathcal{V}}$. However, experiments on more populations of tungsten carbides ($\Gamma = 15.63$) would be necessary to confirm this trend. Over the ceramics populations ($\Gamma = 4$), lower Ar also tend to have more variability between experiments, and slightly higher $\sigma_{\mathcal{V}}$ values. The previously observed trend of higher Φ_m being correlated with higher $\sigma_{\mathcal{V}}$ mentioned in figure 4.9 can be seen here again, as the higher loading categories present generally higher $\sigma_{\mathcal{V}}$ values.

To see whether clustering can be linked with settling alteration, scatter plots of the settling velocity alteration $\frac{V_z - V_{SN}}{|V_{SN}|}$ as functions of $\sigma_{\mathcal{V}}$ are presented in figure 4.11, separated by Ar values. $Ar = 69$ and $Ar = 101$ does not seem to show any specific link between $\frac{V_z - V_{SN}}{|V_{SN}|}$ and $\sigma_{\mathcal{V}}$. For $Ar = 17$, $Ar = 48$ and $Ar = 83$, higher $\sigma_{\mathcal{V}}$ seem to be linked with particles that fall faster, i.e. more negative $\frac{V_z - V_{SN}}{|V_{SN}|}$ values. This trend can somewhat be observed for $Ar = 28$ and $Ar = 46$ although to a lesser extent. This suggests that, if clustering is indeed observed, clustering and higher settling velocities are correlated in our experiments. Due to the previously mentioned issue with simultaneous PIV and PTV experiments, the $Ar = 146$ and $Ar = 204$ will not be commented on further.

Although it seems certain that some experiments present cases of clustering (especially when looking at lower Ar particle populations), this is probably not caused by effects that arise from local interactions between the particles and small flow structures, like what can be observed in a turbulent flow. Such small scale interactions leading to a modification of a particle's trajectory are generally called preferential concentration effects in the literature. This is distinct from clustering, as clustering is simply the observation that particles are grouped in the flow and leave some regions of the fluid empty. Preferential concentration lead to clustering, but clustering can be observed without preferential concentration. In the absence of turbulence, the small scale flow structures in our experiments are the particles wakes, and it is unlikely that these wakes are responsible for the clustering observed in the results presented here.

In the literature, preferential effects have been observed with increasing intensity as the Archimedes number rises [Huisman et al., 2016, Uhlmann and Doychev, 2014], which is the opposite of what can be observed in our experiments. When the Archimedes number

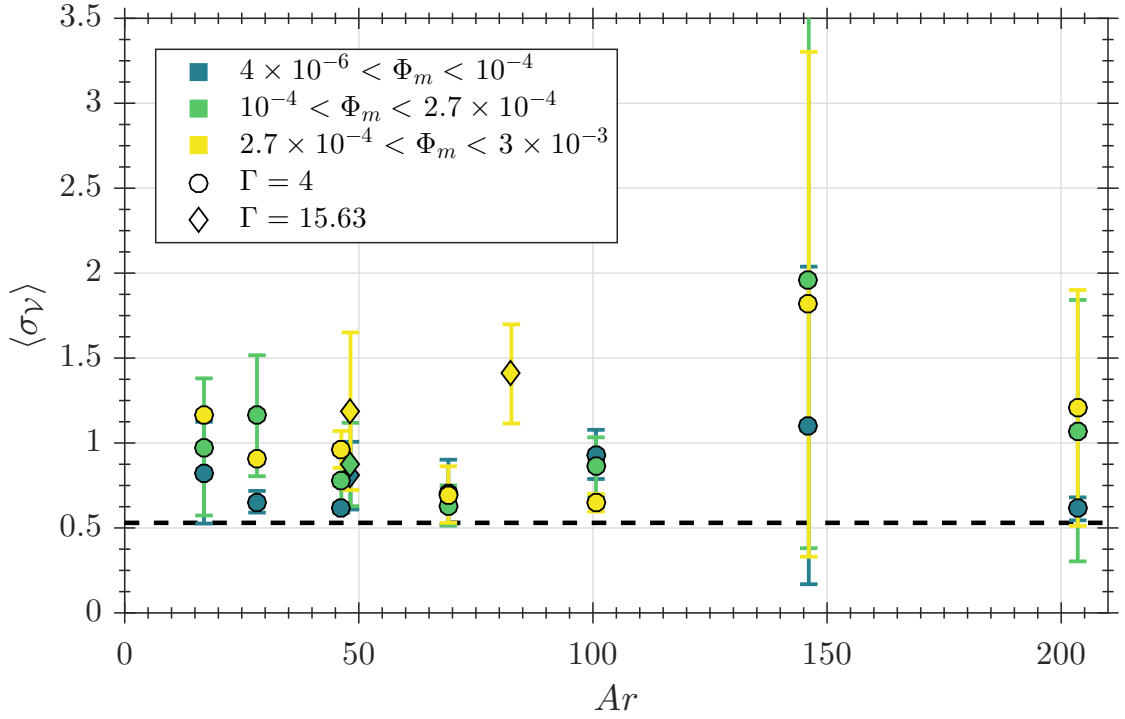

(A)

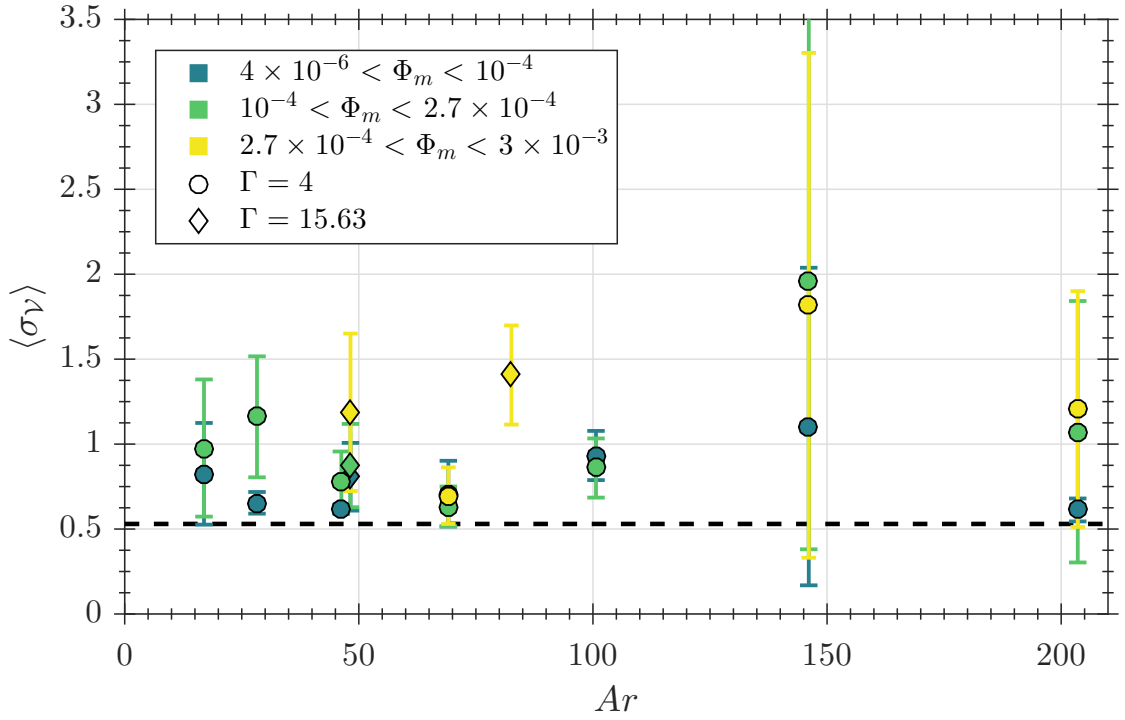

(B)

FIGURE 4.10: Mean of the standard deviation of $\mathcal{V}$ against Ar, grouped by ranges of Φ_m. These ranges where chosen so that the same number of experiments fall in every one of them. Subfigure (A) represents all data. Points that would represent only one or two experiments have been removed from subfigure (B). The error bars here represent one standard deviation above the mean and one below. The black dashed line corresponds to the standard deviation of the distribution of normalised Voronoï cells areas for randomly and uniformly placed particles (Random Poisson Process).

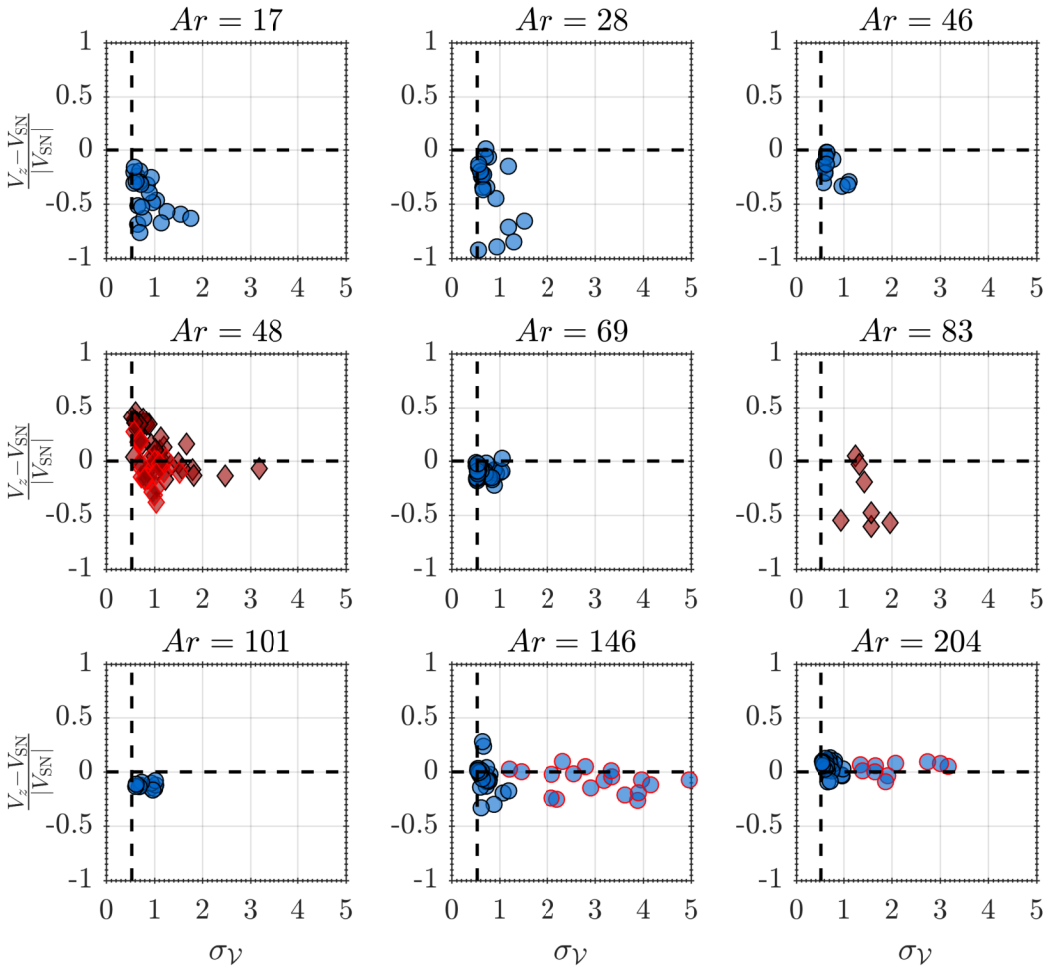

FIGURE 4.11: Scatter plots of the settling velocity alteration against the standard deviation of the normalised areas of the Voronoï cells $\sigma_{\mathcal{V}}$, grouped by Ar number. Blue circle markers are from ceramic populations, red diamonds are from tungsten carbide populations. Red borders are placed over the marker edges of points where simultaneous PIV/PTV was performed. The vertical black dashed line corresponds to the standard deviation of the distribution of normalised Voronoï cells areas for randomly and uniformly placed particles (Random Poisson Process).

of a particle goes above $Ar \approx 24000$, a first wake transition occurs, the wake switching from steady and vertical to steady and oblique. The change in the particles' wake at that transition makes them more likely to cross paths and be trapped in the wakes of other particles. They then follow each other more and group into columns, hence an increased clustering from wake interactions when Ar increases. Our particle populations have Archimedes numbers that are below those of populations tested in the articles cited in section 1.2, our current maximum being $Ar = 204$. This is significantly under the Archimedes number of the first wake transition that is linked with the increased clustering. Our particles then have no reason to group themselves based on their wakes alone.

Moreover, we have observed that the column of falling particles sometimes present wavy patterns, oscillating sideways as the particles fall for some experiments. In the case of tungsten carbide particles, this sometimes even looked like a series of alternating vortices. Due to the geometry of our experimental device, particles fall in two different confined environments: the injection column first, then the larger main tank. As the particles drag down a portion of the fluid with them, the fluid has to rise somewhere else, so large scale flows necessarily develop. These shapes could indicate the development of mixing layers within the experiment. The fluid falling with the particles in the center of the experimental device can be viewed as a jet. Large scale vortices are then generated from this 'jet', which mix the fluid falling with the particles with the surrounding fluid without any particles. This mixing takes the form of large scale vortices that alter the particles trajectory and consequently their distribution by introducing in the column of falling particles fluid that contains no particles at all. This effect would then become more prevalent for experiments where either the mixing is more pronounced or particles are more likely to be swept by the flow. These two cases could potentially be attributed to higher particle mass loadings and density for the first and lower inertia particles (i.e. lower Ar) for the other, but these require fluid measurements to be confirmed. Some elements on that will be presented in section 4.3.

Because void regions corresponds to larger $\mathcal{V}$, they naturally will also contribute more to the value of $\sigma_{\mathcal{V}}$. Given the non converged state of the PDF tails presented in figures 4.7 and 4.8, it is important to point out that the values of $\sigma_{\mathcal{V}}$, mainly driven by the void regions, are then also mainly driven by those non converged values. A decomposition to see the contributions of the clustered and void regions to $\sigma_{\mathcal{V}}$ could be performed, like was done by Sumbekova in her thesis [Sumbekova, 2016] This would help in seeing whether only the voids introduced by the mixing are responsible for the observed higher values of $\mathcal{V}$ or if clustered regions also have a higher contribution than expected of an RPP distribution.

The large scale flows are also probably responsible for the differences in $\sigma_{\mathcal{V}}$ observed between the measurements performed with and without tracers for $Ar = 146$ and $Ar = 204$. In regard to the Voronoï cells of the particles, the introduction of tracers in the experiment can have two effects: they can remove particles that are too close to a detected tracers, or introduce false particles if the tracer is not removed by the mask, as explained in section 3.2.2. It is likely that the second effect is less probable, as an undetected tracer will probably be less intense on the images of both camera, and is thus also less likely to be detected as a particle when performing PTV. In any case, a random and uniform distribution of tracers should not have any impact on the overall distribution of particles and their Voronoï cell areas. This is because a homogeneous subsampling of the particles is harmless to the normalised statistics of a Voronoï cell

area distribution [Monchaux et al., 2010]. However if tracers are not randomly and uniformly distributed, they could induce an error in the measures. Let's suppose that the concentration of tracers is for example higher in the main tank of the experiment than in the injection column. The mixing process described above would then conduct more tracers to be in the regions of the fluid where not many particles are present already. The removal of these particles in the void regions would then accentuate those voids in the Voronoï analysis, voids that by nature contribute more to $\mathcal{V}$. This effect has been observed on the images from these experiments. Because less tracers where used in the experiments of $Ar = 48$ than for the $Ar = 146$ and $Ar = 204$ cases, it is then more visible on the results from the latter two populations. The double measurements method has only been recently developed and we are still in the process of tuning it to our experiments. More work is needed on the way tracers are seeded in the experimental device to ensure a more homogeneous distribution. The double measurements data remain valid in terms of measured velocities, but further testing and investigations are necessary for it to be valid and relevant in the context of a Voronoï analysis to look for clustering phenomena.

4.2.2 Local concentration

To ascertain whether local effects are at play here, the velocities of each particle can be looked in regards to their local concentration. Figure 4.12 presents the joint PDFs of velocity alteration for each particle $\frac{v_z - V_{SN}}{|V_{SN}|}$ with their local normalised Voronoï area $\mathcal{V}$. This figure groups all experiments of a given particle population (fixed Ar) in the same subfigure. Across all particle populations, there does not seem to be a clear trend linking local concentration and settling velocity alteration. Although not represented here, figures of these joint PDFs have also been generated for each plateau. No trend linking $\frac{v_z - V_{SN}}{|V_{SN}|}$ and $\mathcal{V}$ has been observed on these figures either.

To try and measure whether the velocity alteration of a particle is correlated to its local concentration, Pearson correlation coefficients have also been computed between $\frac{v_z - V_{SN}}{|V_{SN}|}$ and $\mathcal{V}$ on the one hand, and $\frac{v_z - V_{SN}}{|V_{SN}|}$ and $\log(\mathcal{V})$ on the other hand, for each experimental plateau. The correlation coefficients between $\frac{v_z - V_{SN}}{|V_{SN}|}$ and $\log(\mathcal{V})$ are presented in figure 4.13 against Φ_m and separated by particle population. Across all experiments, no significant correlation is found between the tested variables. The results are similar for the correlation between $\frac{v_z - V_{SN}}{|V_{SN}|}$ and $\mathcal{V}$ (not represented here), the values of the correlation coefficient being slightly closer to 0.

As a quick remark, looking at the $Ar = 48$ case on figure 4.13, clear horizontal lines can be seen in the joint PDF. This can also be seen on the $Ar = 17$ case to a lesser

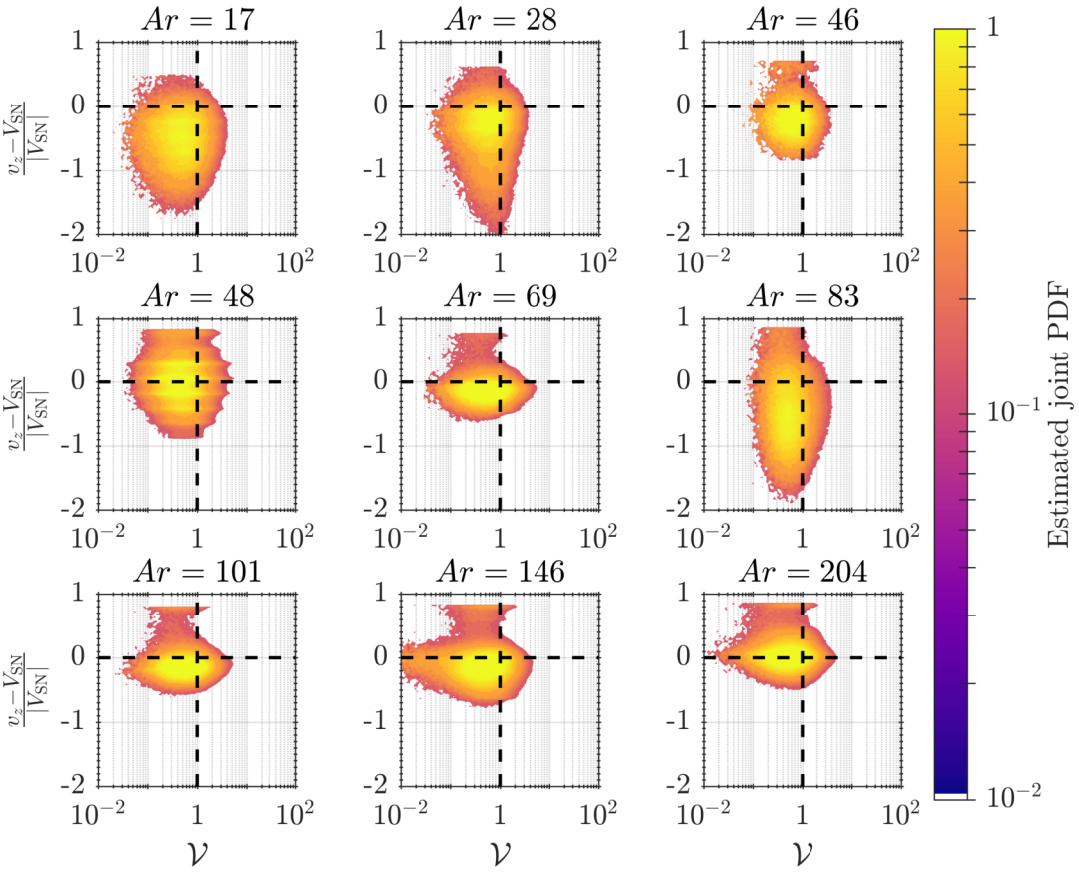

FIGURE 4.12: Estimated joint PDF of the settling velocity alteration, using the Schiller-Naumann model as a reference, against the normalised Voronoï area of the particles. These PDF are estimated using the data from all plateaus for each particle population.

degree. This correspond to a pixel locking issue. This issue likely arise from particles being too small on the images, and can easily be fixed by increasing the resolution of our particles, be it by changing our camera objectives or simply moving them closer to the experiment. Although the field of view of the cameras will then be smaller, the pixel locking issue will be removed.

Overall, settling velocity alteration has been observed, and stronger alteration of that settling velocity seem correlated with higher deviation from a random and uniform distribution of the particles. Whether these deviations correspond to clustering or not remains uncertain. Additionally, because there does not seem to be any influence of the local concentration on the velocity alteration in our cases, the settling alteration is probably more influenced by large scale flow structures that affect all particles relatively equally, rather than by smaller local structures. This is in line with the interpretation of the mixing layers discussed previously. Regions of voids are introduced in the falling column of particles by mixing it with the surrounding fluid. The vortices generated by this mixing effect are large scale structures that generally affect all particles without

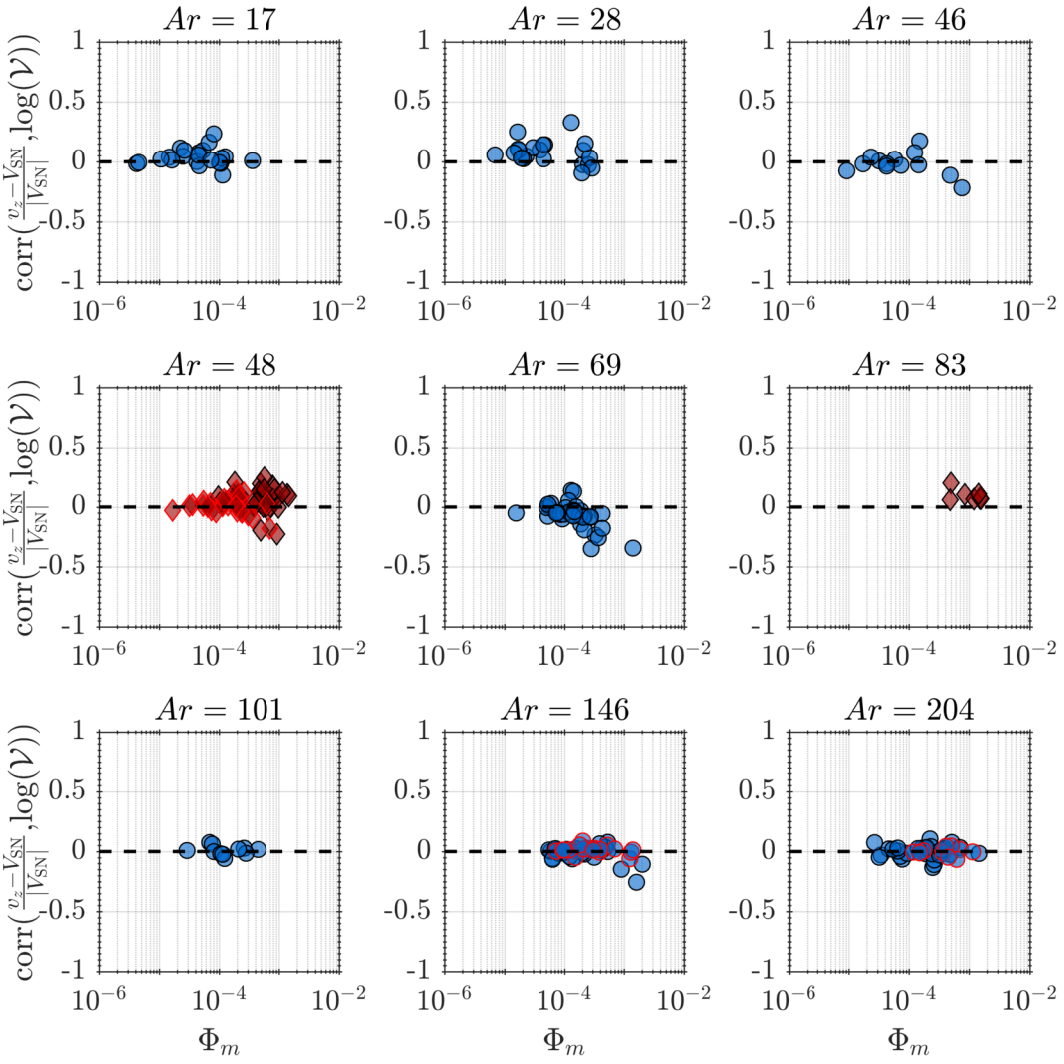

FIGURE 4.13: Pearson correlation coefficient between the settling velocity alteration and $\log(\mathcal{V})$ of each experimental plateau against Φ_m, grouped by Ar number. Blue circle markers are from ceramic populations, red diamonds are from tungsten carbide populations. Red borders are placed over the marker edges of points where simultaneous PIV/PTV was performed.

distinctions. Further investigation on the flow generated by the particles is provided in section 4.3.

4.3 Double phase measurements

Experiments using the double measurement technique described in chapter 3 have been performed for three particle populations: CER 160-180, CER 180-200 ($\Gamma = 4$, and $Ar = 146$ and $Ar = 204$ respectively) and TUN 063-075 ($\Gamma = 15.63$, and $Ar = 48$). The

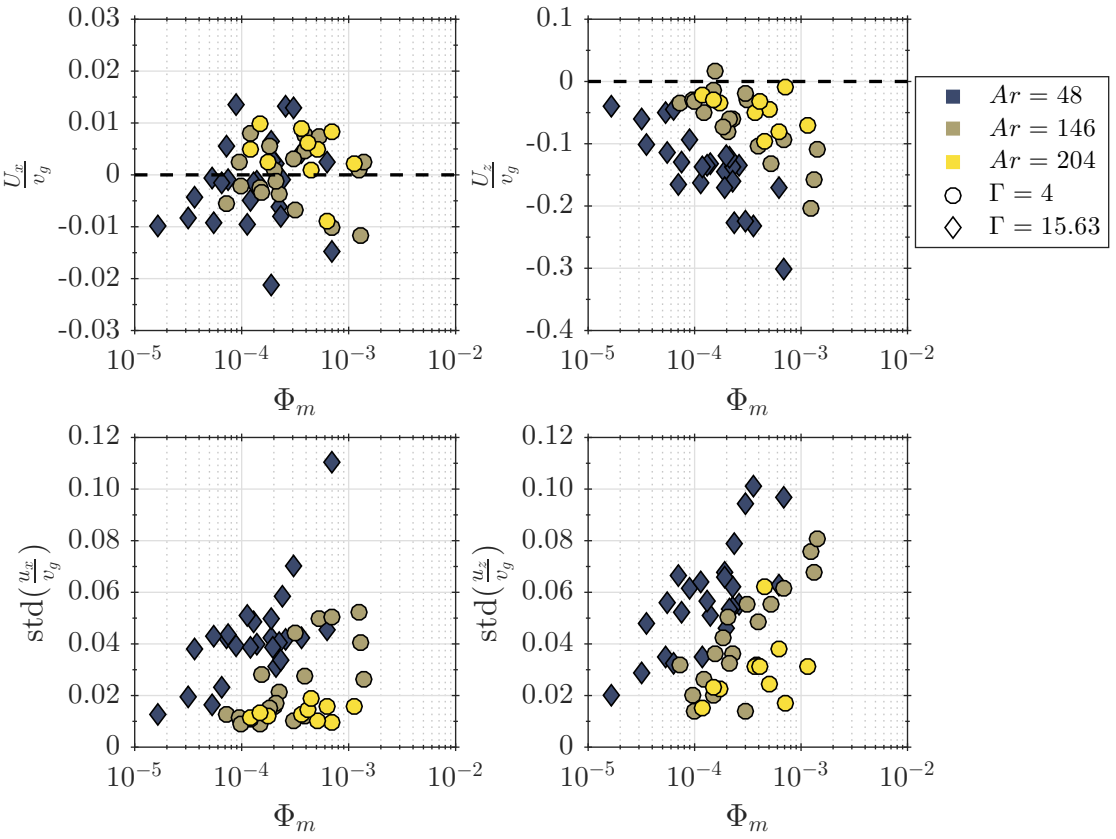

FIGURE 4.14: Scatter plots of the horizontal (u_x) and vertical (u_z) velocities of the fluid plotted against the mass loading in particles. The left side is the horizontal velocity, the right side is the vertical one. The top row is the average of the velocity over each plateau's region of interest. The bottom row is the standard deviation. All velocities are normalised using the gravitational velocity used in the computation of Ar: $v_g = \sqrt{(\Gamma - 1)g\bar{d}}$. The markers are coloured according to the Archimedes number of the particle population. Diamonds represent tungsten carbide particles ($\Gamma = 15.63$), circles represent ceramics particles ($\Gamma = 4$).

results from the joint analysis of the PIV and PTV measurements are presented in this section.

4.3.1 Background flow

A first point to look at is how the particles' characteristics affect the flow generated in the carrier phase. The averages of the horizontal and vertical fluid velocities over the regions of interests of each plateau are plotted against Φ_m in the top subplots of figure 4.14. Velocities are normalised using the gravitational velocity $v_g = \sqrt{(\Gamma - 1)g\bar{d}}$, as explained in section 2.3.2. As can be expected, $\frac{U_x}{v_g}$ is distributed around zero for all particle populations. Φ_m has no influence on this. $\frac{U_z}{v_g}$ on the other hand shows that the fluid generally develop a downward flow, with values one order of magnitude above what $\frac{U_x}{v_g}$ displays. Moreover, for all particle populations, higher Φ_m lead to higher magnitudes for the vertical velocity. The bottom two subplots of figure 4.14 show the

standard deviations of the vertical and horizontal velocities, once again normalised by v_g. Both std($\frac{u_x}{v_g}$) and std($\frac{u_z}{v_g}$) take on similar values, with a trend for all particle populations that higher standard deviation values occur for higher values of Φ_m (maybe with the exception of CER 180-200 (yellow markers) for std($\frac{u_x}{v_g}$)).

When settling, the particles locally generate a downward flow, that can be seen in the region of interest defined for each plateau. The large scale upward flow, that has to exist in our confined system to compensate this, likely occurs outside of the region of interest, or even outside of the cameras field of view. Because the particles are settling, U_x stays close to zero while U_z is negative. For U_x, the deviations from zero that can be seen in figure 4.14 probably come from transitory regimes captured within the plateaus. For example, going back to the idea of large scale eddies coming from mixing layers, if the plateau does not last long enough to let a sufficient number of those eddies pass through the region of interest, the average of the horizontal velocity will deviate from zero. However, even then, those deviations remain an order of magnitude smaller than the averages obtained for the vertical velocities. The influence of Φ_m in this regard is also understandable. Higher Φ_m for a given population simply translates to a higher number of particles settling in the experiment. More particles will drag more fluid with them when they settle, and the fluid will show higher magnitudes for its vertical velocity on average as a result.

The standard deviations give a measure of the time fluctuations and spacial inhomogeneities around the averages. It is interesting to see that the fluctuations are of the same order of magnitude in both the horizontal and the vertical directions. Φ_m also has an influence here. For any given population, higher Φ_m simply means that more particles are present in the system. As more particles settle, it also means that more particle wakes are interacting, which leads to more fluctuations in the fluid velocities, both vertical and horizontal. These observations on the background flow generated by the particles are also in line with the interpretation of mixing layers. Higher numbers of particles generate a stronger downward flow, akin to a stronger jet, that will then present more 'turbulent' mixing layers, hence more fluctuations in velocity in both directions observed for higher Φ_m. This is supported by the direct observation of somewhat vortical structures and wavy patterns in the column of settling particles and its surrounding fluid, as illustrated in figure 4.15. More work is required to determine whether those values arise from spatial or temporal fluctuations.

As we have double measurements on only three populations the potential effects of Ar and Γ remain difficult to assess, and measurements on more particle populations are needed. Γ seems to play an important role, as $\Gamma = 4$ and $\Gamma = 15.63$ are separated in all the subplots of figure 4.14. The higher Γ population lead to higher fluctuations in

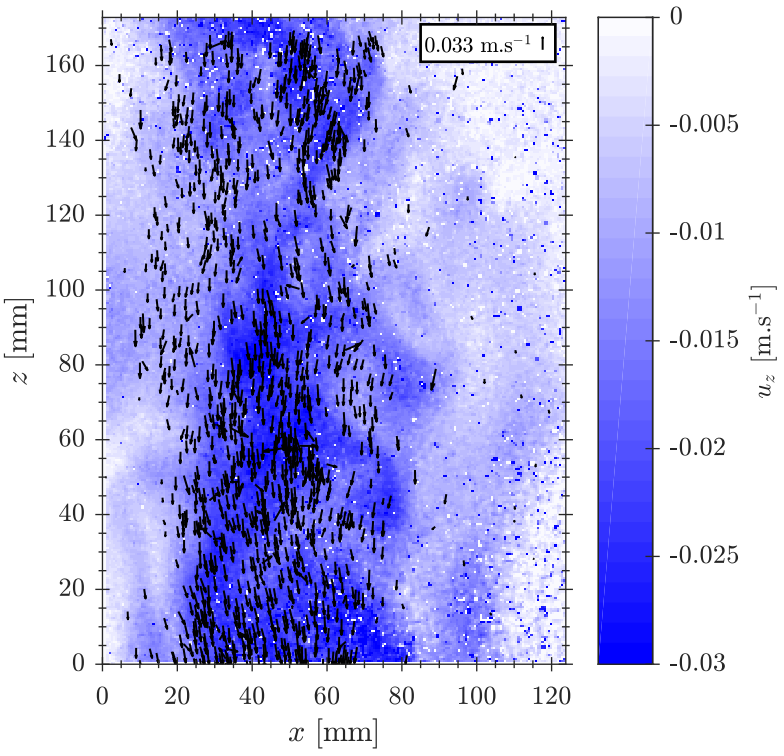

FIGURE 4.15: Instantaneous particle velocities (arrows) and fluid vertical velocity fields u_z (color-plot) at $t = 50$ s taken from experiment shown in figure 4.18b.

both directions and higher magnitudes for the vertical fluid velocity for a given mass loading Φ_m. Following the trends observed in figures 4.4 and 4.5, Ar might also have an influence when low enough, that would here be masked by Γ having a greater effect. More double measurements with both tested Γ at different Ar values are necessary to test whether Ar has an effect on the fluid or not.

4.3.2 Slip velocities

The slip velocities between the particles and the fluid in both the horizontal and vertical direction are shown in figure 4.16, plotted against Φ_m. For the horizontal velocity, the measurements fluctuate around zero. $\Gamma = 4$ (circles in the figure) results in horizontal slip velocities that are closer to zero while $\Gamma = 15.63$ (diamonds in the figure) spreads a bit more. Φ_m does not have an influence. For the vertical velocity, the points line up on values that depend on the density of the population, around -0.18 for $\Gamma = 15.63$ and -0.41 for $\Gamma = 4$. For each particle populations some points deviate from these lines at higher Φ_m.

Because neither the fluid nor the particles were observed to have any strong horizontal component and both were generally around zero, no particular slip velocity was to be expected in this direction. The fact that the $\Gamma = 15.63$ points are more spread might

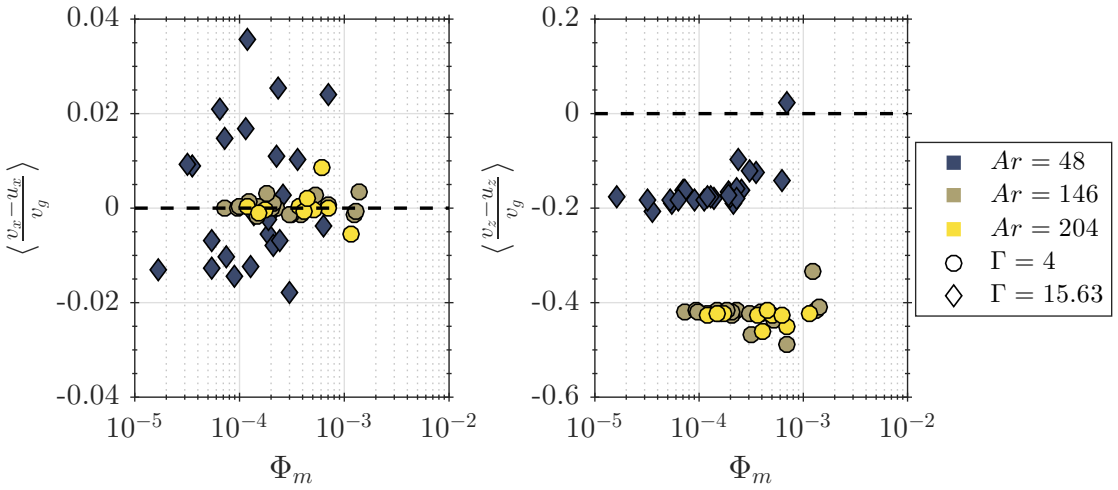

FIGURE 4.16: Scatter plots of the averages of the horizontal ($\langle v_x - u_x \rangle$) and vertical ($\langle v_z - u_z \rangle$) slip velocities between the particles and the fluid plotted against the mass loading in particles. All velocities are normalised using the gravitational velocity used in the computation of Ar: $v_g = \sqrt{(\Gamma - 1)g\tilde{d}}$. The markers are coloured according to the Archimedes number of the particle population. Diamonds represent tungsten carbide particles ($\Gamma = 15.63$), circles represent ceramics particles ($\Gamma = 4$).

come from differences in the tracer seeding conditions between the $\Gamma = 15.63$ and $\Gamma = 4$ experiments. As more tracers were used for the $\Gamma = 4$ experiments, the resulting PIV are also more accurate at measuring small velocities, like the one that can be expected in the horizontal direction. Moreover, the particle population of the $\Gamma = 15.63$ data presented here also corresponds to the experiments where pixel locking is observed the most.

In the vertical direction, the particles settle with a constant slip velocity with respect to the fluid. A simple decomposition can be made when analysing the velocity of the settling particles as the sum of the slip velocity and the fluid velocity: $v_z = (v_z - u_z) + u_z$. Using this decomposition, because we observe that the slip velocity is constant for a given particle population, the differences in settling velocities observed then mainly come from the flow generated by the particles. The points are clearly separated by Γ values, but not so much by Ar values. This suggests that the differences observed between the two density ratios of the particles tested so far, e.g. as seen in figure 4.3 or 4.4, would mainly come from how changing Γ leads to differences in the flow that the particles generate when they fall.

To explain this behaviour, it can be considered that the particles fall at their theoretical terminal velocity (based on the Schiller-Naumann drag model in our case) and that any additional mean flow would then simply be an additional push. In essence, particles fall at their terminal settling velocity in a frame of reference that moves at the mean flow velocity. The slip velocity then becomes the theoretical settling velocity of the particles which in the previous decomposition then corresponds to: $v_z = V_{\mathrm{SN}} + u_z$. The

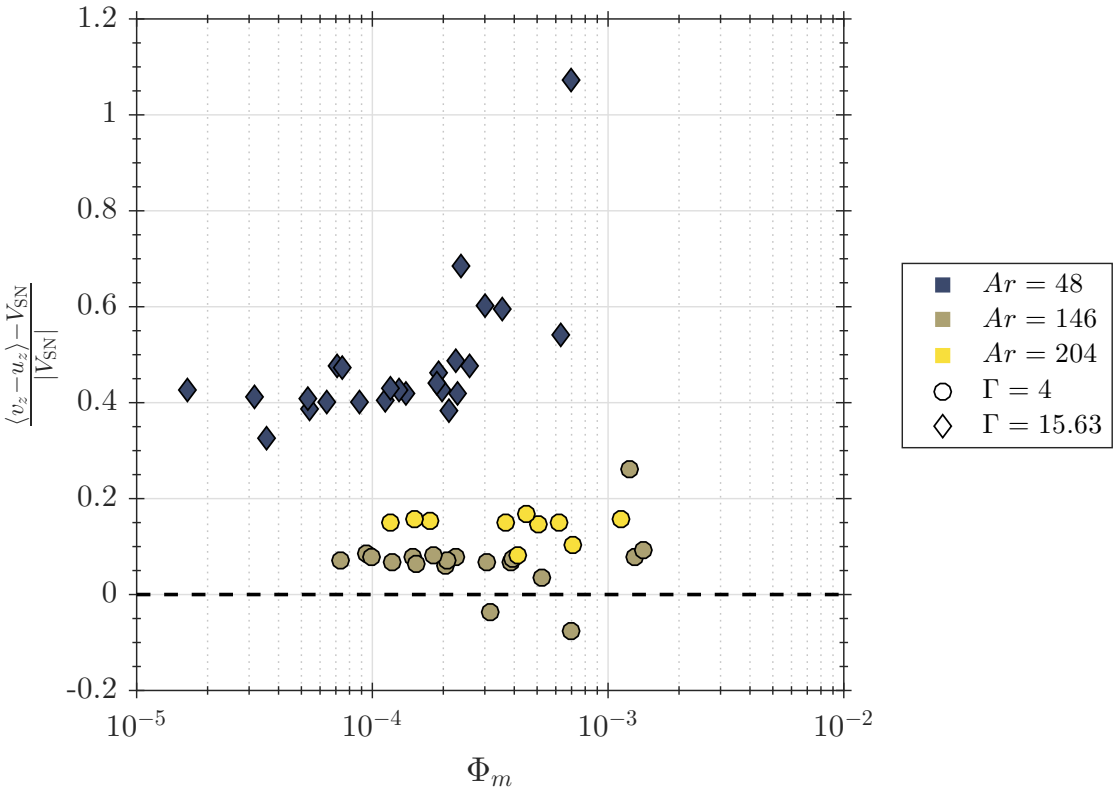

FIGURE 4.17: Scatter plot of the average of the vertical ($\langle v_z - u_z \rangle$) slip velocities normalised by the particle populations Schiller-Naumann settling velocity V_{SN} plotted against Φ_m. The markers are coloured according to the Archimedes number of the particle population. Diamonds represent tungsten carbide particles ($\Gamma = 15.63$), circles represent ceramics particles ($\Gamma = 4$).

numerical data from Uhlmann et al [Uhlmann and Doychev, 2014] goes in favour of this interpretation, as in their simulations the increase in the particle settling velocity is attributed to the flow of the fluid that surrounds them, and the slip velocity of the particles then falls right below a few percent of the expected settling velocity of a single particle. To look at our data through that interpretation, the slip velocity has been normalised using the Schiller-Naumann settling velocity, in a similar fashion to what was done in figure 4.3, and plotted against Φ_m in figure 4.17. The resulting values are for the vast majority positive, i.e. in the hindering region of the figure. Γ still separate the data in clear groups, and while the different Ar values are also more distinct from one another in their results, no trend can be easily identified in that regard as only three Ar cases have been experimented on. For all tested particle populations, the results suggest that the particles fall at lower velocities than their theoretical terminal velocity when in a frame of reference that moves at the average fluid velocity. This hindering is also quite substantial, notably for $\Gamma = 15.63$ where it is generally above 40%.

A way to interpret those differences between the proposed model and our results is that the dynamics observed on our plateaus correspond to non fully developed phenomena.

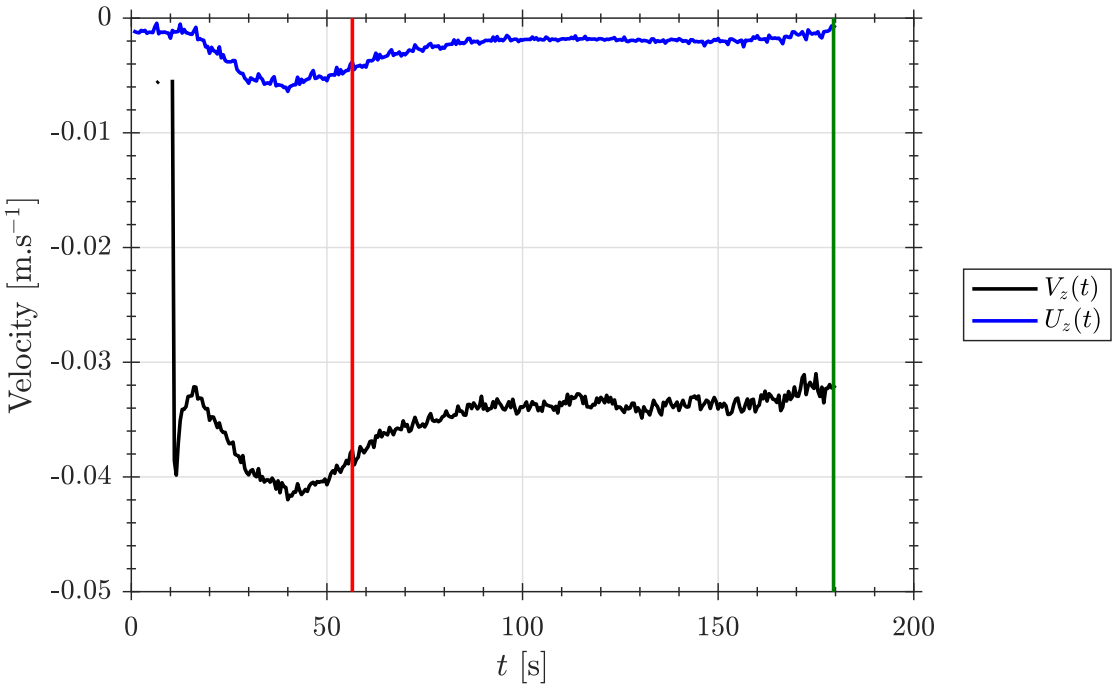

(A) CER 160-180, $\Gamma = 4$, $Ar = 146$

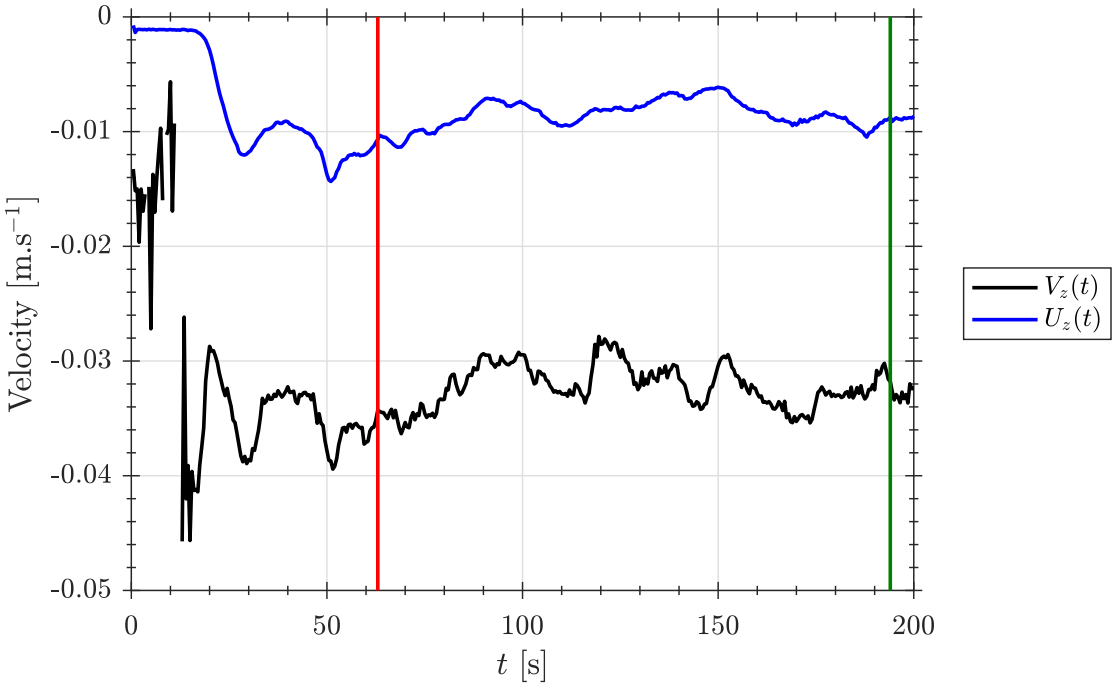

(B) TUN 063-075, $\Gamma = 15.63$, $Ar = 48$

FIGURE 4.18: Examples of temporal traces of the fluid vertical velocity U_z and the particles vertical velocity V_z. The averages are performed at each instant over the region of interest defined for the plateau of the experiment. The red vertical lines denotes the beginning of the plateau and the green one the end.

First, the choice of the plateau boundaries might be put into question. Due to the fact that the double measurements are a late addition to the experimental process, fluid quantities where not considered when establishing the plateaus' boundaries. It is then reasonable to think that the flow might not be in a state converged enough for the computed statistics to be relevant over the duration of a plateau. To look into this, the temporal traces of the average of the particles' and the fluid's vertical velocity over time have been plotted for all experiments. Examples of such plots can be found in figure 4.18. For the vast majority of the plateaus presented in this thesis, the fluid measurements at most indicate that some instants should be removed from the beginning and/or the end of the plateaus, like for example in figure 4.18a. Figure 4.18b shows a less converged system, although this intermittency might be unavoidable for the heavier and more loaded experiments (e.g. tungsten carbide particles here, $\Gamma = 15.63$). Going forward, the process used to define plateau edges will be refined using the fluid measurements as well. The plateaus used up to now then correspond to non transitory dynamics.

Another way to interpret the divergences between the proposed model and our results is that the dynamics within our experimental device cannot reproduce the conditions necessary for the model to be relevant due to scale issues. The flow is driven by the particles falling, but is also constrained by the geometry of our experimental device. As such, a large scale flow develops, falling with the particles in the center and going up on the sides of the experiment. Geometrical constraints like ours are not present in the cited numerical work [Uhlmann and Doychev, 2014] as they use periodic boundary conditions. Our experiment on the other hand develops a 'conveyor belt' made of fluid that has its own dynamic. The particles drag fluid with them which in turn push the particles to go faster. These exchanges of energy occur along the path of the settling particles, and it is possible that this is affected by scale effects. For example, if our experimental device was taller, a longer 'conveyor belt' would develop, and particles would have more time to interact with this flow as they fall. Testing this hypothesis would require to completely change the geometry of our device device, which is not feasible in the foreseeable future.

4.4 Comparison with numerical simulations

During this thesis, direct numerical simulations of point like particles settling in a fluid were performed by Anne Dejoan in continuation of a collaboration with Romain Monchaux. Figure 4.19 presents results from those simulations, where particles settle in a quiescent fluid. Like with the experimental data presented in this thesis, the goal is

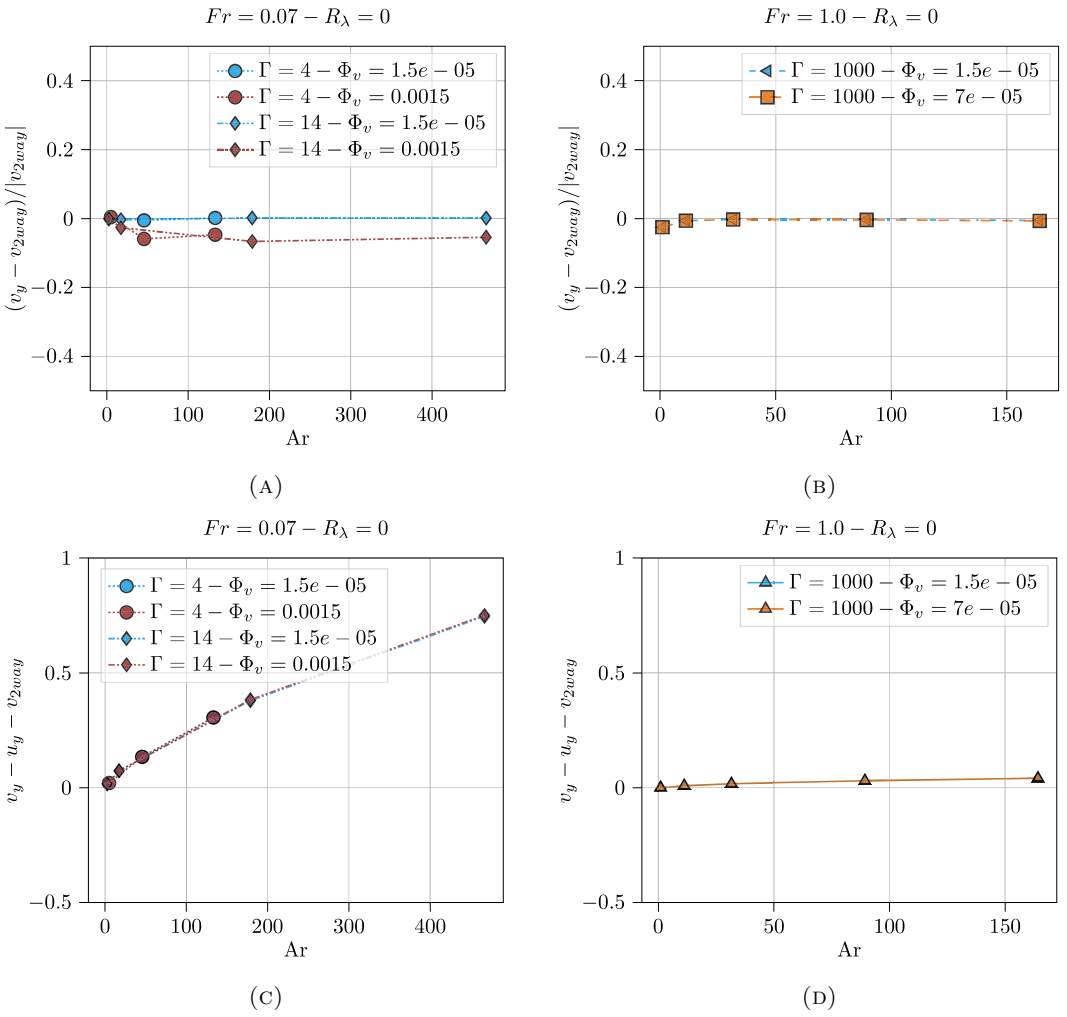

FIGURE 4.19: Results on vertical velocities from 2-way direct numerical simulations of particles settling in a fluid, for three Γ values ($\Gamma = 4$ and $\Gamma = 14$ on the left and $\Gamma = 1000$ on the right). (A) and (B) show the velocity alterations using the settling velocity obtained from a simulation where only one particle was present $v_{2\text{way}}$. (C) and (D) show the slip velocity between the particles and the fluid minus $v_{2\text{way}}$.

to test the influence of the control parameters Γ, Ar and loading (here Φ_V) on clustering and settling velocity alteration. These are 2-way numerical simulations using a non-linear drag model for the particles (Schiller-Naumann).

The settling velocity alterations for the computed cases are shown in figures 4.19a and 4.19b. In figure 4.19a, Γ has no effect and the data groups more by particle loading Φ_V, with the higher loading leading to an increased settling velocity. One notable exception to this observation is that low Ar values lead to reduced settling alteration compared to higher Ar values, which contradicts the observations made in the experiments presented in this thesis. This might come from the fact that the particles fall in a different system in the experiments and in the simulations, the former being an enclosed space with large

scale flows and the later a box with periodic boundary conditions. These difference certainly lead to different flows being developed by the falling particles and so to differences in the results between experiments and simulations. Further investigations are needed to explain this discrepancy. However, a comparison with figure 4.19b reveal that Γ does have an impact in numerical simulations, but it might only appear at significantly higher values ($\Gamma = 1000$ here).

Regarding the slip velocity in figures 4.19c and 4.19d, for a given particle population (i.e. fixed Ar and Γ), the particle loading Φ_V has no impact on the resulting slip velocity. The subtraction of the velocity measured in the experiments for a single particle settling ($v_{2\text{way}}$), also result in positive values, which means that particles fall at hindered velocities with respect to the surrounding fluid. These observations are in agreement with the ones made on figures 4.16 and 4.17. Interestingly Γ has an effect on the slip velocity in the numerical experiment when comparing the results for $\Gamma = 1000$ to the results from $\Gamma = 4$ and $\Gamma = 14$, but these last two show similar values. The experiments of this thesis on the other hand already hint at an influence of Γ being observed between $\Gamma = 4$ and $\Gamma = 15.63$. The numerical results also point at a clear influence of the Archimedes number, and results on more particle populations are needed to affirm whether this is also the case in our experiments.

More comparisons are still under way, especially concerning the fluid flow developed by the falling particles as well as their distribution to find whether clustering occurs or not.

Chapter 5

Perspectives and conclusion

An experimental device suitable for the study of settling dynamics of small inertial particles in a tank of quiescent water has been built. A procedure to prepare particle populations of select densities and size using sieving has also been implemented. This grants access to many parameter values in terms of density ratio Γ and Archimedes numbers Ar. Experiments have notably been performed on ceramics particles $\Gamma = 4$, and tungsten carbide particles to a lesser extent $\Gamma = 15.63$. Because a vast majority of the experiments used ceramics particles, the effects of Γ will be difficult to assess and experiments with more particle populations will be performed in the future. The particle mass loading Φ_m, output of the system, was also computed for each experiment. A straightforward double-measurement method was also developed, and gives simultaneous access to particle and fluid velocities by separating the tracers from the inertial particles on camera images.

Over our studied parameters, smaller values of Ar lead to increases of the settling velocity, with respect to the settling velocity of a single particle using a Schiller-Naumann drag model. When this increase occurs, higher Φ_m then amplify it. A Voronoï analysis also points toward clustering being observed as Φ_m increases, but regrouping of the data to obtain more converged statistics is necessary to validate this claim. In addition, the seeding of tracers should also be reviewed to ensure that the double measurement method does not impact the Voronoï analysis. When conditioning statistics to the local concentration of the particles however, no specific effect has been observed. From double-phase measurements, the fluid flow generated by the falling particles was also studied. Overall, higher Γ and higher Φ_m produce stronger downward flows, with higher spatio-temporal fluctuations in both the vertical and the horizontal directions.

These observations were interpreted as follows. The particles fall in a fluid that is in an enclosed space, dragging fluid down with them. This downward flow pushes the particles

in return and makes them fall faster. When the particles reach the main tank of the experimental device, shear mixing layers develop if the fluid dragged by the particles goes fast enough. This creates vortices that alter particle position and would create the clustering effect observed. Because all particles are affected equally by this effect, it is then expected that the local concentration around each particle has no impact on its settling velocity. The main cause for the particles' increase in settling velocity is then their interactions with the flow they create as they fall. Because particle with a lower inertia (which corresponds to a lower Ar number) are more susceptible to changes in the fluid flow, they are the ones that present larger increases in settling velocities.

If the particles are simply being pushed by an overall flow, their velocity would then be their expected settling velocity (for one particle) added on top of the fluid velocity. But looking at the slip velocity between the particles and the fluid revealed that this was not the case, and that particles in fact fall at hindered velocities with respect to the fluid flow surrounding them. Because the falling particles are the cause of the flow, energy exchanges happen between the particles and the fluid while the particles fall. In the main tank of the experiments, large scale flows certainly develop in what we can call a 'conveyor belt', as the water falls with the particles in the center of the tank and rises on the edges. The motor for this 'conveyor belt' are the falling particles, so they have to provide energy to the fluid to set it in motion, which could explain why they present reduced settling velocities with respect to the surrounding flow. The first falling particles set the fluid in motion, and the following one arrive in an established downward flow These energy exchanges between fluid and particles happen along the particles paths, and it is likely that if their paths were longer (i.e. higher experimental device) the same particle populations would not have the same slip velocities, as it would give them more time to exchange energy with the fluid.

It is important to note that this work chose to focus on established dynamics and ignore transient effects at the beginning and the end of experiments. This transient behaviours are a field of study that the present device can investigate. In particular, a large number of experiments present downward velocities of higher magnitude at the beginning of the experiments than at the established plateaus, both for the particles and the fluid. See figure 4.18a for an example of that. We think this is associated with the formation of an initial vortex ring that descend with the first falling particles. More work is required to confirm this hypothesis and to ascertain what are the conditions required for its formation.

Numerical simulation of cases close to our particle populations parameters where performed by Anne Dejoan. Enhanced settling velocities are also observed, with particle

loading increasing the settling velocity, but its dependency on Ar differs from the experimental results. Similar observations are made between slip velocity, loading and Γ, although Γ seem to impact experiments and numerical simulations differently. A dependency on Ar is also observed in the numerical simulations and more experiments are required to see whether this is the case in our experiments or not More comparisons are still under way.

A main goal of the project this thesis is inscribed in is how turbulence affect settling particles. The work from this thesis will then also be used as a reference point to compare with experiments that will be performed with turbulence in the experimental device, as a system of oscillating grids has been put in place and is currently in the process of being characterised. The different particle populations and the method to prepare them will give access to a large array of parameter values when turbulence will be added, namely St and Ro. This will allow to disentangle the effects of those various control parameters, including the Reynolds number of the turbulence in the fluid, on the effects studied here, namely clustering, settling velocity alteration and the links between those two phenomena. To that end, the double measurement technique developed in this thesis will also prove a valuable asset to study local particle-fluid interactions. In addition to numerical simulations of particles settling in a quiescent fluid, simulations with turbulence have also been performed, and will also be compared with future experimental results.

Overall, this thesis has laid important groundwork that will be built upon as the project that sparked it continues.

Bibliography

Adrian R, Westerweel J (2011) Particle Image Velocimetry. Cambridge University Press

Aliseda A, Cartellier A, Hainaux F, Lasheras JC (2002) Effect of preferential concentration on the settling velocity of heavy particles in homogeneous isotropic turbulence. Journal of Fluid Mechanics 468:77–105

Allen T (2003) Particle size analysis by sieving. In: Powder Sampling and Particle Size Determination, Elsevier, Amsterdam; London, chap 4, pp 208–250

Amoura Z, Besnaci C, Risso F, Roig V (2017) Velocity fluctuations generated by the flow through a random array of spheres: A model of bubble-induced agitation. Journal of Fluid Mechanics 823:592–616

Bagchi P, Balachandar S (2003) Effect of turbulence on the drag and lift of a particle. Physics of Fluids 15(11):3496–3513

Brown GL, Roshko A (1974) On density effects and large structure in turbulent mixing layers. Journal of Fluid Mechanics 64:775–816

Brown PP, Lawler DF (2003) Sphere Drag and Settling Velocity Revisited. Journal of Environmental Engineering 129(3):222–231

Chen R, Fan LS (1992) Particle image velocimetry for characterizing the flow structure in three-dimensional gas-liquid-solid fluidized beds. Chemical Engineering Science 47(13-14):3615–3622

Dejoan A, Monchaux R (2013) Preferential concentration and settling of heavy particles in homogeneous turbulence. Physics of Fluids

Eaton JK (2009) Two-way coupled turbulence simulations of gas-particle flows using point-particle tracking. International Journal of Multiphase Flow 35(9):792–800

Elghobashi S, Truesdell G (1993) On the two-way interaction between homogeneous turbulence and dispersed solid particles. I: Turbulence modification. Physics of Fluids A: Fluid Dynamics 5:1790

Elhimer M, Praud O, Marchal M, Cazin S, Bazile R (2017) Simultaneous PIV/PTV velocimetry technique in a turbulent particle-laden flow. Journal of Visualization 20(2):289–304

Falkovich G, Fouxon A, Stepanov MG (2002) Acceleration of rain initiation by cloud turbulence. Nature 419:151–154

Ferenc JS, Néda Z (2007) On the size distribution of Poisson Voronoi cells. Physica A: Statistical Mechanics and its Applications 385(2):518–526

Fornari W, Picano F, Brandt L (2016) Sedimentation of finite-size spheres in quiescent and turbulent environments. Journal of Fluid Mechanics 788:640–669

Gatignol R (1983) The Faxen formulae for a rigid particle in an unsteady non-uniform Stokes flow. Journal de Mécanique Théorique et Appliquée 2:143–160

Gustavsson K, Mehlig B (2011) Ergodic and non-ergodic clustering of inertial particles. Europhysics Letters 96(6):60012

Haralick RM, Sternberg SR, Zhuang X (1987) Image Analysis Using Mathematical Morphology. IEEE Transactions on Pattern Analysis and Machine Intelligence PAMI-9(4):532–550

Hascoët E, Vassilicos J (2007) Turbulent clustering of inertial particles in the presence of gravity. Advances in Turbulence XI pp 482–484

Hassan Y, Blanchat T, Seeley Jr C, Canaan R (1992) Simultaneous velocity measurements of both components of a two-phase flow using particle image velocimetry. International Journal of Multiphase Flow 18(3):371–395

Homann H, Bec J (2010) Finite-size effects in the dynamics of neutrally buoyant particles in turbulent flow. Journal of Fluid Mechanics 651:81–91, 0909.5628

Horowitz M, Williamson CH (2010) The effect of Reynolds number on the dynamics and wakes of freely rising and falling spheres. Journal of Fluid Mechanics 651:251–294

Huck P, Bateson C, Volk R, Cartellier A, Bourgoin M, Aliseda A (2018) The role of collective effects on settling velocity enhancement for inertial particles in turbulence. Journal of Fluid Mechanics 846:1059–1075

Huisman SG, Barois T, Bourgoin M, Chouippe A, Doychev T, Huck P, Morales CE, Uhlmann M, Volk R (2016) Columnar structure formation of a dilute suspension of settling spherical particles in a quiescent fluid. Physical Review Fluids 1(7):1–10, 1606.07329

Jenny M, Bouchet G, Dušek J (2003) Nonvertical ascension or fall of a free sphere in a Newtonian fluid. Physics of Fluids 15(1):L9–L12

Jenny M, Dušek J, Bouchet G (2004) Instabilities and transition of a sphere falling or ascending freely in a Newtonian fluid. Journal of Fluid Mechanics 508(508):201–239

Johnson TA, Patel VC (1999) Flow past a sphere up to a Reynolds number of 300. Journal of Fluid Mechanics 378:19–70

Kajishima T (2004) Influence of particle rotation on the interaction between particle clusters and particle-induced turbulence. International Journal of Heat and Fluid Flow 25(5):721–728

Kajishima T, Takiguchi S (2002) Interaction between particle clusters and particle-induced turbulence. International Journal of Heat and Fluid Flow 23(5):639–646

Khalitov D, Longmire E (2002) Simultaneous two-phase piv by two-parameter phase discrimination. Experiments in Fluids 32(2):252–268

Kidanemariam AG, Chan-Braun C, Doychev T, Uhlmann M (2013) Direct numerical simulation of horizontal open channel flow with finite-size, heavy particles at low solid volume fraction. New Journal of Physics 15

Kiger K, Pan C (2000) PIV technique for the simultaneous measurement of dilute two-phase flows. Journal of Fluids Engineering 122(4):811–818

Letournel R, Laurent F, Massot M, Vié A (2020) Modulation of homogeneous and isotropic turbulence by sub-Kolmogorov particles: Impact of particle field heterogeneity. International Journal of Multiphase Flows 125:103233

Lucci F, Ferrante A, Elghobashi S (2010) Modulation of isotropic turbulence by particles of Taylor length-scale size. Journal of Fluid Mechanics 650:5

Maxey M, Corrsin S (1980) Stokes spheres falling under gravity in cellular flow-fields. APS Bulletin 25:paper EA6

Maxey MR (1987) The motion of small spherical particles in a cellular flow field. Physics of Fluids

Maxey MR, Riley JJ (1983) Equation of motion for a small rigid sphere in a nonuniform flow. Physics of Fluids 26:883–889

Monchaux R, Dejoan A (2017a) Settling velocity and preferential concentration of heavy particles under two-way coupling effects in homogeneous turbulence. Physical Review Fluids 2(10):104302

Monchaux R, Dejoan A (2017b) Settling velocity and preferential concentration of heavy particles under two-way coupling effects in homogeneous turbulence. Physical Review Fluids 2(10)

Monchaux R, Bourgoin M, Cartellier A (2010) Preferential concentration of heavy particles: A Voronoï analysis. Physics of Fluids 22(10):1–10

Monchaux R, Bourgoin M, Cartellier A (2012) Analyzing preferential concentration and clustering of inertial particles in turbulence. International Journal of Multiphase Flow 40:1–18

Mora DO, Aliseda A, Cartellier A, Obligado M (2018) Pitfalls measuring 1d inertial particle clustering. In: iTi Conference on Turbulence, Springer, pp 221–226

Muste M, Fujita I, Kruger A (1998) Experimental comparison of two laser-based velocimeters for flows with alluvial sand. Experiments in Fluids 24(4):273–284

Nielsen P (1993) Turbulence effects on the settling of suspended particles. Journal of Sedimentary Petrology 63(5):835–838

Ouellette NT, OMalley P, Gollub JP (2008) Transport of finite-sized particles in chaotic flow. Physical Review Letters 101(17):174504

Parthasarathy RN, Faeth GM (1990a) Turbulence modulation in homogeneous dilute particle-laden flows. Journal of Fluid Mechanics 220:485–514

Parthasarathy RN, Faeth GM (1990b) Turbulent dispersion of particles in self-generated homogeneous turbulence. Journal of Fluid Mechanics 220:515–537

Petersen AJ, Baker L, Coletti F (2019) Experimental study of inertial particles clustering and settling in homogeneous turbulence. Journal of Fluid Mechanics 864:925–970

Poelma C, Westerweel J, Ooms G (2007) Particle fluid interactions in grid-generated turbulence. Journal of Fluid Mechanics 589:315–351

Pope SB (2000) Turbulent Flows. Cambridge University Press

Raffel M, Willert CE, Scarano F, Kähler CJ, Wereley ST, Kompenhans J (2018) Particle Image Velocimetry: A Practical Guide, 3rd edn. Springer

Riboux G, Legendre D, Risso F (2013) A model of bubble-induced turbulence based on large-scale wake interactions. Journal of Fluid Mechanics 719:362–387

Rosa B, Parishani H, Ayala O, Wang LP (2016) Settling velocity of small inertial particles in homogeneous isotropic turbulence from high-resolution DNS. International Journal of Multiphase Flow 83:217–231

Schiller L, Naumann A (1933) Über die grundlegenden Berechungen bei der Schwerkraftaufbereitung. Zeitschrift des Vereines deutscher Ingenieure 77:318–320

Schouveiler L, Brydon A, Leweke T, Thompson MC (2004) Interactions of the wakes of two spheres placed side by side. European Journal of Mechanics B/Fluids 23(1):137–145

Sumbekova S (2016) Clustering of inertial sub -Kolmogorov particles: Structure of clusters and their dynamics. PhD thesis, Université Grenoble Alpes

Tom J, Bragg AD (2019) Multiscale preferential sweeping of particles settling in turbulence. Journal of Fluid Mechanics 871:244–270, 1812.08830

Towers D, Towers C, Buckberry C, Reeves M (1999) A colour PIV system employing fluorescent particles for two-phase flow measurements. Measurement Science and Technology 10(9):824

Tsuji T, Narutomi R, Yokomine T, Ebara S, Shimizu A (2003) Unsteady three-dimensional simulation of interactions between flow and two particles. International Journal of Multiphase Flow 29(9):1431–1450

Uhlmann M, Doychev T (2014) Sedimentation of a dilute suspension of rigid spheres at intermediate Galileo numbers: The effect of clustering upon the particle motion. Journal of Fluid Mechanics 752(2):310–348, 1406.1667

Veldhuis CH, Biesheuvel A (2007) An experimental study of the regimes of motion of spheres falling or ascending freely in a Newtonian fluid. International Journal of Multiphase Flow 33(10):1074–1087

Vessaire J (2020) Couplages particules / turbulence dans un écoulement tourbillonnaire et fortement ensemencé. PhD thesis, Université de Lyon

Wang LP, Maxey MR (1993) Settling velocity and concentration distribution of heavy particles in homogeneous isotropic turbulence. J Fluid Mech 256:27–68

Wieneke B (2005) Stereo-PIV using self-calibration on particle images. Experiments in Fluids 39(2):267–280

Yang TS, Shy SS (2003) The settling velocity of heavy particles in an aqueous near-isotropic turbulence. Physics of Fluids 1205.3713v1

ECOLE DOCTORALE

Titre : Dynamique de sédimentation de particules

Mots clés : Particules inertielles - Vitesse de sédimentation - PIV et PTV simultannées

Résumé : La dynamique de particules inertielles lourdes évoluant dans un fluide présente un intérêt dans de nombreux domaines. On les trouve aussi bien dans la nature (gouttes d'eau dans les nuages, sédiments dans les rivières et les océans, disques d'accrétion planétaire) que dans des activités humaines et applications technologiques (gouttes de carburant en chambres de combustion, réacteurs chimiques). Ces systèmes sont complexes, leur modélisation requérant des hypothèses simplificatrices souvent fortes, et leur étude nécessite encore des données expérimentales.
De nombreux comportements sont observés dans ces écoulements diphasiques dispersés. Cette thèse s'intéresse à deux d'entre eux. D'abord le clustering, phénomène où les particules s'accumulent dans des régions spécifiques et en laissent d'autres vides. Le second est l'altération de la vitesse de sédimentation, des particules tombant plus vite ou plus lentement que dans un fluide au repos. Ces phénomènes sont liés, et dépendent de paramètres comme la taille et la densité des particules, de la phase porteuse (eau ou air généralement) et de si celle-ci est au repos ou dans un état turbulent.
Un dispositif expérimental a été construit dans lequel de petites particules solides (diamètre maximal de $200\mu m$) sédimentent dans de l'eau. Des particules de différentes densités ont été séparées par taille par tamisage. Ceci a permis d'accéder à une large gamme de paramètres pour les particules. Une technique de double mesure simple à mettre en œuvre permettant de mesurer simultanément la vitesse des particules et du fluide a été développée, fournissant un aperçu des interactions particules-fluides rarement réussi jusqu'à présent. Des augmentations de la vitesse de sédimentation des particules tombant dans un fluide au repos ont été observées et ont été attribuées au développement d'un écoulement descendant, poussant les particules. Des analyses de Voronoï ont également été effectuées, mais n'ont pas pu déterminer avec certitude si les particules formaient des amas ou non.
Ce travail fournit des données intéressantes, pertinentes pour l'étude des particules qui sédimentent dans des fluides au repos en espace clos. Il fournit également un point de référence pour de futurs travaux où la turbulence sera ajoutée au système.

Title : Particle settling dynamics

Keywords : Inertial particles - Settling velocity - simultaneous PIV and PTV

Abstract : The dynamics of heavy inertial particles evolving in a fluid are of interest in many fields. They are found both in nature (water droplets in clouds, sediments in rivers and in the oceans, planetary accretion disks) and in human activities and technological applications (fuel drops in combustion chambers, chemical reactors). These systems are complex, their modelling using often strong simplifying hypotheses, and experimental data is still required in their study.
A large range of behaviours can be found in such dispersed two-phase flows. This work focuses on two of these. The first is clustering, or the observation that particles accumulate in specific regions and leave others void. The second is settling velocity alteration, as particles have been observed to fall either faster or slower than in a quiescent fluid. These two phenomena are intertwined, and depend on parameters like the size and density of the particles, what the carrier phase is (water or air usually) and whether it is in a quiescent or turbulent state.
An experimental device was built in which small (diameters of at most $200\mu m$) solid particles settle in water. Particles of various densities have been separated by size by sieving. This allows access to a large variety of particle properties. An easy to implement double-measurement technique allowing simultaneous measurements of particle and fluid velocities was developed, providing insight into particle-fluid interactions that was seldomly achieved in previous works. Increases of the settling velocity of particles falling in a quiescent fluid have been observed and could be attributed to the development of a flow that pushes the particles down. Voronoï analysis were also performed, but could not confirm with certainty whether particles formed clusters or not.
This work gives interesting data, relevant in the study of particles settling in quiescent fluids in closed spaces. It also provides a reference point for future works where turbulence will be added to the system.

Institut Polytechnique de Paris
91120 Palaiseau, France